STUDY OF AIRFLOW AND PARTICLE TRANSPORT IN ACINAR AIRWAYS OF THE HUMAN LUNG

by

Haribalan Kumar

An Abstract

Of a thesis submitted in partial fulfillment
of the requirements for the Doctor of
Philosophy degree in Mechanical Engineering
in the Graduate College of
The University of Iowa

July 2011

Thesis Supervisor: Professor Ching-Long Lin

ABSTRACT

In this work, airflow and particle transport are studied using mathematical and image-based models of pulmonary acinus. Numerical results predict that airflow in the presence of wall motion in a three-dimensional honey-comb like geometry is characterized by the presence of a recirculation region within the alveolar cavity and a weak entraining flow between alveolar duct and cavity. Alveolar flow in distal generations is characterized by higher alveolar flow rates, larger entrainment of ductal flow and absence of recirculatory flow inside alveoli. The study of transport constitutes assessment of mixing visualized by the tracking of massless particles and the study of transport and deposition of aerosols. The phenomenon of steady streaming is found to hold the key to the origin of kinematic mixing in the alveolus, the alveolar mouth and the alveolated duct. This mechanism provides the explanation for observed folding of material lines and increases in material surface area, and has no bearing on whether the geometry is expanding or if flow separates within the cavity or not. Streaming results in non-zero drift of particles between the beginning and end of a breathing cycle. Based on flow conditions and resultant convective mixing measures, we conclude that significant convective mixing in the duct and within an alveolus could originate only in the first few generations of the acinar tree as a result of non-zero inertia, flow asymmetry and large K_C number. Evidence of streaming and related Lagrangian drift is also observed in image-based acinar models. Finally, particle deposition calculations are performed on the models of pulmonary acinus considered in this study.

Abstract Approved: _____
Thesis Supervisor

_____
Title and Department

_____
Date

STUDY OF AIRFLOW AND PARTICLE TRANSPORT IN ACINAR AIRWAYS OF THE HUMAN LUNG

by

Haribalan Kumar

A thesis submitted in partial fulfillment
of the requirements for the Doctor of
Philosophy degree in Mechanical Engineering
in the Graduate College of
The University of Iowa

July 2011

Thesis Supervisor: Professor Ching-Long Lin

ProQuest LLC.
789 East Eisenhower Parkway
P.O. Box 1346
Ann Arbor, MI 48106 - 1346

Graduate College
The University of Iowa
Iowa City, Iowa

CERTIFICATE OF APPROVAL

PH.D. THESIS

This is to certify that the Ph.D. thesis of

Haribalan Kumar

has been approved by the Examining Committee
for the thesis requirement for the Doctor of Philosophy
degree in Mechanical Engineering at the July 2011 graduation.

Thesis Committee: _____
Ching-Long Lin, Thesis Supervisor

_____
Merryn H. Tawhai

_____
Eric A. Hoffman

_____
Jia Lu

_____
Albert Ratner

To my grandma J, parents and my sister

ACKNOWLEDGMENTS

My deepest and sincere gratitude goes to my academic advisor and thesis supervisor, Professor Ching-Long Lin. This work would not have been possible but for his motivation during my low and high-times and most importantly for his patience and faith in me. The motivation he gave was very timely and most valuable. His constant support and inspiration helped shape my research attitude during the course of this doctoral study. I would like to thank all the members of my thesis committee for their support and motivation. They were also available for interactions, discussions and clarifications. I would like to also thank them for taking pains in reading this thesis content and providing valuable comment.

I would also like to thank my colleagues Jiwoong Choi, Youbing Yin, Dragos Vasilescu and Shinjiro Miyawaki for their help that came in various forms. Heartfelt thanks to my friend Shivkumar Sambasivan for his motivation, company and invaluable support both at and off work which made a huge difference to my stay and learning experiences at UI. I also thank John Mousel for his inputs and interactions-technical and non-technical. Thanks to others who might have unknowingly been missed out but made a difference in this learning process. I cannot end without thanking my family members to whom I dedicate this thesis.

This work was supported in part by NIH Grant numbers R01-HL-094315, R01-EB-005823, R01-HL-064368, and S10-RR-022421. I also thank Tera Grid via the Texas Advanced Computing Center for computer time.

ABSTRACT

In this work, airflow and particle transport are studied using mathematical and image-based models of pulmonary acinus. Numerical results predict that airflow in the presence of wall motion in a three-dimensional honey-comb like geometry is characterized by the presence of a recirculation region within the alveolar cavity and a weak entraining flow between alveolar duct and cavity. Alveolar flow in distal generations is characterized by higher alveolar flow rates, larger entrainment of ductal flow and absence of recirculatory flow inside alveoli. The study of transport constitutes assessment of mixing visualized by the tracking of massless particles and the study of transport and deposition of aerosols. The phenomenon of steady streaming is found to hold the key to the origin of kinematic mixing in the alveolus, the alveolar mouth and the alveolated duct. This mechanism provides the explanation for observed folding of material lines and increases in material surface area, and has no bearing on whether the geometry is expanding or if flow separates within the cavity or not. Streaming results in non-zero drift of particles between the beginning and end of a breathing cycle. Based on flow conditions and resultant convective mixing measures, we conclude that significant convective mixing in the duct and within an alveolus could originate only in the first few generations of the acinar tree as a result of non-zero inertia, flow asymmetry and large K_C number. Evidence of streaming and related Lagrangian drift is also observed in image-based acinar models. Finally, particle deposition calculations are performed on the models of pulmonary acinus considered in this study.

TABLE OF CONTENTS

LIST OF TABLES

Table

LIST OF FIGURES

Figure

CHAPTER 1

INTRODUCTION

1.1 Lung Anatomy

The human airway architecture is categorized into conducting and respiratory airways; dichotomously branching an average of twenty-three generations starting from the trachea. Alveoli are the air pockets that occupy a part of, or completely cover the walls of respiratory airways. An acinus consists of the entire region of alveoli and alveolated ducts that are distal to a single terminal bronchus, on an average beyond the fifteenth generation (Haefeli-Bleuer and Weibel, 1988; Finlay, 2001). The acinus is therefore comprised of respiratory airways and forms the functional tissue of the lung, or, the lung parenchyma. Figure 1.1 shows a schematic of the acinar airways from generations 16 to 23. Generations 16-18 are commonly denoted as respiratory bronchioles, generations 19-22 as alveolar ducts and the terminal closing lung units as alveolar sacs. Just like the upper airways, the respiratory or acinar airways also have a branching structure with roughly two bifurcations at each branch intersection. The surface area of the lung increases significantly down the acinar tree due to increasing alveolation. Figure 1.2 shows the variation of number of lung units and Reynolds number (Re) along the acinar airways. It can be seen that the number of lung units increases exponentially resulting in significant decrease in the Reynolds number at each generation. The typical Re ranges approximately from 2 in the respiratory bronchioles region to 0.01 in the terminal sacs.

1.2. Motivation and Objectives

Understanding transport of particles in the acinar region is useful in designing effective pharmaceutical aerosol or other drug delivery strategies, as well as treating disease with compromised lung function (Dailey and Ghadiali, 2007). Understanding of transport to and within the acinar region also has practical applications in targeting deposition to specific locations and henceforth reducing systemic absorption, and improving estimates for retention of inhaled pollutants. The deposition of particles is dependent on the flow by which they are transported, and the flow is dependent on alveolar geometries and ventilation conditions.

Mixing analysis provide a simple platform to study the mechanisms by which small particles could be irreversibly transferred across the inspired air-residual air interface. In an idealized setting, as a material dye is transported into the acinus, in the absence of non-linear effects, the shape of the dye will be completely recovered at the end of one breath. The only mechanism that would result in an inherent smearing of the dye interface is molecular diffusion. This behavior is indicative of diffusive mixing or spreading. An example is gas mixing where diffusive transport is the dominant mode. On the other hand, the dye may suffer a large increase in its interfacial area at the end of one breath, even in the presence of a low-Reynolds-number flow in the acinus. This distortion and dispersion of the dye is due to the non-linear effects resulting from geometry and inertia. This behavior is indicative of kinematic or advective mixing. To determine the cause, characterize and quantify the presence of any such kinematic mixing mechanisms is one of the objectives of this work.

The study of transport comprises of study of mixing and deposition. Earlier efforts have relied on either axi-symmetric geometry or complex branching structure in two-dimensions under static loading. To bridge the gap between image-based and simplified alveolar models, it is imperative to first understand the transport phenomena using idealized, but more realistic, controlled geometries. The early proponents of mixing mechanisms associated with irreversibility within alveoli include Tsuda et al. (1995, 2002); Butler and Tsuda (1997); Haber et al. (2000) and Henry et al. (2002). Tsuda et al. (1995) and Henry et al. (2002) observed irreversibility in particle motion associated with recirculation in a toroidal acinar model. Henry et al. (2002) simulated oscillatory flow in an acinar model with multiple alveoli placed adjacent to each other along a straight duct. Advection pattern revealed folded dispersion of the dye released in the alveolar duct. This kinematic irreversibility was related to the flow structure observed within the acinus resulting from expansion and contraction of the geometry. Recently, Henry et al. (2009) demonstrated that alveolation is sufficient to produce convective mixing in a rigid wall oscillatory flow model with Re pertaining to proximal generations of the acinus. This observation completely shifted the onus from mixing originating due to time-dependent wall motion and saddle point. It also shifts the focus toward geometrical features apart from revealing that even fundamental mixing mechanisms are not completely understood.

The main objective of this work is to solve for flow and transport in the pulmonary acinus using simple idealized to more complicated models. Figure 1.3 presents a generalized and exhaustive chart that lists various approaches that could be used. There are three columns: geometry, boundary motion and objective. Although, the use of image-based realistic geometry of the entire acinus in a fully-coupled tissue-air

interface framework may be the ultimate feat, the current state-of-the-art is far from achieving this goal. Hence, in any study of flow and particle transport, various assumptions need to be made regarding choice of geometry and other physiologically relevant conditions. The rightmost column of Figure 1.3 lists the various objectives based on which the studies in this thesis have been designed. The first step is always to compute the flow structure by solving the incompressible Navier-Stokes equations. Once the airflow is computed, the flow field is used to analyze transport of particles. Here, the term 'transport' is used in a broader sense to represent both massless particles and aerosol particles. Massless particles provide a way to study various mixing and its mechanisms in the acinus. When aerosol particles are considered, the flow field is utilized to accurately compute particle deposition efficiency for 0.5, 1, 2, 3 and 5 μm particles.

Geometry

In this work, two representations of the acinus have been considered. First are idealized models of acinus in 2D and 3D. Flow in a simple 2D open cavity configuration is studied. A honey-comb like representation has been used to represent respiratory bronchioles, alveolar duct and terminal alveolar sacs. In the second approach, images from mouse lung obtained using high-resolution micro-CT are reconstructed to provide a realistic rendering of the acinus. Flow and transport are computed in this geometry.

Boundary conditions

Alveoli may be assumed to expand and contract during normal respiration. In reality, the mode of alveolar expansion remains unknown. Hence various limiting

assumptions have to be made when specifying the mode of alveolar expansion *a priori*. Various models in literature have considered rigid wall geometry for both alveoli and alveolar duct. It has been shown by various researchers that major differences arise both in the flow structure and particle deposition characteristics when the motion of alveolar wall and alveolar duct are not properly included in the model. Hence, the models of acinus have to be supplemented with appropriate boundary conditions to mimic breathing. Various efforts in the last decade have started incorporating alveolar wall motion into their simulation. Important flow characteristics and fundamental mixing mechanism have been discovered in acinar models by various researchers. Inspite of these studies, the importance of accurately specifying alveolar duct and alveoli expansion and its effect on resulting advection and mixing characteristics is not clear.

The content of various chapters in this thesis are as follows. Chapter 2 presents the various acinar models considered in this study. Chapter 3 presents the numerical details for simulations of flow and particle transport. Chapter 4-7 presents the results. Each of these chapters presents results and presents separate discussion on the results and its physiological implications. Chapter 4 presents the results of airflow in the idealized models of the acinus. Both 2D and 3D results are reported. Chapter 5 presents the significant and important contributions of this work. It reports the results of mixing calculations in 2D and 3D idealized models. Another important aspect of particle transport study is the estimation of particle deposition. Chapter 6 reports results of deposition efficiency and deposition distribution for aerosols in 3D acinar models. Finally, Chapter 7 studies advection and deposition in complex idealized and image-based multi-generational models of acinus.

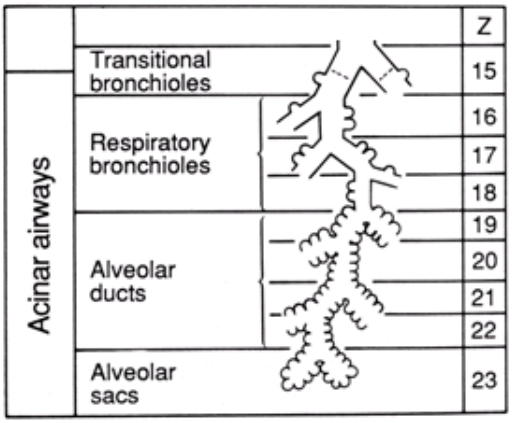

Figure 1.1 Schematic of respiratory airways. Z is the generation number. The generations are numbered such that Z=0 indicates trachea. Z=23 is the terminal alveolar sac.

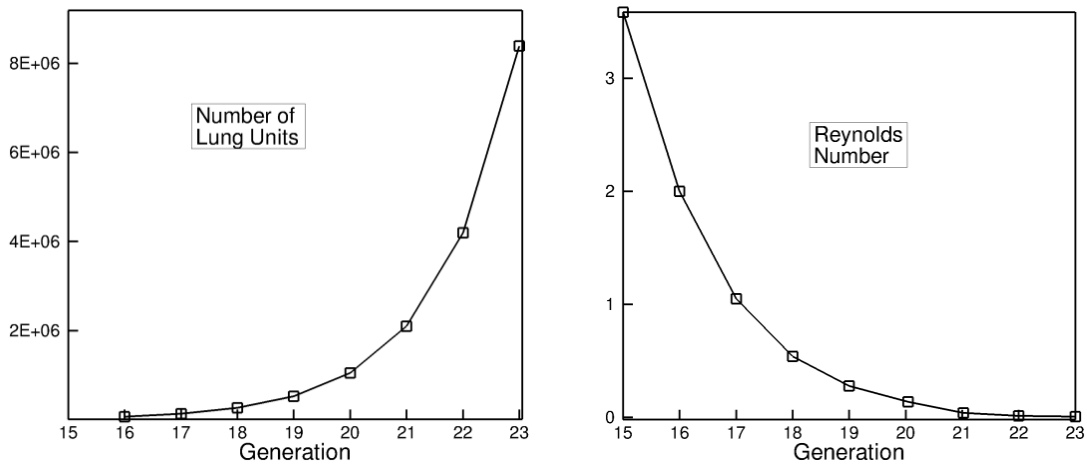

(a) (b)

Figure 1.2 Variation with acinar generation (a) number of lung units (b) Reynolds number

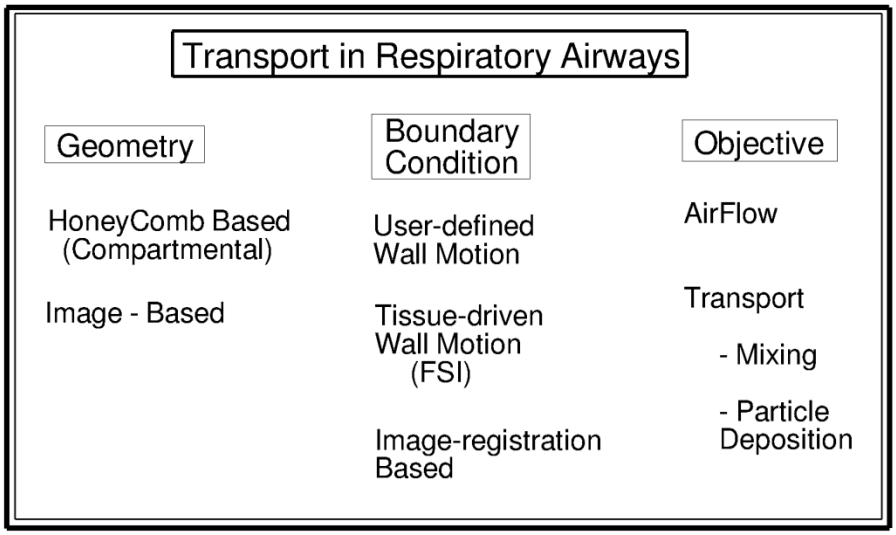

Figure 1.3 Objective-driven approaches to analysis of flow and transport in acinus.

CHAPTER 2

ACINAR MODELS

2.1 Introduction

In contrast to the progress achieved in upper airway reconstruction, the success in three-dimensional (3D) imaging of lung parenchyma has been limited by its size and accessibility (Tsuda et al., 2008). Recent studies have attempted to reconstruct the 3D image-based alveolar structure (Namati et al., 2007, Popp et al., 2007 and Tsuda et al., 2008), and define its dynamics (Carney et al., 2005). In their classical paper, Davidson & Fitz-Gerald (1972) studied flow patterns in spherical, cylindrical and ellipsoidal sections as representative of lung units. Tsuda et al. (1995) performed simulations on simplified expanding and contracting torus surrounding a central channel. Later, Henry et al. (2002) expanded this axi-symmetric model to 9-cell geometry. Unsteady 3D simulation efforts of fluid flow in the alveolated ducts and sacs in the past decade have been scarce. Darquenne and Paiva (1996) adopted a simplified model of the alveolated duct using sections of an annular ring around a central channel. Harrington et al. (2006) used a similar representation, but compared the effect of acinar branching using a bifurcation model. Haber et al. (2000) performed analytical investigation using a spherical cap to represent a single alveolus. Some of the later works also used self-similar breathing motion although using an isolated 3D cavity to represent an alveolus (Haber et al., 2003 and Sznitman et al., 2007). A recent effort towards simulation in the acinar tree was carried out by Sznitman et al., 2007 and Sznitman et al., 2009 who followed Fung (1988) to create an assemblage with 190 polyhedral units.

Given the limitations and challenges posed in view of geometric modeling and assumption of alveolar dynamics, earlier efforts have relied on either axi-symmetric geometry or complex branching structure in two-dimensions under static loading. Although technologies are emerging for acquiring alveolar geometries and constructing image-based alveolar models (Tsuda et al., 2008 for example), challenges arise in deforming these models and imposing boundary conditions for computation due to lack of knowledge and data on alveolar mechanics. To bridge the gap between image-based and simplified alveolar models, it is imperative to understand the transport phenomena using idealized, but more realistic, controlled geometries that account for the asymmetric feature of alveolar geometry.

This chapter describes the various models used in this work for which flow, mixing and deposition computations will be presented later. Section 2.2 describes the 2D open-cavity configuration. Section 2.3 presents the honeycomb acinar model.

2.2 Two-Dimensional Open Cavity Configuration

The alveoli can be best visualized as an isolated or group of open cavities ventilated by the acinar airway. The 'open cavity' configuration is an excellent prototype for understanding various fundamental features of flow and transport characteristics in acinar flows before embarking on to realistic representations of acinus. In this section, we introduce the model for a typical open-cavity configuration which would be later used to simulate the alveolar flow and mixing characteristics.

Consider an oscillating flow in a 2D long, straight channel with multiple grooves located periodically on the lower part of the channel as shown in Figure 2.1(a) and (b).

For reasons that will be described later, two configuration of the open cavity are considered. Figure 2.1(a) is a rectangular groove referred to as deep cavity. Figure 2.1(b) is a trough that will be referred as shallow cavity. Unlike the 3D cases to be discussed later, the channel and cavity walls remain rigid. Flow is simulated only in the mid-section of length ($L+2d_EL$). Due to low Re, the flow becomes fully developed within distances much less than one channel height. Hence a parabolic profile with a sinusoidal waveform is imposed at the ductal entrance "E", while a Neumann outflow condition is applied at 'N'. As shown in Figure 2.1, the upstream channel length is d_EL. By this specification, $d_E \rightarrow \infty$ is a model with a single cavity in an infinitely long channel, and $d_E=0$ is one where the channel is completely lined with grooves with no spacing in between.

2.3 Three-Dimensional Representation of Acinus

The longitudinal path length of the acinar region from an average 16th to 23rd generation may vary between 5,000-12,000 μm depending on the generation in which it terminates (Haefeli-Bleuer & Weibel, 1988). Although during respiratory ventilation the airflow has a single unobstructed path, a compartmental approach is considered and the problem is dealt using geometrical structures representative of regions along the acinar tree (Figure 2.2). The flow rate at the duct entrance is Q_D, the flow rate associated with cyclic expansion and contraction of the walls of a single alveolus is Q_A, and the flow rate associated with motion of the duct as Q_B. If the volume of an alveolar model is $\forall$, the total flow rate caused by alveolar wall motion is $\dot{\forall} = MQ_A + Q_B$. where M is the number of alveolar units in the model. The relationship between Q_D and $\dot{\forall}$ along the acinar tree is illustrated in Figure 2.2. Tsuda et. al. (1995) used Q_A/Q_D as a measure of the fractional

loss of inhaled volume. Due to alveolar expansion, this amount is displaced from the lumen and is unavailable to latter acinar generations (Sarangapani and Wexler, 2000).

The geometrical structures representative of regions along the acinar tree are identified as follows. Case I corresponds to respiratory bronchioles which have occasional alveolar units. The model for Case II is an alveolar duct lined completely with alveoli asymmetrically and represents the lung units in generation 18-22. Case III represent closed-end alveolar sacs. The current treatment uses a cluster of truncated octahedron to obtain a nearly space filling polyhedra (Tawhai & Burrowes, 2003 and Burrowes, 2005). The proximal wall of the alveolus is conventionally the one closest to the alveolus mouth during inspiration. Similarly the proximal generation is the generation of airways, which has already been ventilated along the path of the air. Analogously, a distal wall and a distal generation are defined. Finally, for closure, a complex honey-comb like model with single branching is also considered in this study. Figure 2.3 shows two views (frontal and side view) of this model. This model consists of 47 alveoli. As before, each alveolus is a truncated octahedron. For simplicity, the wall is considered to be rigid in this case.

Figure 2.4 shows a micrograph image cross-section of alveoli surrounding an alveolar duct with demarcated boundaries of septa. As shown by the 3D schematic in Figure 2.4(b), the structured arrangement of alveolar wall around the axial channel rationalizes the choice of the honeycomb-like polygonal model.

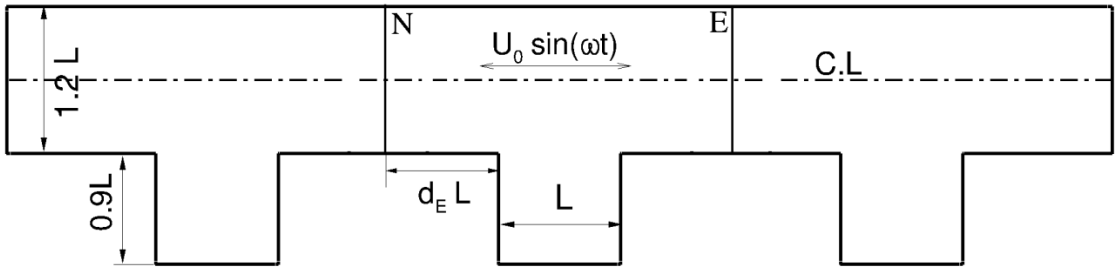

(a) Deep Cavity

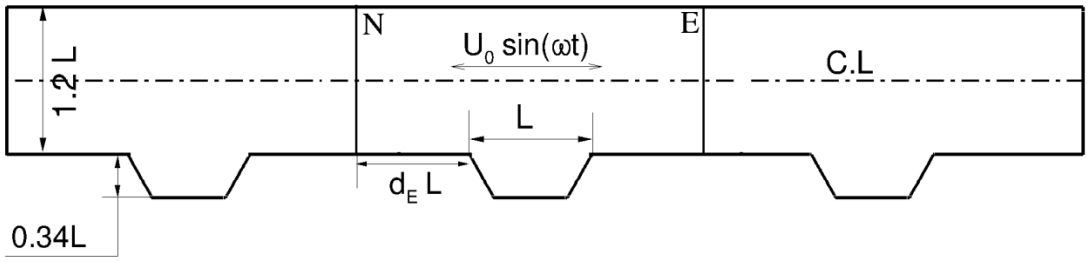

(b) Shallow Cavity

Figure 2.1 Schematic of a 2D channel with multiple cavities. d_E is the entrance length parameter. E, model entrance where a parabolic velocity profile is imposed; N, model exit where a Neumann outflow boundary condition is imposed. (a) Deep cavity (b) Shallow cavity.

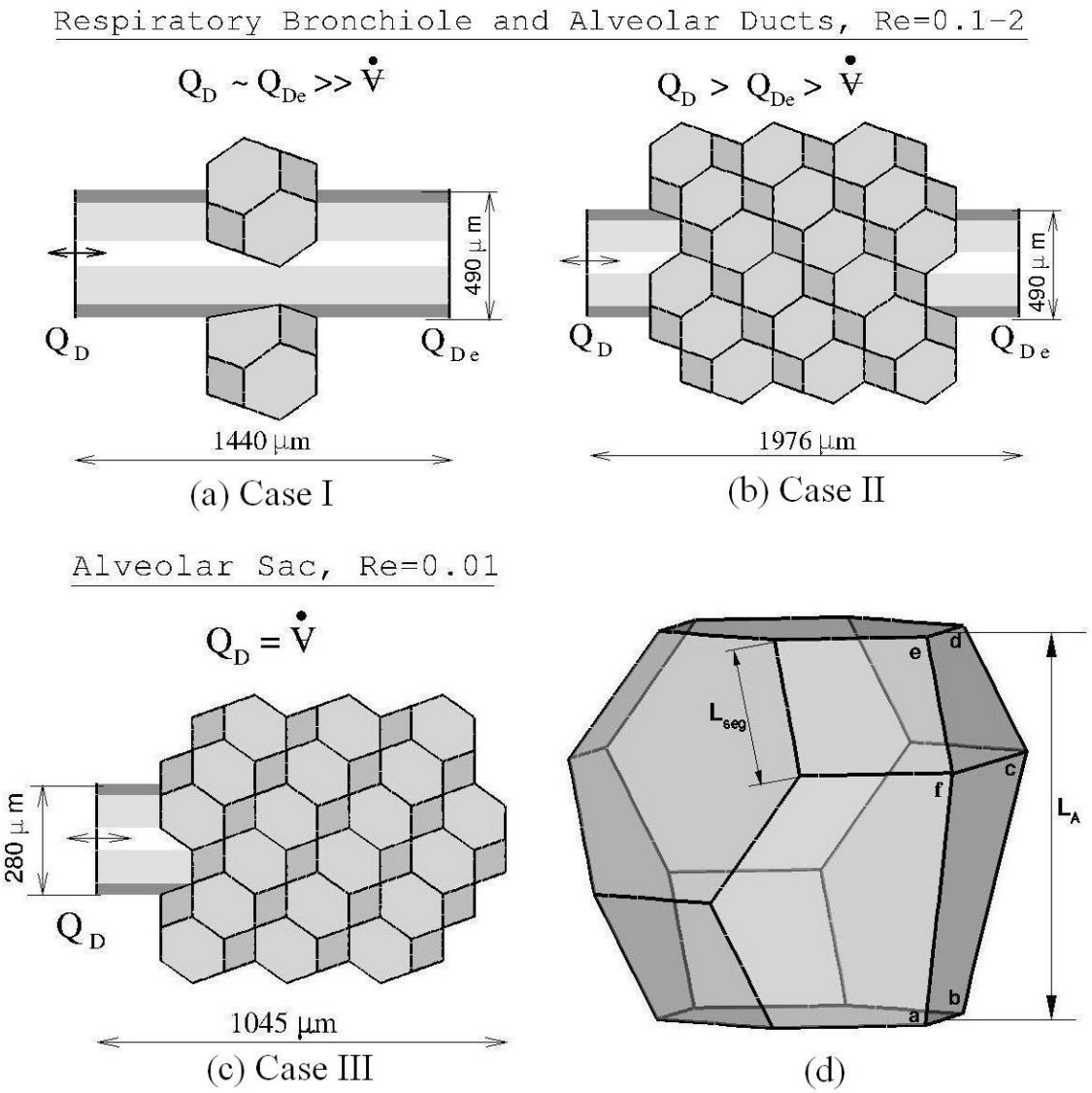

Figure 2.2 (a-c) Representative geometry for the acinar region. Q_D is the input flow rate at inlet and Q_{De} is the exit flow rate and (b) a typical alveolus represented as a truncated octahedron - consisting of 3 hexahedral faces and 5 square faces. 'abcdefa' is the non-coplanar alveolar mouth. For Cases I and II, segment length: L_{seg} = 171 μm and entrance length: L_A= 416 μm. Geometry for (a) Case I; (b) Case II; (c) Case III.

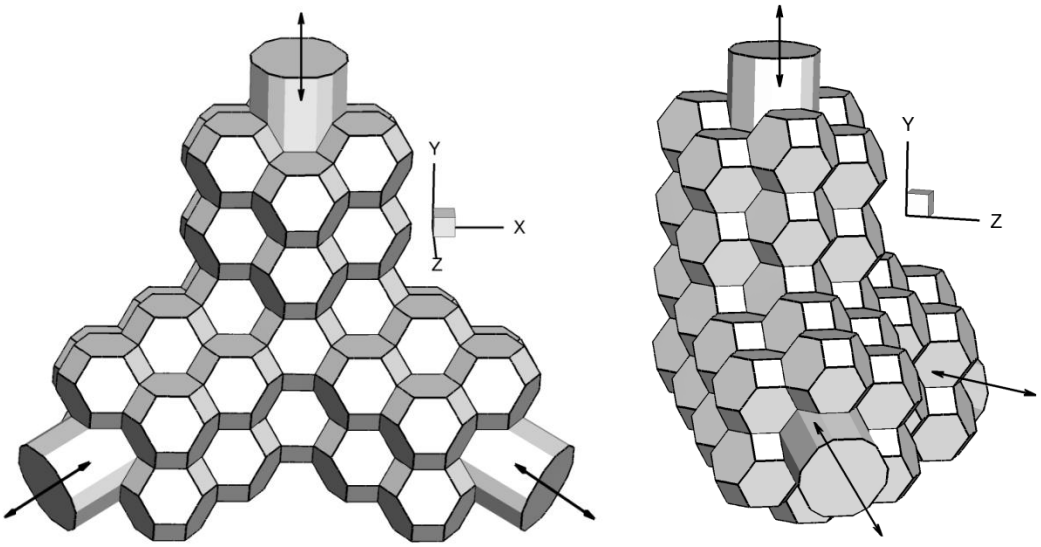

(a) (b)

Figure 2.3 Single bifurcation honeycomb model. (a) Front view. (b) Side view. The flow directions in the parent and two daughter ducts are marked.

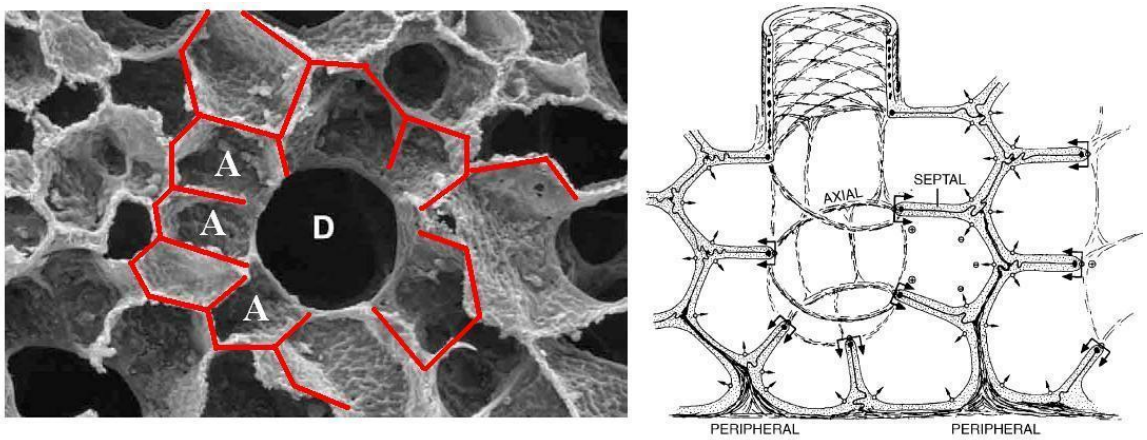

Figure 2.4 (a) Scanning electron micrograph of cross-section of an alveolar duct (D) showing densely packed alveoli 'A' surrounding the duct and (b) schematic of mechanical structure of basic acinar unit showing the septa and its arrangement around the axial channel of the airways (Reprinted with permission from Weibel et al., 2005).

CHAPTER 3

NUMERICAL METHODOLOGY

3.1 Flow Solver

The problem of alveolar flow is solved using the incompressible Navier-Stokes equations in a moving Arbitrary-Lagrangian Eulerian (ALE) grid setting (Sung et al., 2000, Quarteroni et al., 2000, Xia and Lin, 2008) as given below in index form.

$$\frac{\partial u_i}{\partial x_i} = 0$$

$$\frac{\partial u_i}{\partial t} + \left(u_j - \tilde{u}_j \right) \frac{\partial u_i}{\partial x_j} = -\frac{1}{\rho} \frac{\partial P}{\partial x_i} + \frac{\partial}{\partial x_j} \left(\nu \frac{\partial u_i}{\partial x_j} \right) \tag{3.1}$$

Here, u_i is the i-component fluid velocity, $\tilde{u}_i$ is the i-component mesh velocity, P the fluid pressure, ν the kinematic viscosity of air, and $(x_1, x_2, x_3)=(x, y, z)$. The system of equations is split using a fractional four-step method (Choi et al., 1997, Yue et al., 2003 & Lin et al., 2005) and then discretized spatially using an equal-order finite element method. The domain is discretized using tetrahedral elements with a smallest element having side of 5 μm. A single alveolar unit consists of ~40,000 elements. The Reynolds number is measured at peak inspiration: $\mathrm{Re}=UD/\upsilon$ where U is the peak inspiration speed, $D=\sqrt{4A/\pi}$ is the effective diameter of the duct, and A the duct cross-sectional area. One may also define a RMS-Reynolds number, $\mathrm{Re}_{\mathrm{RMS}}=\overline{U}\,\overline{D}/\upsilon$, where $\overline{U}\,(=U/\sqrt{2})$ and $\overline{D}$ $=(D_{\max}+D_{\min})/2$ are time averaged values of velocity and diameter, respectively. The Womersley number, $W_o=\overline{D}\sqrt{\omega/\nu}$ (where $f=\omega/2\pi=1/T$ is the frequency and T is the

breathing period) is 0.22 for Cases I and II, and is 0.12 for Case III, which match those of Sznitman et al. (2007). The breathing period chosen here, of 2.5 seconds (at 24 breaths/min) is similar to earlier alveolar studies (Tsuda et al., 1995 and Henry et al., 2002). The inverse of Strouhal number is known as Keulegan-Carpenter number (Pedrizzetti, 1996), $K_C = 1/St = UT/L$. It determines the displacement or length of fluid particle excursion over a characteristic length, L. For analysis, Case I (with Re=2, 1 and 0.52) and Case II (with Re=1, 0.6 and 0.2) are investigated. For Case I, Re=2, 1 and 0.52 yield K_C of 386, 193 and 96.5, respectively. An additional case of Case I with Re=0.06 is included to demonstrate that advection with Re approaching zero, predicted by the current analysis, exhibits essentially reversible behaviors. The flow phenomena along the acinar pathway are commonly associated with the fractional flow rate Q_A/Q_D introduced by Tsuda et al. (1995). Here, Q_A is the alveolar flow rate and Q_D is the ductal entrance flow rate. Note that in a rigid wall model, $Q_A/Q_D = 0$. This ratio, by definition increases down the acinar tree. For example, based on the ductal flow rate in Case I, $Q_A/Q_D=0.0024$ for Re=2 and $Q_A/Q_D=0.0047$ for Re=1. For isolated alveolar representations, we use Re to identify flow conditions in Cases I and II. For Case I with Re=1, due to non-zero Q_A the Re at the exit of the model is approximately reduced by 4%. The flow equations are normalized using the alveolus mouth dimension, L_A as in the isolated model alveolus of Figure 2.2 and peak velocity U. At Re=1, for example, U=3.21 cm/s corresponding to tracheal flow rate $Q_0=0.25$ liters/second and assuming that flow rate varies with generation number, n, as $Q(n)=Q_0/2^n$, based on an idealized dichotomous lung.

All models of acinus considered in this study essentially consist of a cavity attached to an external duct. The duct representing acinar airway lumen carries the ductal

flow and consists of an inlet and exit. Appropriate boundary conditions need to be provided to represent the rhythmic breathing condition. Unless specified otherwise, the following operating and boundary conditions have been used. A sinusoidal flow rate is specified at one end of the duct while a Neumann boundary condition is employed at the other. In cases when the wall remains rigid, all components of the fluid velocity on the wall are imposed as zero. In cases when the walls move during the breathing cycle, the following methodology is adopted. There is no consensus on the mode of volume change (Gatto et al., 2004) at alveolar level in response to lung expansion. Several modes of expansion like balloon-like isotropic expansion and paper-bag like crumbling have been proposed. In this study, homothetic wall motion where corresponding sides of the duct and alveolar wall remain parallel in a geometric expansion or contraction, a method analogous to isotropic expansion, is prescribed. The wall motion and flow are temporally coherent (Figure 3.1) producing a 25% volumetric expansion ratio (Henry et al., 2002). For case III, the expansion ratio is the determining parameter required to obtain a sinusoidal flow rate (corresponding to the Re desired). All computations were performed and tested for dependence on mesh and timestep.

One special case, introduced in Section 2.3 is that of a single branching of this honeycomb like model. For reasons that will be evident later, for our purposes, it is sufficient to consider a fixed wall case. Unless otherwise specified, all other 3D cases are moving wall geometries. The boundary condition for this single bifurcation geometry is specified as follows. Unlike the single branch case (Case I and Case II), an outflow condition is imposed with predetermined mass-flux ratio between inlets and outlets. It is assumed that the flow (and hence mass flow rate) exactly splits into half in each of the

daughter branches. A sinusoidal mass flow condition (parabolic) is prescribed at the inlet. At the outlets, velocities are corrected during the fractional step process so that a parabolic profile is still maintained ensuring non-zero velocity component present only normal to exit boundary. Such (mass outflow) boundary conditions are common in physiological flows, including arteries where the downstream ducts are not open to atmosphere and usually connected to other sections as a continuous flow device. Hence it is often useful to prescribe mass flux ratios between inlet and outlet ducts and derive boundary condition based on this assumption. Three Reynolds number cases have been considered, namely: Re=1, Re=0.5 and Re=0.25. This Reynolds number has been defined based on the hydraulic diameter of inlet (parent) duct and the peak inspiration velocity.

3.2 Validation

Cellular flows are a classical problem in the literature (Pozrikidis, 1994; Shen & Floryan, 1985; Pozrikidis, 2000; Horner et al., 2002 are some of them). The alveolar cavity poses a disturbance to the outer (steady or) oscillating shear flow. The problem of steady unbounded shear flow over a cavity (opening angle of $\pi/2$ with mouth twice the cavity depth) is studied by Pozrikidis (1994). The geometry demonstrates the characteristics of recirculating flows in the presence of a cavity. The 3D structure of the flow (Figure 3.2 (a)) and the location of the recirculation center in the cavity, in Figure 3.2(b) at ~45% of the cavity depth matches well with literature. The velocity field is extracted onto a chosen plane resulting in a two-dimensional streamline plot. Wall shear stress (Figure 3.2(c)) is plotted along the wall trace with the origin of arc length set at the entrance of the plane containing the cavity. The profile of shear stress, τ_w and the

prediction of flow reversal agree well. The wall shear stress, in Figure 3.2(c) at the corner (which is a singularity point) is under-predicted because of the limitation in resolution of the singularity of the flow, although the flow profiles far away remain unaffected.

3.3 Lagrangian Methods

The transport model of small aerosol particles across the interface of residual and inhaled air reduces to advection equation as sedimentational and depositional effects become negligible. Lagrangian tracking of massless particles is performed using the computed flow data stored at a finite number of time points in one breathing cycle. The advection is governed by the 3D kinematic vector equation:

$$\frac{d\boldsymbol{x}}{dt} = \boldsymbol{u}(\boldsymbol{x}, t), \boldsymbol{x}(0) = \boldsymbol{x}_0 \tag{3.2}$$

where $\boldsymbol{x}$ is the position vector of a passive particle (sometimes referred as a marker); $\boldsymbol{u}$ is the numerically generated velocity field and $\boldsymbol{x}_0$ is an initial condition. The advection is passive involving no diffusion of particles and the particle velocity exactly matches the fluid velocity. As the particles are transported through the fluid mesh, the fluid element in which the particle resides is determined as follows: A SALT or 'Search Algorithm for Linear Triangles (or Tetrahedrons in 3D)' algorithm is employed to search for the location of a particle in the fluid mesh at any given time-step (Allievi and Bermaro, 1997). In this procedure, the particle whose coordinate location is known is searched in an iterative manner. An initial seed element is provided. Usually the element in which the particle resided at the previous time-step provides the initial seed from which the search begins. It is convenient to store *a priori* the neighboring element information of the fluid mesh which can later be used during the particle search procedure. The advection is

carried out using a fourth-order Runge-Kutta scheme and a time-step independent solution is ensured with a choice of $\Delta t=T/500,000$. For details on a typical procedure to solve for particle transport, the reader is referred to Wang et al. (2003). All simulations are carried up to five cycles unless specified otherwise.

The mixing measures used in this study are designed to clarify the role of flow topology and geometry in the process of tracer transport. Three independent techniques have been used to study mixing: tracer advection, stretching analysis and axial dispersion. All three techniques are based on massless particle tracking. The formulation details are given below. Material advection (i.e. tracer deformation) is a classical technique used to study mixing in specific regions of interest. It involves passive tracking of tracers placed in strategic locations in a 3D flow. The tracer or dye is constructed from a uniform distribution of particles. The second technique, stretch rate analysis, is based on evolution of unit line elements computed from velocity and its gradient. This technique is an extension of the line element approach in Roberts and Mackley (1995) to 3D. Note that particle advection could also be used to compute stretch rate by considering relative separation distance of adjacent particles, which however is a lower-order approximation as it relies on only fluid velocity and fails in high stretch regions (Roberts and Mackley, 1995). The stretch rate computation based on the line element approach relies on higher-order approximation using fluid velocity and its gradient. In this approach, each particle location is tagged with line elements, following:

$$\frac{D\mathbf{m}}{Dt} = \mathbf{m}.\nabla\mathbf{u} - (\underline{D} : \mathbf{mm})\mathbf{m}$$
$$\frac{D\ln\lambda}{Dt} = \underline{D} : \mathbf{mm}$$
$$s_l(nT) = \frac{1}{nT}\int_0^{nT}\left(\frac{D\ln\lambda}{Dt}\right)dt \tag{3.3}$$

where $\mathbf{m} = (dx,dy,dz)^T$ is the orientation vector of any line element with $|\mathbf{mm}|=1$; $\mathbf{u}$ is the fluid velocity, $\underline{D}$ is the symmetric stretching tensor, and $D(\ln\lambda)/Dt$ is the stretching function. Time-averaged stretch rate, s_l, is obtained from the instantaneous stretching function (of dimension s^{-1}) averaged from three initially orthogonal line elements.

The third measure of mixing employed here is axial dispersion. In this approach, the variance of particle displacement is calculated based on axial location of particles (Sobey, 1985). The initial condition is a bolus of particles released at the entrance of the alveolar duct. For a bolus consisting of N markers, the axial mean $\langle y \rangle$ and variance σ_y^2 at the end of the n^{th} breathing cycle are defined as

$$\langle y \rangle = \sum_N [y_i(nT) - y_i(t_0)]/N$$
$$\sigma_y^2 = \sum_N [(y_i(nT) - y_i(t_0)) - \langle y \rangle]^2/(N-1) \tag{3.4}$$

where nT is the total time after 'n' breathing periods and t_0 may be the initial release time or some reference state, say the end of first breathing period. Because the current acinar model consists of alveoli attached to a straight duct, they represent a section of the acinar tree. A periodic boundary condition is employed so that particles exiting the domain are allowed to re-enter thus approximating multiple alveolar units attached to the duct.

3.4. Validation

3.4.1 Advection in 3D Cavity

To demonstrate the effectiveness of Lagrangian techniques to illustrate mixing, we consider flow induced in a 3D cavity ($0 \le x \le 3.34$, $0 \le y \le 2$, $0 \le z \le 1$) where the walls at $y=0$ and $y=2$ move tangentially (ABCD & LMNO in Figure 3.3 as shown by arrows) at $Re=0.01$. Adopting the mixing protocol $\mathscr{A}$ in Anderson et al. (1999), the wall motion is made discontinuous and time-periodic. Figure 3.3(b) shows the streamlines extracted in the $z=0.5$ plane in the two half-periods. Figure 3.3(d) and Figure 3.3(f) show the result of 3D deformation of an initially planar surface and patterns of stretching in the z-midplane, respectively. The results are in good agreement with Anderson et al. (1999) as shown in Figures 3.3(c) and 3.3(e). The tongue near the left wall in Figure 3.3(f) is a high stretch region surrounding a low stretch core.

3.4.2 Channel With Three Cavities

Henry et al. (2009) recently investigated mixing in a stationary wall axi-symmetric model to study the effect of unsteadiness induced by the oscillatory flow and non-zero inertia. The flow conditions pertained to proximal generations in the acinus. Their model has been chosen here for validation. The problem details and some of the results are given below. The geometry is a central channel surrounded by three cavities as shown in Figure 3.4(a). The solution is obtained for Re=2 ($Q_A/Q_D=0$) and a time period of 3s. The flow streamlines in the central cavity extracted onto the y-z plane are shown in Figure 3.4(b). Typical of open cavity flows, a single recirculatory flow region is observed in the cavity. A pair of fluid-particles initially separated by an infinitesimal distance of d_0

~10^{-11} are advected for 50 cycles. The rate of separation of this particle pair is estimated by finding the Liapunov exponent given as: $\sigma_n = \frac{1}{t}\ln\left(d_t / d_0\right)$. Here d_t is the final distance after time t. σ_n converges to a positive value of ~0.02 in good agreement with Henry et al. (2009).

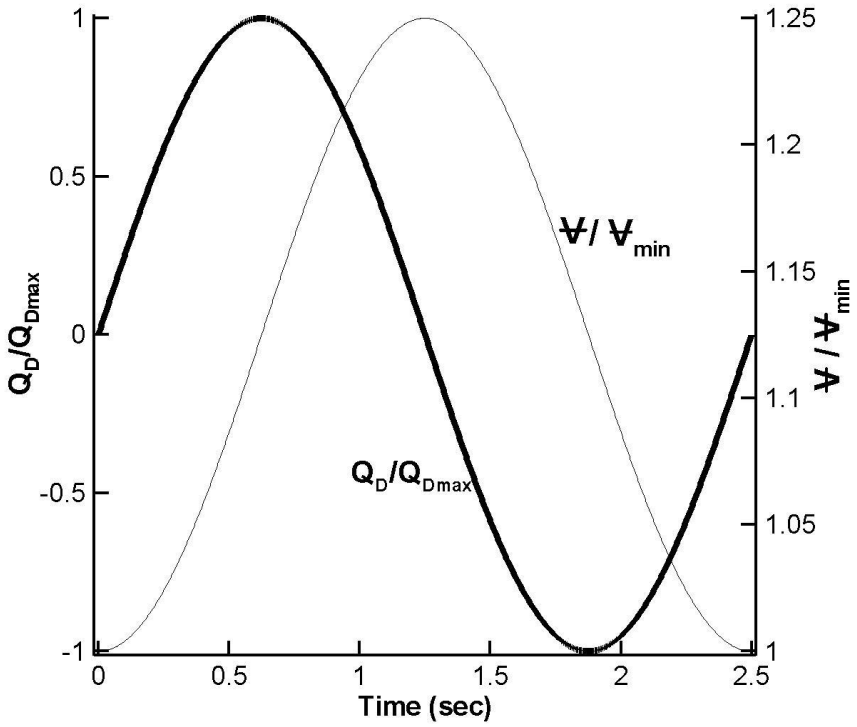

Figure 3.1 Temporal evolution of normalized inlet flow rate (Q_D/Q_{Dmax}) and normalized volume employed in our simulation.

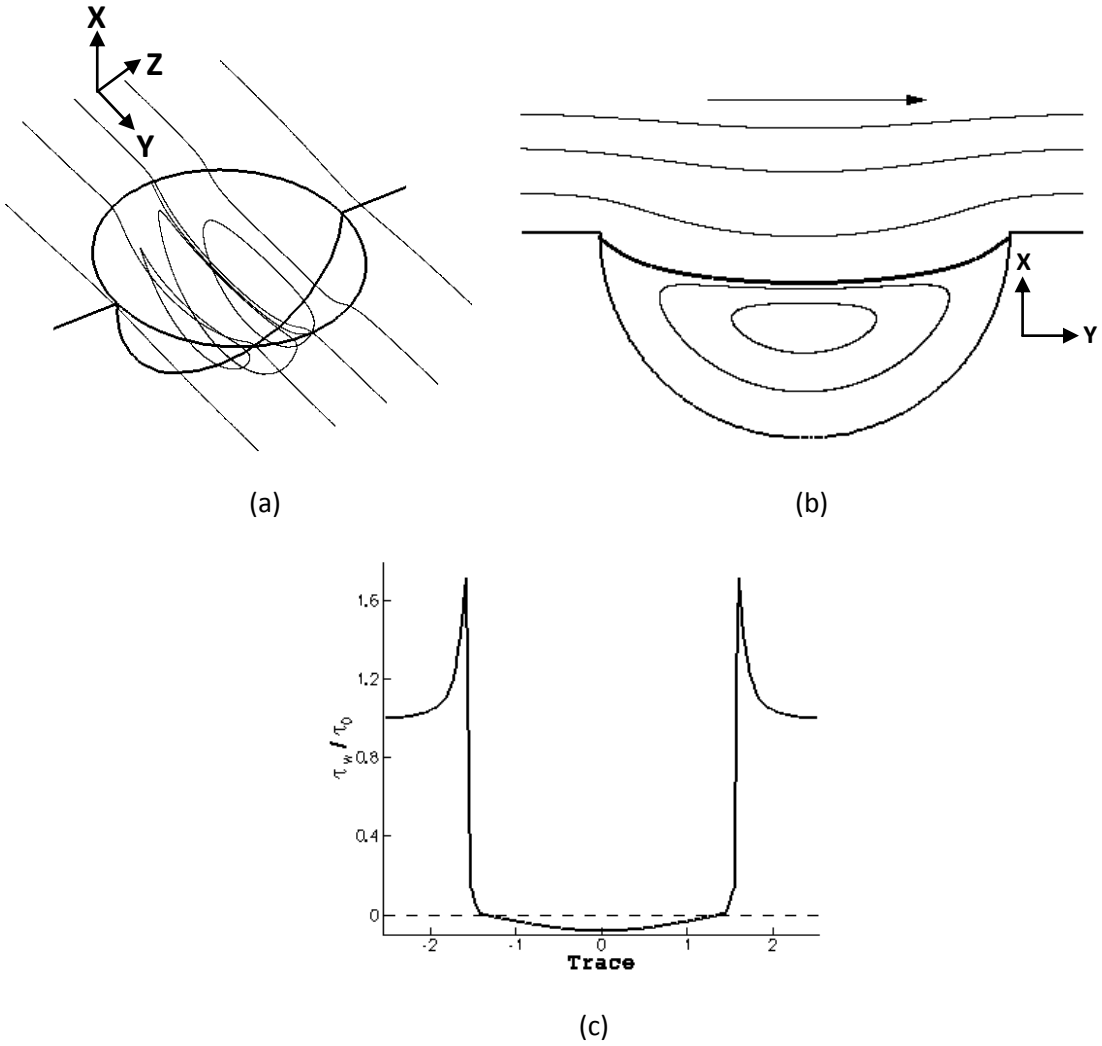

Figure 3.2 (a) 3D flow structure for Re=0.01; (b) extracted flow streamlines in *xy*-plane; (c) Shear stress along trace of the wall in the *xy*-plane. The zero shear stress line is shown dashed. τ_o is the unperturbed value corresponding to flow over the plane wall to which the cavity is attached.

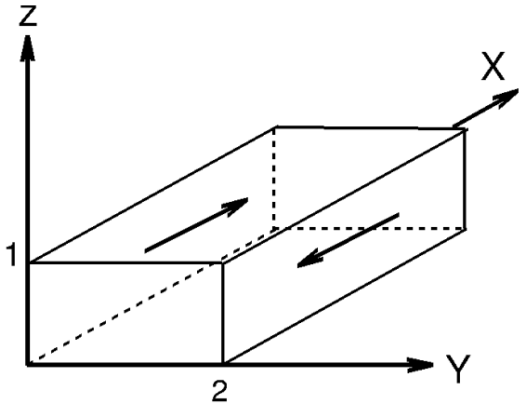

(a) Model of cavity

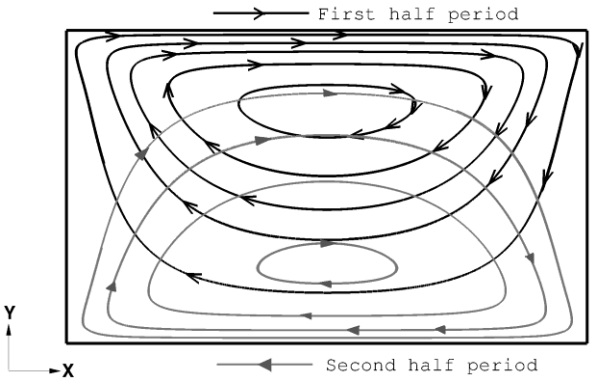

(b) Streamlines in z-midplane

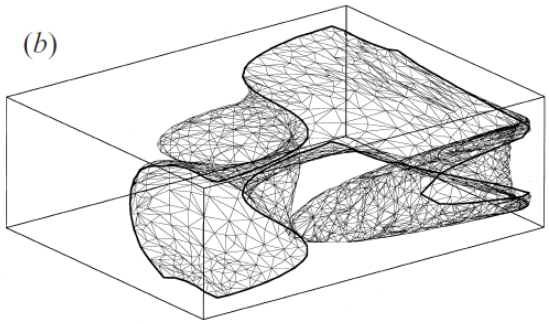

(c) Anderson et al. (1999)

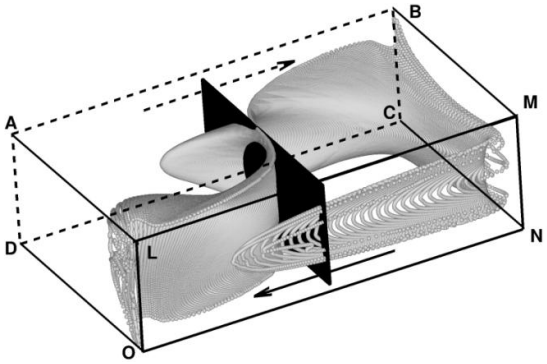

(d) Our result

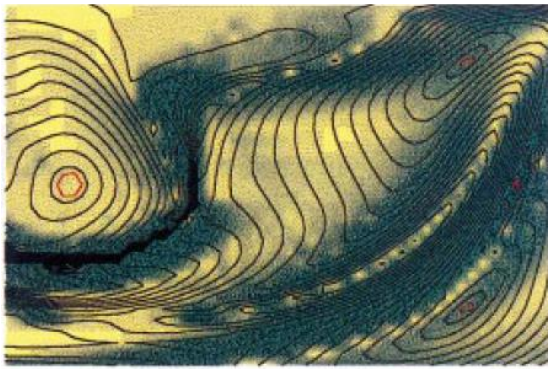

(e) Anderson et al. (1999)

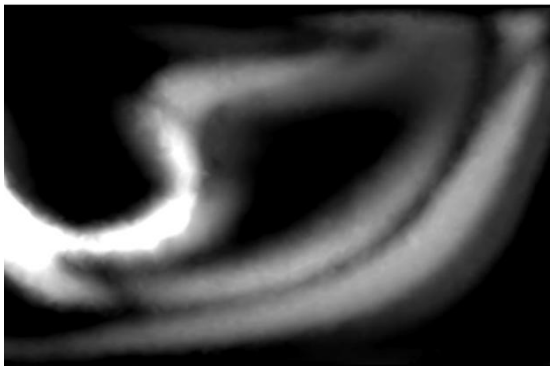

(f) Our result

Figure 3.3 (a) Model of 3D bounded cavity. (b) Streamlines in the xy-plane during two half periods when the wall is moving out of phase (c-d) Tracking of an initial material interface at t/T=1/8(black) and its deformed state at t/T=3/8 (gray). (e-f) Maps of period-one stretching in plane z=0.5. White regions correspond to high stretching and dark regions to low stretching.

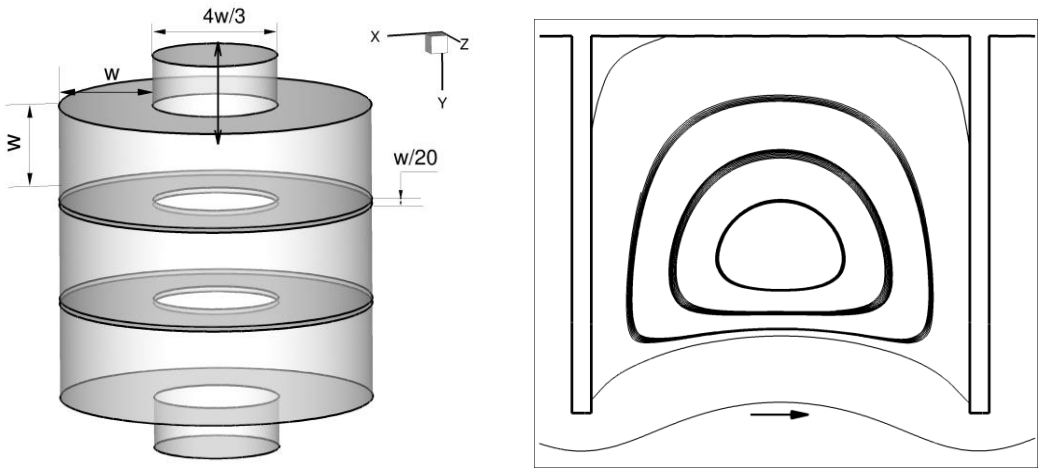

(a) (b)

Figure 3.4 (a) An axi-symmetric alveolated duct model used for validation. The model geometry and dimensions are chosen from Henry et al. (2009). (b) Streamlines in the cross-section of an axi-symmetric alveolus near peak inspiration.

CHAPTER 4

AIR FLOW

In this chapter, the results of alveolar flow field obtained by solving the incompressible Navier-Stokes equations are presented. The methodology for the solution process was described earlier in Chapter 3. This chapter is organized as follows. Section 4.1 presents the results for the two-dimensional open cavity configurations. Section 4.2 presents the results of the three-dimensional flow using the honeycomb representation of acinus. The results are presented for geometry representing respiratory bronchioles, alveolar ducts and alveolar sacs. The final section of this chapter presents analysis of flow topology by identifying stagnation points through an eigen-value analysis.

4.1 Two-Dimensional Open Cavity Flow

In this section, the results of flow field in a representative simple 2D open cavity configuration are presented. The geometry and model details are described in Section 2.2. The Re in a 2D setting is defined using the channel height (H) as $Re=U_0H/\nu$. All dimensions and flow conditions are chosen to match closely with Case I. Unlike the 3D cases to be discussed later, the channel and cavity walls remain rigid. Flow is simulated only in the mid-section of length ($L+2d_EL$). Due to low Re, the flow becomes fully developed within distances much less than one channel height. Hence a parabolic profile with a sinusoidal waveform is imposed at the ductal entrance "E", while a Neumann outflow condition is applied at 'N'. The Re in a 2D setting is defined using the channel height (H) as $Re=U_0H/\nu$. The simulation is carried out for Re=1 and $K_C=193$. This

combination of low-Re and high-K_C is unique for acinar flows. For the given flow conditions, the flow separates and forms one single recirculation eddy in the cavity. The flow structure is not symmetric with respect to the vertical centerline in the cavity as shown in Figure 3(b) and the deviation from symmetry is resulted from non-zero-Re inertia effects. The flow in the channel is separated from flow in the cavity by a separation line, which attaches itself to the sidewalls of the cavity. This separation line or 'separatrix' (Horner et al., 2002) penetrates roughly to 25% of the cavity depth. When the depth of the cavity is not sufficient, as in the shallow cavity case, streamlines penetrate deep into the cavity as shown in Figure 4.1(b). The dominant recirculation within the cavity is absent.

4.2 Three-Dimensional Acinar Flows

As discussed in Chapter 3, earlier efforts have relied on either axi-symmetric geometry or complex branching structure in two-dimensions under static loading. To bridge the gap between image-based and simplified alveolar models, it is imperative to understand the transport phenomena using idealized, but more realistic, controlled geometries that account for the asymmetric feature of alveolar geometry. This section examines fluid flow in the acinar region using realistic honeycomb-like polygonal geometries under imposed rhythmic breathing at varying Reynolds number. Specific effort is made to highlight the details and the role of the chosen geometry in view of fluid exchange to investigate duct-cavity interaction.

4.2.1 Case I

In geometry involving smooth or sudden expansions in a main channel, separation may occur due to net effect of pressure gradients in the outer flow and due to the sudden expansion. When the flow is steady, two flow regions appear: one within the cavity and the other as bulk flow, separated by a distinct 'separatrix' that attaches itself to parabolic points on the side wall (Horner et al., 2002).

Figure 4.3(a) presents the geometry considered (Case I) that represents the respiratory bronchiole. The mean diameter of the air carrying duct is ~500 μm (Haefeli-Bleuer & Weibel, 1988). The length of the duct is ~500 μm on either side of the alveolus. In the presence of prescribed wall motion and oscillating shear flow, the flow structure is different from that described above. The combined effects of oscillating ductal flow and rhythmic motion of the wall causes the fluid to recirculate (Figure 4.3(c)) near the proximal wall (the wall closest to the mouth during inspiration) of the cavity. Figure 4.3(b-d) shows the flow structure for Re=2, 1 and 0.52, respectively. The size of the recirculation is dependent on the Reynolds number. For Re=0.52 (Figure 4.3(c)), there is no re-circulating flow formed inside the alveolus. The inclusion of alveolar wall motion weakens the wall attachment point allowing convective interaction between the cavity and duct in the form of an entrainment region, E (i.e, the fraction of the ductal fluid entering the alveolus measured at the alveoli entrance. In a Lagrangian sense, a fluid particle placed within this region becomes a part of the alveolar flow), in Figure 4.3(c). The time rate of entrainment is proportional to Q_A. The width of the entrainment region changes during breathing; the extent of its unsteadiness is characterized by the Womersley number. As Wo<1, the unsteadiness is not pronounced except at times when

the flow rate is small, for example, at the start of inhalation (Finlay, 2001). The entrainment region is a function of Re: for example, it is confined to ~9-14 μm for Re=1, and ~19-26 μm for Re=0.52. During exhalation, the flow reverses in direction, but the motion of the alveolar wall is reversed, causing contraction of the geometry. Counter-intuitively, the fluid still recirculates in the proximal region within the cavity; although, the sense of flow about the recirculation is opposite to that during inspiration. During both inhalation and exhalation, associated with the recirculation is a stagnation point. Tsuda et al. (1995) and analyze the effect of wall motion on the recirculation and the nature and origin of this stagnation point. The flow rate reverses in sign at t/T=0.5 and a large recirculation fills the entire domain. The presence or absence of recirculation may be an important determinant of the nature of mixing of fluid particles. It is known that, even in 3D-Stokes flows, the presence of recirculation (Anderson et al., 1999 for example) can result in considerable stretching and folding of material interfaces, demonstrated through a Lagrangian analysis of the flow field using techniques like stretch rate field, dispersion, tracer deformation etc, (Ottino,1989) and will be discussed in the next chapter.

Figure 4.3(d) shows the contours of velocity magnitude in the y-z plane near the end of inspiration. The flow in the cavity is an order of magnitude smaller than the bulk flow (similar to observations by Sznitman et al., 2007). Within the cavity, the flow near the proximal wall is slower corresponding to flow recirculation.

4.2.2 Case II

Figure 4.4(a) is a model of an alveolar duct. Figure 4.4(b) shows streampaths (near the end of inspiration) in the yz-plane. Figure 4.4(c) plots selected streamline patterns projected onto the yz-plane for alveolar compartments, placed asymmetrically on opposite sides of the central air-carrying duct. The sizes of the entrainment region on the left and right asymmetric units vary ~13-18 μm and ~27-32 μm, respectively resulting in different sizes of recirculation regions, although the alveolar mouth area and Re are the same. The differences in ventilation pattern arising out of asymmetry in the model geometry are clearly evident here. Figure 4.4(c) illustrates this difference at Re=1 and 0.6. Note that the recirculatory flow is absent in one alveoli with an accompanying larger entrainment region. Hence, out of the 18 alveoli, separation occurs in only 9 of them. As mentioned earlier, the differences in entrainment and the presence (or absence of recirculation) translates to non-uniform transport and resulting mixing of particles within the alveoli. With subsequent inhalation cycles and the added role of gravity, the effect on estimations of dispersion and deposition may be different from computations based on simplified (e.g., axi-symmetric) models.

4.2.3 Case III

Alveolar sacs are the blind-ending terminal units of alveolar ducts. The duct has an effective diameter of ~300 μm (Haefeli-Bleuer & Weibel, 1988). In contrast to the alveolar ducts they are covered with alveoli even on their terminal surface (Figure 4.5 (a)). Figure 4.5(b) shows streamline patterns near peak inspiration. The flow within the alveoli does not recirculate during inhalation and exhalation. The flow is radial and a

significant portion of the flow (large Q_A/Q_D ratio) from the duct entrains the alveoli. The entrainment region from the outer airway lumen into the alveoli in the first stack is ~45 μm and ~53 μm on the left and right asymmetric units, respectively. Hence, asymmetry did not contribute significantly (unlike case II), to any variation in flow ventilation pattern across the entire acinus (in the last generation).

4.2.4 Reynolds Number and Recirculation

The size of recirculation becomes a function of the peak Re and decreases in size with Re. Figure 4.6 compares the Reynolds number in the current study and the observed recirculatory flow regime. Our model predicts that the recirculatory flow regime extends only upto third acinar generation. The Reynolds numbers used by Tsuda et al. (1995) and Henry et al. (2002) has also been plotted for comparison although these references did not mention the corresponding generation for which the results are applicable.

4.2.5 Flow in Single-Bifurcation Model

The flow streamlines for the single bifurcation model are plotted in Figure 4.7. The results are shown for Re=1 at t/T=0.25. Streamlines are plotted only in the alveolar duct. The alveoli surrounding the duct have been removed during visualization for clarity. The three plots show the flow structure in three alveoli located at the intersection of the three ducts, one proximally, one distally and one at the base as shown in Figure 4.7. Unlike Cases I, II and II above, the wall remained fixed and all alveoli contain a dominant recirculation that fills the entire cavity. Note that due to the octahedral shape of the alveoli, the branching structure from the parent to the daughter does not lie in the

same plane evident of a pure 3D branching structure (i.e) the two daughter branches do not lie in the same plane as the centerline of the parent branch.

4.3 Flow Topology and Classification

Figure 4.8 illustrates the flow topology and associated critical points within the alveolus by showing the instantaneous stream-traces in the y-z plane of the alveolus. The reasons for identifying critical points are two-fold. First, a stagnation saddle point had been attributed before for chaotic mixing in the alveoli (Tsuda et al., 1995; Henry et al., 2002; Tsuda et al., 2008). Second, the observed flow topology helps identify advection regions of interest for analysis in subsequent sections.

The flow topology can be classified by the first-order critical points of the flow in the y-z mid-plane. The type of critical points depends on the eigenvalues of the velocity gradient in the vicinity of a critical point (Ottino, 1989; Helman and Hesselink, 1991) The magnitude of fluid velocity vanishes at a critical point. The eigenvalues are computed from the characteristic equation $|[A]-\lambda[I]|=0$, where $[A]=A_{ij}=\partial u_i/\partial x_j$ is the Jacobian matrix based on the velocity gradient in the mid-plane and λs are eigenvalues, λ_1 and λ_2. The eigenvalues and the type of critical points for Case I, Re=2 and 1, are listed in Table 1 at time instants that roughly correspond to the maximum flow rate during inspiration and expiration. Two critical points are observed in Figure 4.8. By definition, if both eigenvalues are real with at least one of them being negative, the critical point is a ‘saddle’ point (see Figure 4.8(b)). If both eigenvalues are complex conjugates, the critical point is called a ‘center’ (see Figure 4.8(c)). The center point is found at the center of the recirculation, whereas the saddle point is near the proximal

wall. The presence of the saddle point is consistent with Tsuda et al. (1995) and Henry et al. (2002) who also recognized its presence within the cavity. Tsuda et al. (1995) explained that such a saddle point arises from superposition of a main recirculating cavity flow and the radial flow generated by wall motion.

As the critical point is in essence a stagnation point, the magnitude of velocity near the saddle point is relatively small. During expansion, the saddle point and recirculation are displaced deeper into the cavity. As shown in Figure 4.8(b), a saddle point diverts streamlines that pass into it to different regions, thus leading to uncertainty. The non-zero real part of the eigenvalue of the 'center'-like point depicts a spiral behavior. The change in sign between inspiration and expiration indicates the direction of this spiral. That is, the negative (positive) real part of the center-like spiral point implies that particles in its vicinity tend to move toward (away from) that point in a spiral fashion. Although the particles could move toward the spiral point from any direction, there is no guarantee that they would follow the same path in a reversible manner when moving away from it, resulting in uncertainty. Hence it was postulated that the presence of critical points might give rise to mixing in its neighborhood.

The entrainment region, a thin layer attached to the ductal wall, is also marked in Figure 4.8. The stream-trace, which represents the upper bound of this layer, is overlaid with solid circles. This stream-trace is open to the channel on the proximal-wall side, but is closed and attached to the distal wall, allowing advection of fluid into or out of the cavity. The presence of the entrainment region restricts the recirculation eddy to the right hand side of the cavity close to the proximal wall, and forms a saddle point where recirculating flow interacts with entrained flow and radial flow induced by wall motion.

In contrast, for the rigid-wall case, like the 2D channel flow shown in Figure 4.1, a separation line is formed at the mouth region to separate ductal flow from cavity flow and the recirculation is located approximately at the center of the cavity.

Table 4.1 Critical points in the flow.

Re	Time	Eigenvalues	Type	Location	
				w/L	h/L
Re=2	0.48π	0.203±5.63i	Spiral	0.366	0.477
		15.194, -0.98	Saddle	0.03	0.187
	1.52π	-0.2054±5.6i	Spiral	0.38	0.482
		0.987,-15.83	Saddle	0.032	0.192
Re=1	0.48π	0.03±3.33i	Center	0.2665	0.447
		2.542, -8.099	Saddle	0.046	0.207
	1.52π	-0.036±3.3i	Center	0.267	0.45
		8.351, -2.74	Saddle	0.045	0.21

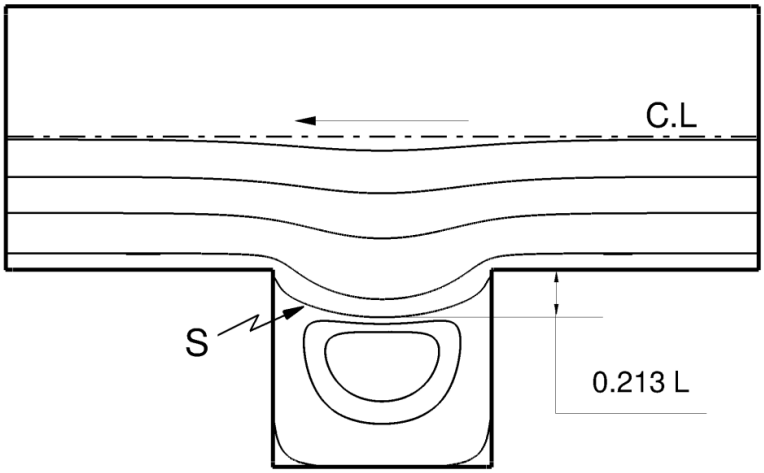

(a) Deep Cavity Case

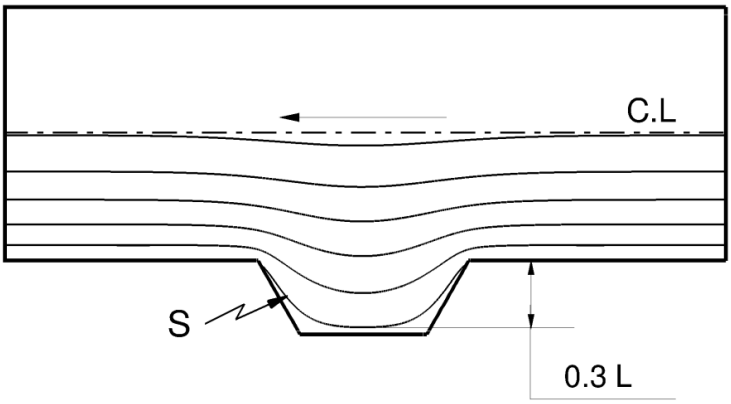

(b) Shallow Cavity Case.

Figure 4.1 Flow streamlines shown correspond to t/T=0.24, close to peak inspiration for Re=1. 'S' denotes the separatrix (a) Deep cavity case (b) Shallow cavity case

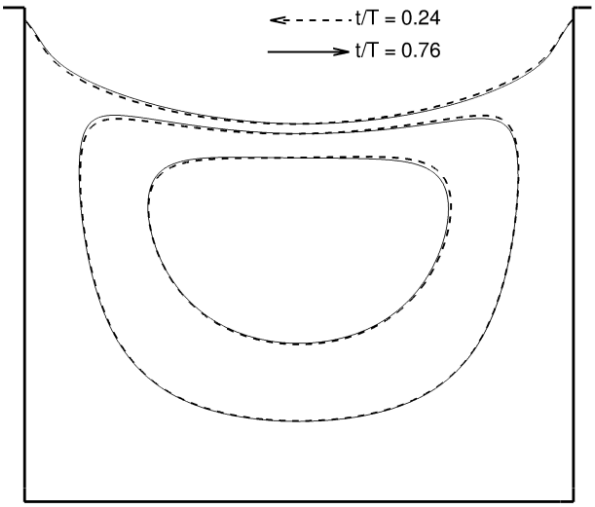

Figure 4.2 Deep cavity case: Streamlines at near peak inspiration (t/T=0.24) and expiration (t/T=0.76) in the cavity of a channel flow with Re=1. Arrows indicate the axial flow direction in the channel.

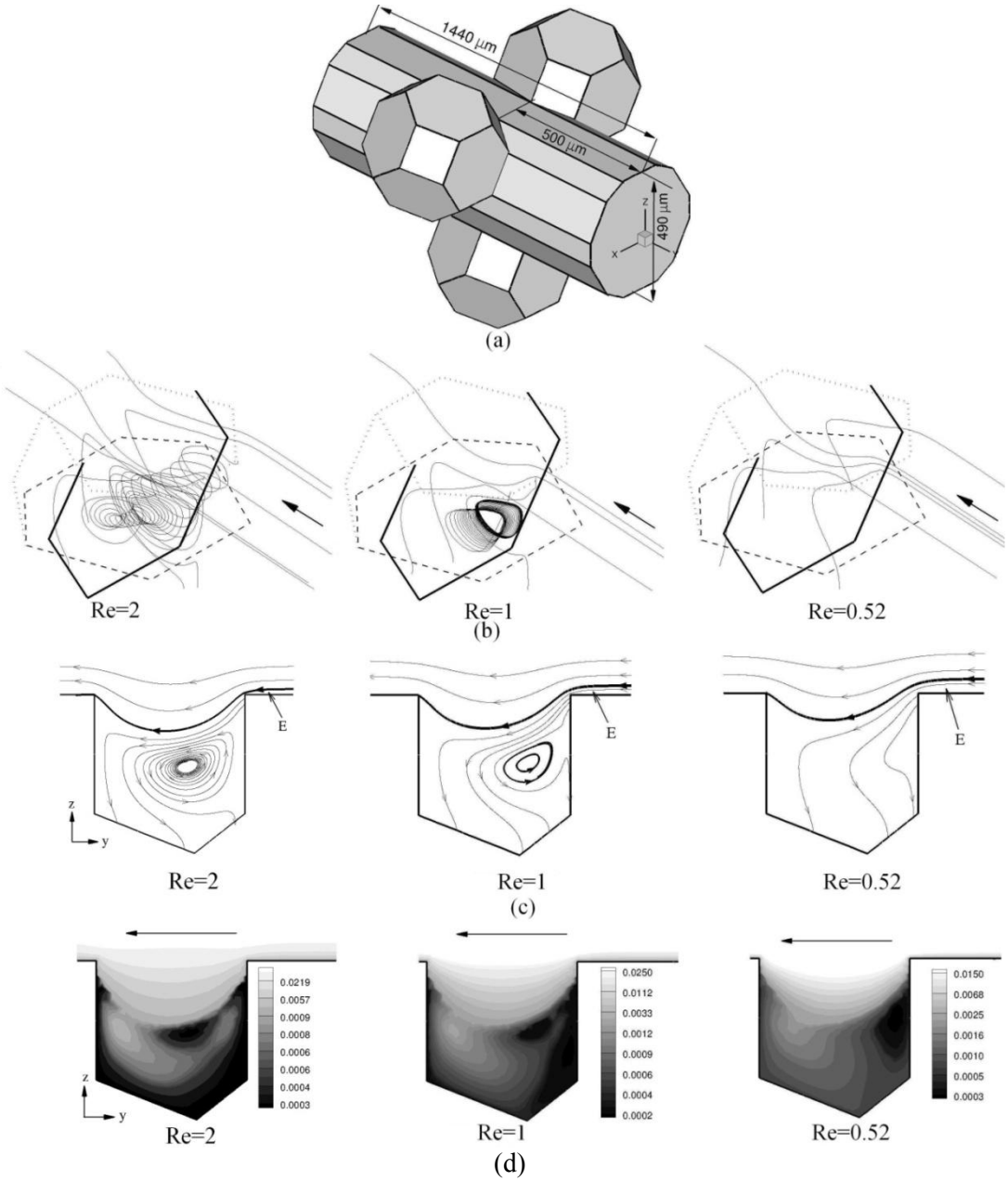

Figure 4.3 Case I (a) 3D model (b) 3D structure of the flow (c) Extracted set of instantaneous flow streamlines and (d) Normalized velocity magnitude in the yz-plane for Re=2, 1 and 0.52. E denotes the entrainment region.

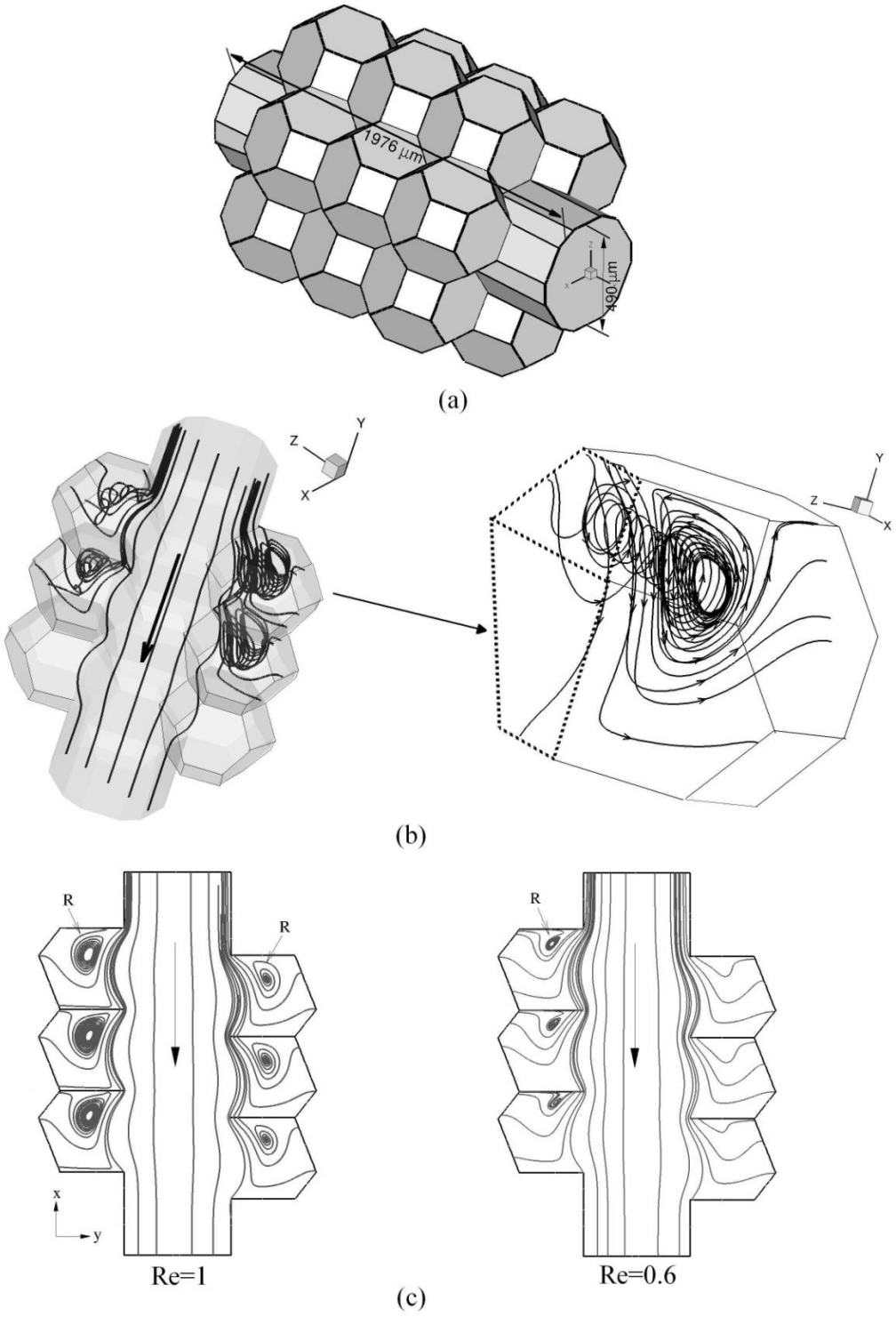

Figure 4.4 Case II (a) 3D geometry of honey-comb like alveolar duct (b) streamline pattern in the yz-plane at t/T=0.24 for Re=1.0 and Re=0.6. (c) Streamlines in the yz-plane near end of inspiration for Re=1.0 (left) and Re=0.6(right). R denotes the recirculation region.

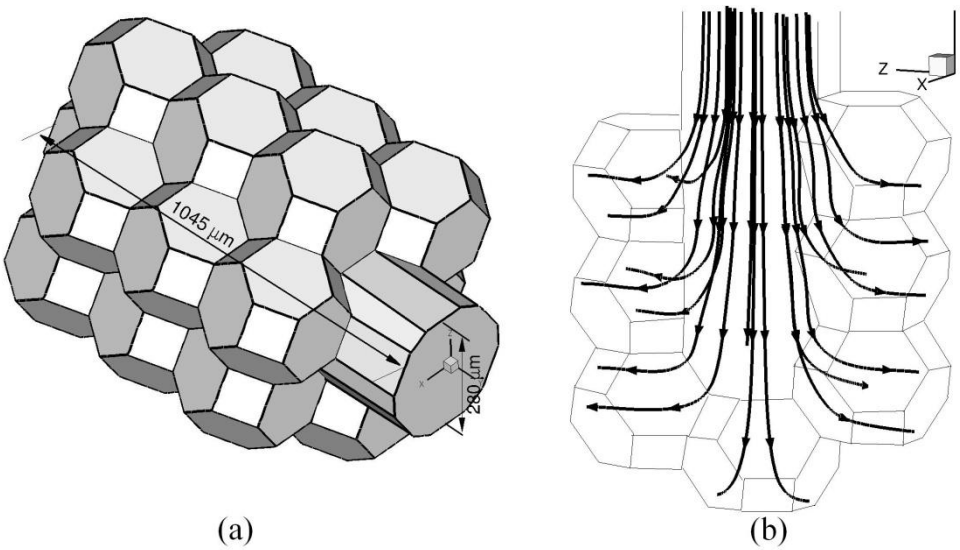

Figure 4.5 Case III (a) 3D alveolar sac geometry with a single entrance. (b) Streamline pattern in the yz-plane near end inspiration.

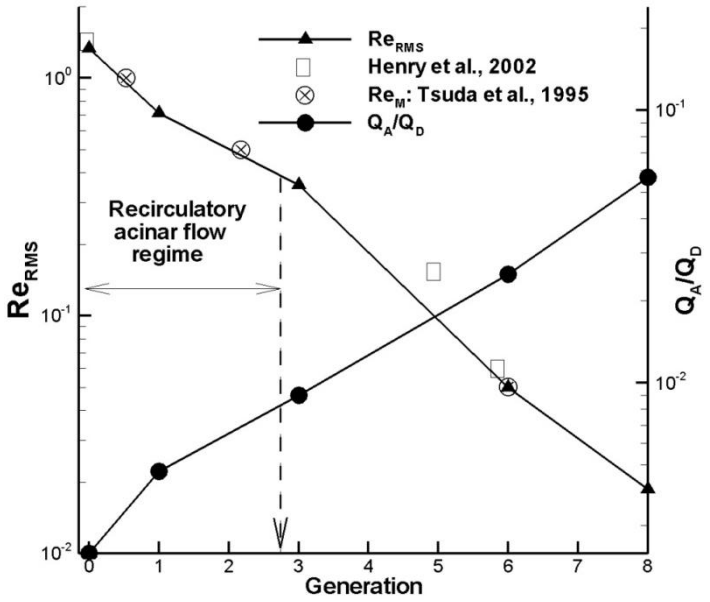

Figure 4.6 (a) Reynolds number and Q_A/Q_D variation with acinar generation number; Generation 15 is marked as 0 and hence generation 23 (corresponding to Case III in the results of the present study) as 8.

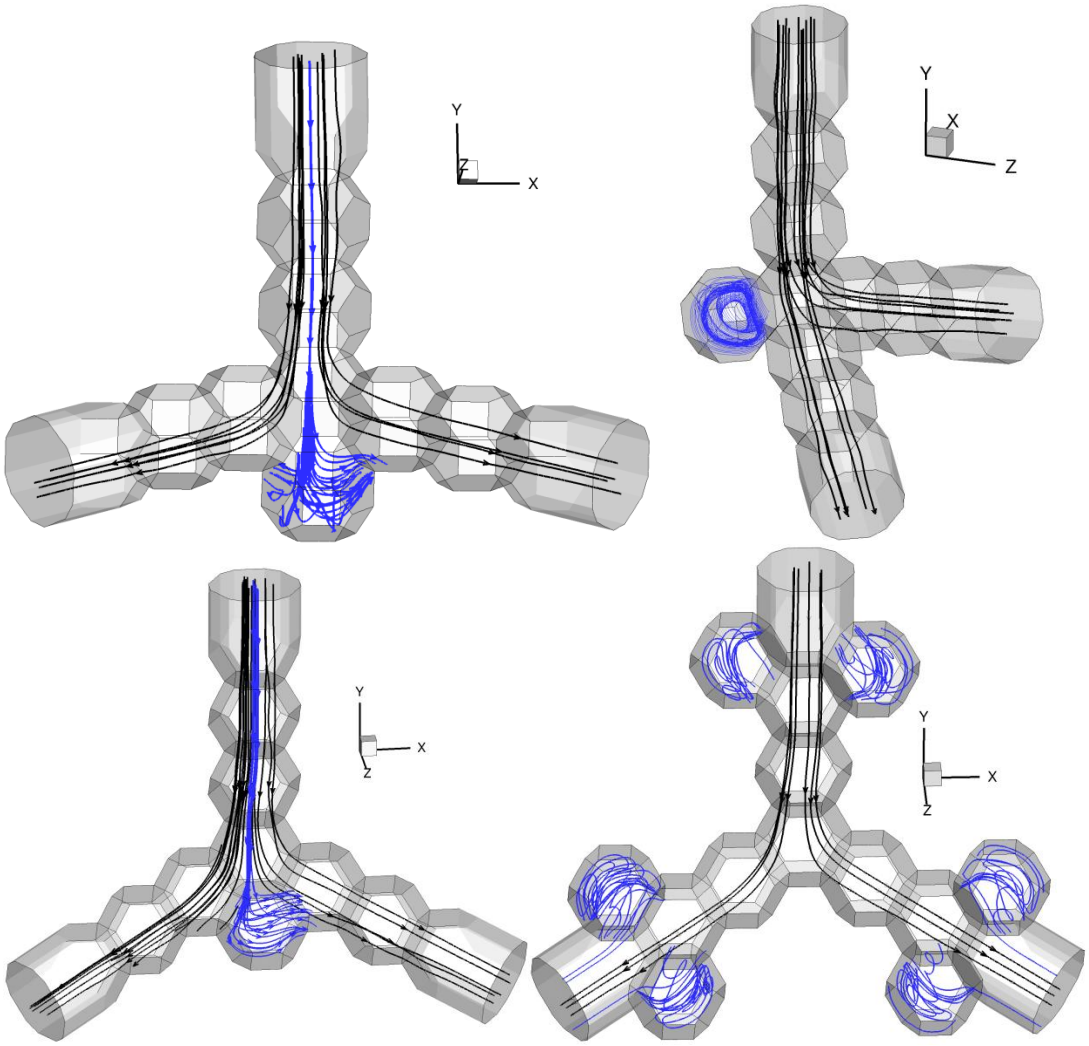

Figure 4.7 Streamlines in single-branching alveolar duct model shown at t/T=0.25 for Re=1 case. The flow in the central duct of parent, branch, daughter branch and certain selected alveoli are only shown to aid in visualization.

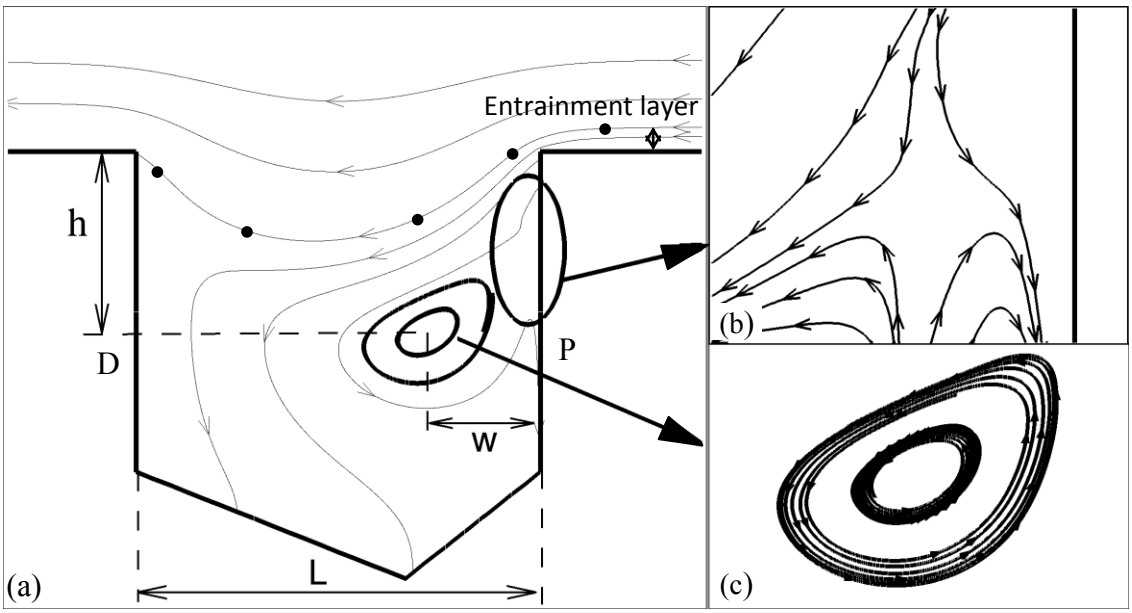

Figure 4.8 (a) Stream-traces in the y-z plane of the alveolus for Case I, Re=1 at t/T=0.24. The entrainment layer is denoted by a double-sided arrow, and its upper bound is delineated by the stream-trace marked with circles. P, proximal wall; D, distal wall. Enlarged view of: (b) a saddle point, (c) a center point (associated with recirculation). For a saddle point, $Im(\lambda_1)= Im(\lambda_2)=0$, $Real(\lambda_1)\times Real(\lambda_2) < 0$; for a center point, $Real(\lambda_1)=Real(\lambda_2)=0$.

CHAPTER 5

STREAMING AND MIXING

Mixing analysis helps study the mechanisms by which small particles could be irreversibly transferred across the inspired air-residual air interface. In an idealized setting, as a dye is transported into the acinus, in the absence of non-linear effects, the shape of the dye will be completely recovered at the end of one breath. On the other hand, even in the presence of a low-Reynolds number flow in the acinus, the dye may suffer a moderate to large increase in its interfacial area at the end of one or multiple breaths. This dispersion of the dye is due to the non-linear effects resulting from geometry and inertia. To determine, characterize and quantify the presence of any such kinematic mixing mechanisms is the main objective of this chapter.

5.1 Introduction

Several studies have attempted to identify mechanisms of mixing in low-Re flows. Some of the earlier works in this regard are Aref (1984); Chien et al. (1986); Swanson and Ottino, (1990); Jana and Ottino (1992); Jana et al. (1994); Anderson et al. (1999); Horner et al. (2002), and among others. The application areas include transport of material in processing industries, mixers, micro-fluidic applications and physiological flows. In addition to these applications, the study of mixing is important in understanding the transport of particles in the conducting and respiratory regions of the lung. Understanding of transport to and within the acinar region has practical applications in improving delivery strategies of pharmaceutical aerosols or other drugs, targeting

deposition to specific locations and henceforth reducing systemic absorption, and also for improving estimates for retention of inhaled pollutants. Without the assistance of turbulent mixing, how the low-Re acinar flow achieves effective mixing is the topic of interest in this chapter.

During normal breathing, when the inspired volume is larger than the anatomical deadspace, the inspired gas 'mixes' with the residual gas in the lung. In this process, particles are transferred to the residual gas across the inspired-residual interface front, which in case of aerosols is referred to as aerosol mixing. Peclet number ($Pe=U_0D/K$, where U_0 is the mean fluid velocity, D is the duct diameter and K is the diffusion coefficient) relates the magnitude of convective to diffusive transport. For gas mixing in the acinus, $Pe\approx0.1$-1, while for aerosol particles (say, ~1 μm diameter), Pe=3,000-20,000. Consequently, convection and diffusion manifest differently in these two mixing processes (Tsuda et al., 2008).

Particles with diameter 0.5-1 μm have very low deposition efficiencies in the acinus and behave like non-diffusing massless fluid particles (Heyder et al., 1988). Particles in this size range play a very important role in various physiological processes (Sznitman et al., 2009). Heyder et al. (1988) performed mixing estimates with aerosol bolus consisting of ~1 μm particles. The dispersion of the inhaled bolus increased with increasing penetration volume. The net transport of particles from the (particle-laden) inspired air to the residual air was shown to occur as a result of irreversible processes whose origins were unknown. This motivated investigations of possible transport mechanisms and their origin. The accomplishment of mixing, particularly in viscous

flows deep in the lung are non-trivial. Advective mixing was proposed as one such mechanism.

The early proponents of mixing mechanisms associated with irreversibility within alveoli include Tsuda et al. (1995, 2002); Butler and Tsuda (1997); Haber et al. (2000) and Henry et al. (2002). Tsuda et al. (1995) and Henry et al. (2002) observed irreversibility in particle motion associated with recirculation in an acinar model. Tsuda et al. (2002) performed experimental flow visualization in a rat lung using blue and white colored dyes for inspired and resident fluids. Lateral images of acinar airways revealed de-lineated interface patterns between the two dyes. After four breathing cycles, an indistinguishable blue-white uniformity appeared indicating a high degree of mixing. Recently, Henry et al. (2009) demonstrated that alveolation is sufficient to produce convective mixing in a rigid wall oscillatory flow model with Re pertaining to proximal generations of the acinus. This observation completely shifts the onus from mixing originating due to time-dependent wall motion and saddle point as thought earlier. It also shifts the focus toward geometrical features apart from revealing that even fundamental mixing mechanisms are not completely understood. Sarangapani and Wexler (1999) commented that the contribution from mixing towards a dramatic increase in the interface area requires numerous cycles and hence cannot completely explain the observed dispersion in a single cycle. Other works include those of Lee and Lee (2003) who used 30 identical toroidal alveolar cells and modeled inspiration and expiration in isolated phases. The differences in dispersion between alveolated and non-alveolated tubes in the presence and absence of wall motion were compared. Thus, from previous experimental and numerical studies, there seems to be no consensus on the explanation for origins of

convective mixing. Also, most demonstrations have been limited to use of single particle trajectories with inadequate quantifications. Darquenne and Prisk (2003) compared dispersion of aerosol bolus between simulation and experiments. For particles of critical sizes 0.5 and 1μm in diameter, order-of-magnitude discrepancy was observed in a zero-gravity environment. Flow-induced mixing was suggested as one possible cause. Later, Darquenne and Prisk (2005) designed a flow reversal mechanism to study the effect of acinar flow irreversibility. Experiments performed in microgravity failed to indicate any significant increase in dispersion and deposition with increase in number of flow reversals.

The investigation of irreversibility that arises in a system due to low but non-zero Re forms the starting point of the analysis in this chapter. The concept of irreversibility applied to acinar mixing gains special meaning in view of the targeted application area like drug delivery. Ultimately, the motivation for all these studies is to predict the mechanisms that cause particles to remain in the acinus after exhalation. Irreversibility, referred henceforth in a Lagrangian sense, signifies the drift or spreading of a passive particle from its initial position. This drift may arise due to flow topology, unsteady and geometry effects. Mixing as a result of such irreversibility is commonly referred as advective mixing. In the lung terminology, this mechanism is often referred as convective mixing at the interface between inhaled and residual air.

Results of flow structure in models of acinus were presented in the previous chapter. The objective of this chapter is to investigate the origin of advective mixing and quantify mixing in physiologically motivated models of the acinus using three Lagrangian techniques: tracer advection, stretching analysis and axial dispersion. Unlike

previous acinar mixing studies whose attention was restricted to a specific region, this chapter considers mixing in three regions: the duct, the alveolar mouth, and the alveolus. Apart from showing the presence of irreversibility in these regions, an important highlight of this work is to demonstrate that the origin of kinematic irreversibility in these regions, or any region of the flow, is physically associated with the same non-zero positive/negative steady streaming velocities formed at the alveolar entrance region due to inertia asymmetry in an oscillatory setting. Steady streaming results from cycle-averaged flow field and can lead to significant transport and drift of particles in an Eulerian time-averaged framework, and subsequent folding and mixing of material lines and surfaces. Of the three techniques, tracer advection and stretching analysis provide a measure of the mixing rate within the alveolus. The study of acinar mixing is not complete without understanding axial transport in the alveolated duct. Again, steady streaming is the driving mechanism underlying axial spreading of a tracer in the alveolated geometry. Axial dispersion is estimated in the alveolated airways.

5.2 Streaming and Tracer Advection

5.2.1 Stokes drift and Lagrangian Drift Velocities

The mechanism of Lagrangian drift outlined here derives its background from the well-known ‘steady streaming’ in oscillatory flows (Pedrizzetti,1996; Lyne, 1971; Duck and Bodonyi, 1988; Riley, 2001; Larrieu et al., 2009; Fresconi and Prasad, 2007; Flekkoy et al. 1996; Suh and Kang, 2008). In an oscillatory flow setting, a non-zero mean flow averaged over one time period may be observed. This non-zero mean flow can result in significant drift of particles at end cycle called steady streaming. An entire treatise on

steady streaming was given by Riley, 2001. Suh and Kang, 2008 presented different instances of streaming and the importance of Stokes drift. Larrieu et al., 2009 presented an analytical treatment of drift in a simple setting of Couette flow weakly perturbed by a wavy bottom. For any given passive particle under the assumption of small displacement, Eq. (1.1) with $\boldsymbol{x}(t=0)=\boldsymbol{x}_0$ may be expanded in a Taylor series.

$$\frac{d\boldsymbol{x}}{dt} = \boldsymbol{u}(\boldsymbol{x},t) \approx \boldsymbol{u}(\boldsymbol{x}_0,t) + (\delta\boldsymbol{x}\cdot\nabla)\boldsymbol{u}(\boldsymbol{x}_0,t) + H.O.T. \tag{5.1}$$

where the small displacement $\delta\boldsymbol{x} = \int_0^t \boldsymbol{u}(\boldsymbol{x}_0,t)dt$ and "*H.O.T.*" indicates higher-order terms of the series. Let the time average of a variable ϕ over one period of T be denoted as $\langle\phi\rangle$. Then, to the first-order approximation,

$$\frac{\boldsymbol{x}(T)-\boldsymbol{x}(0)}{T} = \boldsymbol{u}_L(\boldsymbol{x}_0) = \boldsymbol{u}_E(\boldsymbol{x}_0) + \boldsymbol{u}_S(\boldsymbol{x}_0) \tag{5.2}$$

where $\boldsymbol{u}_E(\boldsymbol{x}_0) = \langle\boldsymbol{u}(\boldsymbol{x}_0,t)\rangle$ and $\boldsymbol{u}_S(\boldsymbol{x}_0) = \langle\delta\boldsymbol{x}\cdot\nabla\boldsymbol{u}(\boldsymbol{x}_0,t)\rangle$. $\boldsymbol{u}_E$ is known as the "Eulerian mean" (or "Eulerian streaming") velocity and $\boldsymbol{u}_S$ is the "Stokes drift" velocity. $\boldsymbol{u}_L$, which is the sum of $\boldsymbol{u}_E$ and $\boldsymbol{u}_S$, is called the "Lagrangian mean" (or "Lagrangian streaming" or "Lagrangian drift") velocity. Lagrangian streaming is often referred to as steady streaming. Conceptually the decomposition of $\boldsymbol{u}(\boldsymbol{x},t) = \boldsymbol{u}(\boldsymbol{x}_0,t) + (\delta\boldsymbol{x}\cdot\nabla)\boldsymbol{u}(\boldsymbol{x}_0,t)$ or $\boldsymbol{u}_L=\boldsymbol{u}_E+\boldsymbol{u}_S$ resembles the material derivative $D\phi/Dt = \partial\phi/\partial t + \boldsymbol{u}\cdot\nabla\phi$ in a Lagrangian framework that consists of a local derivative (the former) and a convective derivative (the latter). More precisely, the acceleration of a fluid parcel is obtained by taking the time derivative of Eq. (3.2), which yields the material derivative of the parcel's velocity. Although steady streaming is a nonlinear phenomenon, the Eulerian streaming is caused by the fluid dynamical interaction (between fluid parcels and with the geometry of the

fluid system under consideration) and the Stokes drift arises from a kinematic viewpoint, depending on the pathline of the tracked particle. The decomposition Eq. (5.2) allows distinction between the two effects. Nonetheless, Eq. (5.1) holds true only when the displacement of a particle is small such that $\boldsymbol{u}(\boldsymbol{x},t)$ can be expanded in series with respect to the initial reference location $\boldsymbol{x}_o$. Typically, acinar flows are characterized by a large K_C number. Hence the above differential form of equation (5.2) must be modified in discrete form for large particle displacements. Consider a particle at a location $\boldsymbol{x}_j$ at $t_j = j\Delta t$ with $\Delta t = T/N$. To the first-order approximation of the Taylor series expansion of Eq. (1.1), the generalized stencil for the particle location is as follows.

$$\frac{\boldsymbol{x}_1 - \boldsymbol{x}_0}{\Delta t} = \boldsymbol{u}(\boldsymbol{x}_0, t_0) \qquad \text{for} \quad P = 1$$
$$\frac{\boldsymbol{x}_P - \boldsymbol{x}_{P-1}}{\Delta t} = \boldsymbol{u}(\boldsymbol{x}_0, t_{P-1}) + \boldsymbol{u}_I \qquad \text{for} \quad P = 2, N \tag{5.3}$$

where the "instantaneous" Stokes drift velocity at time t_{P-1} reads

$$\boldsymbol{u}_I = [(\boldsymbol{x}_1 - \boldsymbol{x}_0)\cdot\nabla]\boldsymbol{u}(\boldsymbol{x}_0, t_{P-1}) + [(\boldsymbol{x}_2 - \boldsymbol{x}_1)\cdot\nabla]\boldsymbol{u}(\boldsymbol{x}_1, t_{P-1}) + \ldots + [(\boldsymbol{x}_{P-1} - \boldsymbol{x}_{P-2})\cdot\nabla]\boldsymbol{u}(\boldsymbol{x}_{P-2}, t_{P-1})$$

Summation of the above discrete equations for P=1 to N gives

$$\frac{\boldsymbol{x}_N - \boldsymbol{x}_0}{T} = \frac{1}{N}\sum_{i=1}^{N}\boldsymbol{u}(\boldsymbol{x}_0, t_{i-1}) + \sum_{j=1}^{N}\{[(\boldsymbol{x}_j - \boldsymbol{x}_{j-1})\cdot\nabla][\frac{1}{N}\sum_{i=j+1}^{N}\boldsymbol{u}(\boldsymbol{x}_{j-1}, t_{i-1})]\} \tag{5.4}$$

where

$\boldsymbol{u}_L = (\boldsymbol{x}_N - \boldsymbol{x}_0)/T$ is the Lagrangian streaming velocity,

$\boldsymbol{u}_E = \frac{1}{N}\sum_{i=1}^{N}\boldsymbol{u}(\boldsymbol{x}_0, t_{i-1})$ is the Eulerian streaming velocity, and

$\boldsymbol{u}_S = \sum_{j=1}^{N}\{[(\boldsymbol{x}_j - \boldsymbol{x}_{j-1})\cdot\nabla][\frac{1}{N}\sum_{i=j+1}^{N}\boldsymbol{u}(\boldsymbol{x}_{j-1}, t_{i-1})]\}$ is the Stokes drift velocity.

And $\boldsymbol{u}_S = \sum \boldsymbol{u}_l / N$. For validation of formula (5.4), please refer to appendix A.

5.2.2 Streaming in a Hypothetical Setting

Figure 5.1 illustrates a simple setting in which a hypothetical flow profile (Haselton and Scherer, 1982) has been used to demonstrate steady streaming and the resultant transport of particles. Consider an oscillatory flow through a pipe. In the first of the cycle of time period T, the flow is from left to right in the Figure 5.1(a) above with a fully developed parabolic velocity profile. In the second half-cycle, the flow is from left to right with a plug-flow like velocity profile across the pipe cross-section. The cycle-average flow rate is zero. The axial component of steady streaming velocity along the tube cross-section, computed using Eq. (5.1) is shown in Figure 5.1(a). To understand the effect of this streaming on particle transport, we advect an initial tracer (red color region in Figure 5.1). The final shape of this region of material after one complete cycle is shown in blue. This simple example demonstrates the concept of steady streaming and the resulting tracer drift from its initial location. In summary, steady streaming is computed as the cycle-averaged flow field and results from differences in the velocity between inspiration and expiration in an oscillatory flow.

5.2.3 Streaming in a Progressive Wave Problem

Eq. (5.4) for the Eulerian mean and Stokes drift velocities is validated with a progressive-wave problem which has an analytical solution. Consider a 2D progressive wave having a velocity profile of $\boldsymbol{u}=U(y)\sin(\lambda x-\omega t)\boldsymbol{i}+V(y)\cos(\lambda x-\omega t)\boldsymbol{j}$ with $U(y)$ and $V(y)$ satisfying continuity $\lambda U + dV/dy = 0$. Here λ is the wavenumber and ω is the wave

frequency, and $\boldsymbol{i}$ and $\boldsymbol{j}$ are unit vectors in the respective x and y directions. For this case, the Eulerian mean velocity $\boldsymbol{u}_E$ is zero and the Stokes drift velocity reads $\boldsymbol{u}_S = d^2(V^2/4\omega\lambda)/dy^2\boldsymbol{i}$. The set of parameters T=10, λ=2π/16, U=0.02 are purposely chosen so that the analytical Stokes drift velocity $\boldsymbol{u}_S$=$\lambda U^2/2\omega\,\boldsymbol{i}$=1.25×10^{-04} $\boldsymbol{i}$ is of the same order of magnitude as those in the open-cavity flows presented in Section 4.1. Our numerical advection procedure and the formulation given in Chapter 3 and Eq. (5.4) predict a Stokes drift velocity within 0.5% of this analytical value.

5.2.4 Mesh Dependency and Streaming

For the 2D open cavity flow at Re=1, the flow solution is computed in three different meshes. The mesh details are given in Table 5.1. As the mesh is unstructured, the size of the closest node to the cavity corner is reported. The Eulerian mean velocity $\boldsymbol{u}_E$ is computed. The peak of the Eulerian mean is reported at the same location near the corner for all the three cases. The percentage error between the fine mesh and the very fine mesh is ~0.2%.

5.3 Mixing in 2D Open Cavity Flow

Before embarking on the analysis of flow structure and mixing in the 3D alveolar geometry, a representative 2D case is used to demonstrate various important, but not well-understood, mixing patterns, some of which had been reported before (Tsuda et al., 1995 and Henry et al., 2002). We will first discuss the steady-streaming phenomenon and its characteristics, and then relate it to the origin of various interface stretching and folding patterns observed in the duct, in the duct mouth, and within the cavity. Consider

an oscillating flow in a 2D long, straight channel with multiple rectangular grooves located periodically on the lower part of the channel as shown in Figure 2.1.

In the following presentation, the advection and observed drift are understood in relation to the Eulerian mean and Stokes drift velocities in Eq. (5.4). The axial and transverse components of Eulerian mean flow is shown in Figure 5.2. Note that the local maximum positive and negative axial Eulerian streaming velocities occur near the two corners of the cavity and are asymmetric in sign with respect to the vertical centerline of the cavity. The non-zero Eulerian streaming components are a result of asymmetries from non-zero-Re inertia effects, which do not cancel out between inspiration and expiration cycles. The distribution of non-zero axial mean in Figure 5.2 agrees with the asymmetry of the streamlines shown in Figure 4.2. Hence, the presence of a non-zero Eulerian mean flow is due to asymmetry in the fluid flow between the two half-cycles and the effect decreases with decreasing Re. On inspiration the fluid flows from right to left, and on expiration the flow is reversed (see Figure 4.2). The flow fields on inspiration and expiration become more asymmetric near the upper corners of the cavity than near the bottom because fluid in the channel experiences immediate expansion and contraction when flowing over the cavity. The Eulerian mean magnitude is about 3 orders smaller than the mean velocity of the fluid. Such non-zero mean flow effects are typically observed in other low-Re settings such as flow over a wavy bottom. For example, Larrieu et al. (2009) showed the formation of positive and negative peaks of Eulerian mean velocities observed between two crests of the wavy wall. Because the magnitude of the Eulerian mean velocity $\boldsymbol{u}_E$ is small, to assess the sensitivity of $\boldsymbol{u}_E$ on mesh size we present the comparison of the observed maximum Eulerian mean velocities for three different

mesh sizes. The results show that a mesh-independent solution is ensured. The "fine mesh" of Table 5.1 is henceforth used. Figure 5.3 shows the Eulerian mean velocity components for the shallow cavity case.

We now consider advection in three regions: the cavity, the cavity-channel mouth, and the outer channel. First, let us consider advection of particles inside the cavity. Let A_0-B_0 and C_0-D_0 denote the respective right and left vertical material lines (comprising a number of Lagrangian particles) at t/T=0 in Figure 5.4(a). The drifts of two initial vertical lines of particles at the end of one cycle are also displayed. At end cycle, the right line dye A_0-B_0 forms a fold denoted by 1-2-3-4-5 in Figure 5.4(a). On the other hand, the left line dye C_0-D_0 is almost reversed back to its initial location. The shapes of the two dyes at half cycle t/T=0.5, A_π-B_π and C_π-D_π, are displayed in Figures. 5.4(b) and (c), respectively. The locations of points (Lagrangian particles) 1, 2, 3, 4, and 5 at t/T=1 in Figure 5.4(a) are also marked along A_π-B_π at t/T=0.5 in Figure 5.4(b). At t/T=0 these points are aligned vertically along A_0-B_0. During inspiration, these points are advected upward toward the mouth region where non-zero streaming is dominant (see Figure 5.2). Point 1 is advected to the left wall of the cavity on inspiration, passing through positive and negative streaming zones and resting away from the non-zero streaming zone. The (uppermost) thin line marked by "I" in Figure 5.4(b) delineates the pathline of point 1 during forward excursion. On expiration, the pathline "E" almost follows the inspiratory pathline "I", which is expected in very low-Re flow. Point 1 and 5 experiences almost zero drift. Points 2, 3 and 4 spread along from negative to positive streaming zones. The resulting Lagrangian drift of the material line at end cycle in Figure 5.4(a) takes the shape of a fold with the under-shoot of point 2 to the left and the over-shoot of point 4 to the

right. For the left line C_π-D_π at end inspiration shown in Figure 5.4(c), only the tip of the dye reaches the peripheral lower portion of the positive Eulerian streaming zone, producing little drift.

To better understand the roles played by Eulerian mean and Stokes drift on the total (Lagrangian) drift, Table 2 compares the three terms of Eq. (5.4): Lagrangian streaming velocity ($\boldsymbol{u}_L$), Eulerian mean velocity ($\boldsymbol{u}_E$) and Stokes drift velocity ($\boldsymbol{u}_S$) for the five points along the right line A_0-B_0. For all the points, the independently calculated $\boldsymbol{u}_L$, $\boldsymbol{u}_E$ and $\boldsymbol{u}_S$ satisfy $\boldsymbol{u}_L \approx \boldsymbol{u}_E + \boldsymbol{u}_S$, (with average error of ~0.15%) again validating Eq. (5.4). The under-shoot of point 2 to the left and the over-shoot of point 4 to the right that forms a fold as illustrated in Figure 5.4(a) are reflected by the negative and positive y-component steady streaming velocities v_L.

Table 2 further shows the dominant contribution of Stokes drift to the total drift, suggesting the kinematic (or pathline-dependent) nature of the folding pattern. To further understand this kinematic nature, we shall examine the contribution of the instantaneous Stokes drift velocity $\boldsymbol{u}_I$ in Eq. (5.3) from various locations along the inspiratory and expiratory pathlines to the total Stokes drift velocity $\boldsymbol{u}_S$ ($=\sum \boldsymbol{u}_I/N$). Figure 5.4(d) shows the distribution of y-component instantaneous Stokes drift velocity v_I for point 1 (see the insert in the upper left corner where the inspiratory and expiratory pathlines are almost overlapped). On inspiration (solid line) v_I is negative, whereas on expiration (dashed line) v_I becomes positive. The time instants at the three locations along the pathlines in the insert are marked by the same symbols in the main plot. The distributions of v_I on inspiration and expiration are of nearly the same shape, but opposite sign. v_I reaches a local minimum or maximum when the particle reaches around the midway between the

left and right walls of the cavity. By inverting the sign of v_I for t/T=0-0.5 and reversing the time axis (t*/T=1-t/T) for t/T=0.5-1 as shown in the lower right insert, we can compare v_I of the same particle at approximately the same location, but opposite phase. On the left side of the peak value (in the lower insert), the dashed line is slightly higher than the solid line, signifying the net v_I that contributes to v_S when the particle is near the right upper corner (e.g., the triangle in the upper insert) is positive. On the other hand, on the right side of the peak value, the dashed line is slightly lower than the solid line, resulting in the negative net v_I that the particle experiences near the left upper corner of the cavity. The positive and negative local Stokes drift velocities cancel out at end cycle, resulting in nearly zero displacement in Figure 5.4(a) for point 1. This analysis suggests that if a particle is advected through positive and negative Eulerian mean regions and rests at a zero Eulerian mean region at end inspiration t/T=0.5, the total drift at end cycle may be zero due to the cancellation effect.

Next, particle advection and stretch rate maps are demonstrated inside the cavity for two purposes. First, it highlights the connection between particle advection and fluid kinematics reflecting through deformation of line elements expressed by Eq. (3.3). Second, it helps elucidate the behavior of stretch rate in association with Lagrangian drifts. Figures 5.5(a), 5.5(b), and 5.5(c) show a time sequence of the advection of Lagrangian particles at t/T=0, 0.5, and 1, respectively. Here, the particles initially fill a rectangle, expanding from previous two vertical line dyes to a surface, to map out the drift in the core region of the cavity. At end inspiration (Figure 5.5(b)) particles exhibit a spiral shape, equivalent to a combination of Figures 5.4(b) and 5.4(c). At end expiration (i.e. end cycle t/T=1) Figure 5.5(c) shows the majority of particles are reversed back to

their original locations, except that a series of folds are formed and distributed along a curved strip from the right wall to the bottom wall, and then to the left wall. Figure 5.5(d) shows the stretch rate map of the same region within the cavity. A tongue of higher stretch rate region surrounds an almost zero mixing core. The higher stretch rate region coincides with the advection map shown in Figure 5.5(c), indicating that the stretch rate can capture and distinguish the regions of small and large drifts. A higher stretch rate yields greater separation and fold of dyes.

Having demonstrated typical advection patterns in the cavity, we present results of advection and drift in the mouth region. The visualization of advection of a line dye for which periodic boundary condition has been applied is shown in Figure 5.6 and Figure 5.7. The initial line is stretched into multiple cavities at t/T=0.5 as shown in Figure 5.6(a). A large increase in length of the tracer during the positive half-cycle is noted. The dye is overlaid back on to a single cavity, resulting in an appearance of "layer structure" in the mouth as shown in Figure 5.6(b). This is equivalent to the pattern of advection that can be expected when a dye is placed periodically in the alveolar mouth of all cavities in a physical scenario. Figure 5.6(c) shows the final shape of the dye after one complete advection cycle, exhibiting multiple folds (as opposed to a single fold of the right line dye inside the cavity in Figure 5.6(a)). The origin of folding is also attributable to steady streaming and will be discussed next in conjunction with the drift characteristics in the outer channel.

Advection in particle motion in the outer channel is studied by releasing two vertical lines of particles in the channel adjacent to the two corners of the cavity. The final shape of the tracer after one cycle shows the Lagrangian drift from its initial

condition. Two values of d_E=1.2 and 5 are considered. As seen in Figure 2.1, the upstream channel length is d_EL. By this specification, $d_E \rightarrow \infty$ is a model with a single cavity in an infinitely long channel, and d_E=0 is one where the channel is completely lined with grooves with no spacing in between. The drifts of these line tracers at end cycle calculated from Eq. (3.2) are shown in Figures 5.7(a) and 5.7(b). Like Figure 5.6(c), multiple folding patterns, hereafter referred to as "fold structure", are observed. The number of folds is higher for d_E=1.2 than for d_E=5. Multiple folds in the tracer clearly indicate that two particles initially located close to each other might over-shoot or under-shoot its initial location as observed inside the cavity (Figure 5.5(a)), in the mouth region (Figure 5.6(c)), and in the outer channel (Figures 5.7(a) and 5.7(b)).

The advection characteristics of selected points (Lagrangian particles) 1, 2, 3, 4 and 5 marked in the dye for d_E=5 in Figures 5.7(b) and 5.7(c) for t/T=1 and 0.5, respectively, are studied. The initial vertical line tracer on the right hand side is stretched over multiple cavities at end inspiration t/T=0.5. Only a section of the stretched tracer is shown in Figure 5.7(c). Points 1 and 4 that consistently fall short of their initial positions (under-shoot) after one cycle are always located near the left corner of the cavity at end inspiration. On the other hand, points 2 and 5 that over-shoot their initial positions after one cycle are located at the right corner of the cavity at end inspiration. Point 3 which is almost traced back to its initial location is located over the channel at t/T=0.5. Table 2 shows that points 1 and 2 (or points 4 and 5) have non-zero y-component streaming velocities v_L of opposite signs, and the calculated $\boldsymbol{u}_L$, $\boldsymbol{u}_E$ and $\boldsymbol{u}_S$ satisfies $\boldsymbol{u}_L \approx \boldsymbol{u}_E + \boldsymbol{u}_S$ with an average error of 0.7%. Hence, it can be concluded that non-zero steady-streaming velocities combined with pathlines of particles that traverse over multiple cavities (due to

large K_C) result in the observed advection drift and folding patterns. The number of folds increases with increasing K_C (or decreasing cavity spacing). If a horizontal line dye is released in the mouth region as shown in Figure 5.6, the resulting fold structure covers the mouth region as shown in Figure 5.6(c). Unlike the fold structure formed at end cycle, the layer structure in Figure 5.6(b) is irrelevant to mixing and is observed at end inspiration when a number of stretched tracers appear periodically over multiple cavities.

Similar to the deep cavity case in Figure 5.7, line dyes are released in the duct of the shallow cavity case. Due to smaller depth of cavity, a dominant recirculation is not present inside the cavity. It is not the objective of this work to resolve smaller corner vortices inside the trough. The advection of two lines dyes produced the fold structure and hence further validates our claim that streaming resulting from non-zero inertial effects in an alveolated geometry are responsible for such a behavior. The presence of recirculation inside the cavity does not play a role in this observed dispersion phenomena. Axial dispersion in the channel caused by steady streaming shown in Figure 5.7 is quantified by Eq. (3.4). The data at the end of first cycle is used as the reference initial condition to remove the effect of initial transient drift in the first cycle, which is usually greater than subsequent cycles. This is because of larger increase of dye interface from a line to folds in the first cycle while the fold pattern is retained in subsequent cycles. The variance shows an exponentially increasing trend with cycle number as seen in Figure 5.9 for both cases d_E=1.2 and 5. Additional experiments were carried out and two important variables that alter the observed fold structure significantly were realized. These are the Keulegan-Carpenter number, K_C and geometrical ratio L/H (ratio of cavity length to

channel height). Nevertheless, an elaborate parametrical study and identification of critical threshold values of these parameters is beyond the scope of this paper.

In summary, the relation between advection, stretch rate, steady streaming, and Lagrangian drift has been established in a simple 2D channel flow for Re=1 and K_C=193. It is shown that a mechanism that leads to large increase in dye interface length exists in a low-Re flow that arises due to streaming. With the physical insights gained from this case, we proceed to report the results in 3D acinar models. Unlike the 2D channel flow, all cases, except one, presented below consider uniform expansion and contraction of the 3D duct and alveolar walls.

5.4 Three-Dimensional Acinar Mixing

The characteristics of the flows for Cases I and II were discussed in Chapter 4. In the proximal generations, the main cavity flow typically consists of a recirculation near the proximal wall. The only non-diffusive interaction between the duct and the alveoli occurs through an entrainment region. The presence of such an entraining flow is a consequence of expansion and contraction of alveolar walls. Hence the fluid exchange to and from the alveoli occurs through a region located near the proximal wall corner. Since steady streaming plays an important role in mixing as demonstrated before with a 2D alveolated channel flow, Figure 5.11(d) shows the contours of the steady-streaming Eulerian mean axial (y-component) velocity in the y-z plane of an alveolus for Case I with Re=1 (refer to Figure 5.10(d) for the location of the y-z plane). The positive and negative streaming velocities are observed in the proximal (right) and distal (left) corners of the alveolus, exhibiting the same feature as the 2D rigid-channel case in spite of the

3D moving wall. For a given Re, the major difference from the rigid-wall case is that the magnitude of the streaming velocity in the moving-wall case is slightly lower than that of the rigid-wall case and is more asymmetric, having greater positive streaming velocity than negative one. With increasing (decreasing) Re to 2 (0.52), the maximum Eulerian axial velocity increases (decreases) approximately by two-fold.

5.4.1 Tracer Advection and Deformation

In this section, we investigate the Lagrangian drift that arises in tracer transport in an alveolus. For the tracer advection experiments below we shall consider the alveolus 'ALV' marked in Figure 5.10(a). For clarity, different 3D views of the alveolus are provided in Figures 5.10(c) and (d). A cross-shaped dye is introduced within the cavity and its deformation is monitored for ten cycles to assess the effect of recirculation on mixing. A visualization of the final shape of the dye for three different flow conditions is shown in Figure 5.12. The four arms of the dye are numbered, aiming to observe advection in four regions of the cavity. The dye experiences an increase in the interface area due to the alveolar flow: ~45% increase for Re=2(Q_A/Q_D=0.0024), ~12% for Re=1(Q_A/Q_D=0.0047) and ~3.5% for Re=0.52(Q_A/Q_D=0.0095). Similar to the observed folding phenomena in the 2D case of Figure 5.5, a stretch of material into the proximal corner is observed due to steady streaming. Again indicative of the Re effects, the drift is more pronounced for Re=2 than Re=1 and for Re=1 than Re=0.52. In particular, at Re=2, blue arm #1 is folded and stretched toward the upper proximal wall, and arm #3 near the mouth region is also highly stretched. At Re=1, the recirculation zone is reduced (see Figure 4.3), and thus only stretch of arm #2 is evident. Arm #3 still experiences stretching

because of its proximity to the mouth region. At Re=0.52, the recirculation is absent (see Figure 4.3) and only the stretch of arm #3 seems significant. The increase in the red-blue interface area ratio is correlated as roughly quadratic with increasing Re (see Figure 5.12(d)). It is also useful to plot the ratio as a function of the flow ratio Q_A/Q_D defined earlier. The interface area increases almost exponentially with decreasing values of Q_A/Q_D.

Previously the advection and deformation of tracers inside the cavity are examined by a cross-shaped dye. Next, a planar tracer is advected for one full cycle. The tracer is constructed using ~20,000 particles and placed initially in the *y-z* plane shown in Figure 5.10(d). The advection is carried out in a complete 3D sense utilizing all the three velocity components. Figure 5.13 shows advection characteristics in the mid-plane for Case I, which are of particular interest for reasons discussed in Section 4.3 in association with steady streaming. For studying the characteristics of deformation within the alveolus, the advection pattern in strategic regions within the planar tracer are separately followed. These regions are depicted by different colors and illustrated in Figure 5.13. The blue tracer, on average, covers the region inside the cavity where recirculation (in the neighborhood of the 'center' point) is observed. Mixing in the neighborhood of the proximal region (associated with the 'saddle' point) within the alveolus is identified using the green tracer. As observed in Figure 4.8, the mid-plane contains a saddle point near the proximal cavity wall. The rest of the cavity is colored in gray.

The layered appearance of the gray tracer at end inspiration, as seen in the middle panel of Figures 5.13(a), 5.13(b), and 5.13(c), is a visualization of traverse of the tracer in multiple alveolar units and has already been discussed in conjunction with Figure 5.6.

Because the axial distance travelled is greater for Re=2 than Re=1, and for Re=1 than Re=0.52, the number of layers observed is higher in Figure 5.13(a) than Figure 5.13(b), and in Figure 5.13(b) than Figure 5.13(c).

Mixing within the alveolus is visualized by the deformation of the blue and green regions. For Re=2 the blue region at end inspiration t/T=0.5 is stretched in a manner similar to the 2D channel case shown in Figure 5.6(b). Recall that in the presence of alveolar and ductal wall expansion, the recirculation eddy is shifted toward the proximal wall to accommodate the entrained flow. Therefore, the blue dye can hardly reach the distal wall of the cavity. At end expiration (i.e. end cycle, t/T=1), the fold structure similar to the 2D case in Figure 5.6(c) is observed. The fold structure extends further up to the green tracer region. At the mouth region, the fold structure is also formed at t/T=1. The particle distribution at the mouth region in association with folds appears to shift to the proximal-wall side, closer to the entrainment layer, especially at Re=2. The appearance of fold structure implies mixing which will be quantified later. For Re=1, the blue tracer region is smaller than that of Re=2 because the size of the recirculation eddy reduces in size. A smaller recirculation yields smaller stretching of the blue tracer at peak inspiration (see Figure 5.13(b), middle panel). The fold structures inside the cavity and at the mouth region are also observed in Figure 5.13(b), bottom panel. For Re=0.52, there is no recirculation, nor a stagnation saddle point. The green tracer is almost restored to its original shape as shown in Figure 5.13(c), bottom panel. Nonetheless, the fold structure at the mouth region is still observed. We also performed advection experiment for tracers released within the cavity for Re=0.06 case mentioned earlier in Section 3.1. The net

displacement of particles within the cavity after 5 cycles is observed to be 3-orders of magnitude smaller than observed in the Re=0.52 case.

5.4.2 Stretch Rate Map

The spatial distribution of stretch rate, also known as a "stretch rate map", represents stretching histories of Lagrangian particles seeded over an area and computed using Eq. (3.3). First, stretch rate within the cavity is considered. Figure 5.14 depicts slices of stretch rate inside the alveolus in the y-z plane for Cases I and II. Relatively high-stretch-rate zones are limited to localized regions within the alveolus. In Figure 5.14(a), a tongue of high stretching surrounds a region of almost zero stretching, resembling the fold structure inside the cavity shown in Figures 5.5(c) and 5.5(d). The high-stretch-rate regions near the proximal wall in Figures 5.14(a) and 5.14(b) roughly correspond to the spreading of the blue tracer towards the proximal wall in Figures 5.13(a) and 5.13(b). The distributions of particle tracer after five cycles are superimposed on the stretch rate maps in Figures 5.14(a) and 5.14(b), confirming the physical correlation between stretch rate and tracer deformation. The shape and length of the tongue of this high-stretch region are dependent on the size and shape of recirculation and its advection of particles to the steady streaming zone as discussed in Section 5.3. When Re=2, the size of recirculation is larger. Hence the high-stretch tongue is larger in length, extending into the cavity. On the other hand, when Re=1, the size of recirculation is small and is more shifted towards the proximal wall, resulting in the observed high-stretch region in Figure 5.14(b). The stretch rate map for two alveolar units (marked in Figure 5.10(b)) for Case II with Re=1 are shown in Figure 5.14(c). As in Case I, the high-stretch

rate is observed near the proximal region. Although both Cases I and II in Figures 5.14(b) and 5.14(c) have the same Re at the ductal entrance, more alveolation in Case II enhances stretch rate by ~4 times. In addition, the left alveolus has higher stretch rate than the right one because of the geometrical effect.

In Figure 5.14(d), the stretch rate map at the mouth region of Case I with Re=1 is overlaid with the tracer distribution after five cycles. The high stretch-rate distribution is correlated well with the tracer distribution. Transport in this region represents the nature of duct-alveoli interaction. The stretch rate map in the alveolar mouth region is of higher complexity, stratified in appearance with alternating higher and lower values of contours, resembling the fold structure shown in Figure 5.6(c) due to steady streaming. It is noted that the stretch rate at the mouth region is an order-of-magnitude higher than inside the cavity, suggesting that stretching and folding of dye interface in the mouth region is much more effective than inside the cavity.

To correlate the high-stretch rate region (effective mixing region) inside the cavity with the flow topology (e.g. center and saddle critical points, recirculation and entrainment), Figure 5.15 overlays the stream-traces near peak inspiration with the stretch rate map. This suggests that the high stretch rate (effective mixing) takes places along the periphery of the recirculation and at the mouth region in association with entrained flow and it does not necessarily coincide with the saddle point. The center point of the recirculation at Re=2 appears to contribute little to mixing.

The time-averaged stretch rates shown in Figure 5.15 can be averaged over the entire flow field to get a single-value volume-averaged stretch rate at various conditions for comparison. The volume-averaged stretch rate thus obtained gives the mixing rate

solely determined by the kinematics of the flow, and is referred to as kinematic mixing rate. Figure 5.16 plots the variation of mixing rate with Q_A/Q_D and Re for the cases considered. The mixing rate is approximately equivalent to the separation rate of adjacent array of particles. The stretch rate in Eq. (3.3) is a logarithmic rate. Hence, if the average stretch rate is 's_l' after time 'nT', the approximate separation between particles roughly increases by $100(e^{s_l \times nT} - 1)\%$. The mixing rate for Case I is ~0.04 at Re=2 and ~0.005 for Re=1. The average separation between particles in the flow roughly increases by ~65% when Re=2(Q_A/Q_D=0.0024), and by only ~7% for Re=1(Q_A/Q_D=0.0047). The mixing rate is ~0.02 in Case II for Re=1(Q_A/Q_D=0.0047) and decreases to ~0.009 for Re=0.6(Q_A/Q_D=0.008). As illustrated in Figure 5.12(d), a rapid reduction in mixing rate is evident for both Cases I and II as Re decreases and Q_A/Q_D increases down the acinar tree.

5.4.3 Dispersion in an Alveolated Duct

While the previous section focuses on convective displacement of particles within the alveolus and at the alveolar mouth region, this section is primarily concerned with axial dispersion in the ductal region of the acinar airways. The streaming mechanism governing axial spreading of a dye in a 2D alveolated channel is analyzed in Section 5.3. Based on its definition, d_E=1.2 for Case I and d_E=0 for Case II. For the 3D geometry considered here, it is not surprising that a similar advection pattern would be observed. But the motion of the wall introduces some changes to the advection characteristics of particles close to the cavity. Unlike the rigid wall case, a fraction of particles from the duct and from the alveolar mouth penetrate deeper into the cavity during inspiration.

These particles may not return back to its original location. Also, the fraction of the particles entering the alveoli is small (observed to be less than ~2% when Re=1). The net dispersion of particles in the duct studied in this section is hence primarily attributed to the axial spreading mechanism. For illustrative purposes, the advection of a planar dye released in the duct near the proximal wall is displayed in Figure 5.17(a). Similar to the 2D-fold structure shown in Figure 5.6, a 3D-fold structure in the dye after one advection cycle is observed. This drift is the 3D equivalent of axial spreading caused by steady streaming as discussed before. We now proceed to quantify the observed dispersion in the axial direction.

A bolus consisting of ~40,000 particles are released in the entrance of the alveolar duct and advected through multiple cycles. Dispersion of the bolus is calculated by Eq. (3.4). The particle location at the first cycle is treated as the base state in Eq. (3.4) to remove the initial transient effect. Two different initial distributions of bolus with the same particle flux density, number/μm^3, are considered: (1) a parabolic distribution and (2) a uniform particle flux distribution. Both distributions are introduced at the entrance of the alveolar duct. Figures 5.17(b) and 5.17(c) show the evolution of axial variance for Case I and Case II at different Q_A/Q_D and Re. There exists significant difference in the estimated dispersion for the two initial distributions. For example, when Re=1, about 3-fold increase for Case I and 4-fold increase for Case II are observed at the end of five time periods as shown in Figures 5.17(b) and 5.17(c) clearly illustrating the accelerated dispersion due to streaming. The extent of the axial spread of the tracer increases as we move away from the centerline as evident in Figure 5.17(a). This can also be seen in Figure 5.7(b) for the 2D case, where the drifts of points 1 and 2 are smaller than those of

points 4 and 5. In an initial parabolic distribution, the concentration of particles decreases away from the duct centerline. Hence, dispersion of particles in a region of higher particle concentration, which is near the ductal center, is less. The importance of geometry on axial dispersion can be related back to the streaming mechanism discussed in Section 5.3. It is recollected that the variances in Figure 5.9 for the two cases of d_E differed significantly. Hence, it can be concluded that geometry plays a crucial role in the accurate estimation of dispersion in acinar airways. The effect of Re on the resulting dispersion is also significant. For example, variance in Cases I and II drops by one order of magnitude when Re is halved, for both initial flux distributions.

5.4.4 Advection in a Single Bifurcation Model

Just like the upper airways, the acinus also consists of bifurcations or branching causing a progressive reduction in Re along the acinar tree. Although the low-Re flow quickly assumes a parabolic velocity profile in the duct space at the end of one branch before entering the daughter branch, the role of the bifurcation on mixing is not completely known. The models in Cases I and II presented before cannot capture this effect as it requires an elaborate geometry of the entire acinus although certain efforts in this direction have been attempted recently. For example, Harrington et al. (2006) and Sznitman et al. (2009) have performed computations of aerosol in a bifurcation model. But none of these works have performed advective mixing analysis or dispersion estimates.

Hence, advection in a single bifurcation model is briefly considered here. The model and the flow structure in this geometry have already been described in previous

chapters. The computation of advection in this model and the implementation of periodic boundary condition is tricky. Unlike the geometries of the honeycomb like alveolar duct in Cases I and II, the single bifurcation model has two exits. The following methodology is implemented. Three sets of fluid simulations were performed with peak Reynolds number, Re=1, 0.5 and 0.25 respectively. Here, the Reynolds number is based on the velocity at the entrance of the parent duct at peak inspiration. Since the velocity profile at inlet is prescribed as parabolic in nature, the maximum of the parabolic velocity at peak inspiration (t/T=0.25) is taken as the reference velocity to compute this Reynolds number. The same geometry is used for all three simulations. The walls of the geometry do not move and remain rigid. Particles are released in the entrance of the geometry at Re=1 which is at the top of the tree structure shown in Figure 5.18. As the particles advect through the domain, it reaches one of the two exits (each with peak Reynolds number 0.5). These particles are then suitably transferred to the entrance of the geometry and the solution now proceeds using Re=0.5 flow solution. This process is continued for one complete cycle. This transfer of particles from one exit to the next entrance is straightforward and performed as illustrated in Figure 5.18. Three sets of flow solution are used. Re=1 flow solution is indicated by single solid line. At the ends of this geometry are attached Re=0.5 solution indicated by tri-striped lines. Finally, the Re=0.25 constitute the last two generations and are indicated in thicker solid line. The schematic of the final generational structure that results from such an implementation is shown in Figure 5.18(a). The exit planes of two daughter branches are shown in Figure 5.18(b). The exit plane is divided into 12 triangular regions. As the particle ‘P1’ (or P2) exits through this plane, the triangle through which the particle advected out is established. In

this figure, particle 'P1' (or P2) is located in triangle 1-2-O. The boundary of this polygon is suitably matched with the entrance boundary of the parent domain into which the particle will be transferred. Once the particle is suitable transferred, the velocity of the particle at its new location is now obtained using the CFD solution in that domain at that timestep. The advection then proceeds as usual. The results of advection of a line dye released at four different locations are shown in Figure 5.19. One dye is released in the alveolar duct in the xy-plane, another dye in the yz-plane and two other dyes are released at the entrance of the alveolus. Unlike the single branch straight chain model (implemented using the periodic boundary condition) of Cases I and II, the advection is not negligible in the centerline of the model. This is obvious as the particles in the dye which are located near the centerline in one generation may be advected to regions closer to the alveolar mouth in the next generation. Elaborate analysis of dye advection or dispersion will not be carried out. The main objective of this effort is to demonstrate the fact that the process of streaming and resulting fold-like mixing pattern observed in earlier sections of Cases I and II are inherent dispersion mechanisms of oscillatory flows in alveolar geometries and are inevitably present even in the presence of branching. The results of advection in Figure 5.19 clearly illustrate this. In all these figures, the blue line is the initial shape of the dye at t/T=0. The final shape of the dye is in black. Considerable differences are observed for a dye released in xy-plane versus the one released in yz-plane. This is due to the three-dimensional geometric structure of branching. Note that one limitation of this model is the choice of only three simulations Re=1, Re=0.5 and Re=0.25. This gave rise to a 4-generational acinar tree structure as can be seen from Figure 5.18. Hence, particles that (possibly) might exit the tree from generation 4, which

are exits of Re=0.25 model, or at the end of one complete cycle advect out of the entrance of Re=1 model and overshoot its initial location at time t/T=0 cannot be accounted by the model. But for our current purposes, we have clearly established that the folding of material interface due to alveolation exists even in a branched (tree-like) structure.

5.5. Discussion

Cavities, in general, are stagnant pockets, which show weak material transport characteristics unless modified by some form of temporal perturbation (Horner et al., 2002). Alveolar flow is a time-periodic low-Re phenomenon occurring in open cavities. The extent of mixing achieved by low-Re acinar flow, under normal breathing conditions, reversible wall motion and perfectly sinusoidal ductal flow is the topic of investigation in this chapter. Improved understanding of acinar mixing helps in better prediction of particle transport, dispersion and the ultimate deposition of fine particles deep in the lung. For example, bolus dispersion studies cannot individually simulate flow and transport in each region of the acinus, due entirely to its complexity. Mixing factor is a term commonly used in these studies to denote the fraction of particles transported from the inhaled to residual air in the alveolar region. This factor is mostly empirical and accounts for the flow-induced mixing. Its importance can be quickly realized from the observation (Hofmann and Koblinger, 1990; Hofmann et al., 2008) that 0.5-1 μm particles show an order of magnitude difference in deposition fraction between cases of zero and total mixing. Hence, obtaining time-averaged mixing estimates is a main objective of this work.

The mixing measures rely on the estimation of particle motion due to non-zero inertia and geometry. The important contributions of this paper may be summarized as follows. Acinar flows belong to a unique category of low-Re high K_C oscillatory flows. An open cavity geometry is used as a simple prototype for alveoli, to observe a Lagrangian drift and hence an increase in interface length. This is shown to result in advective mixing studied from different viewpoints - mixing in the duct, mixing within the alveolus and their interaction. The origin of the Lagrangian drift in these regions can all be explained by the steady-streaming phenomenon in an oscillatory flow. Using this basic understanding of the mechanism, estimates such tracer deformation, stretching and dispersion are used to quantify this advective mixing in 3D acinar models. Critical points in the flow are also identified within the cavity based on an analysis of eigenvalues computed from the velocity gradient in the mid-plane. However, they are not physically correlated with regions of high stretch rate.

The steady-streaming mechanism also accounts for considerable axial dispersion in alveolated channels and ducts. Such a drift mechanism exists due to alveolation even in the absence of wall motion. Previously, Henry et al. (2002) observed a 'finger-like' stretch of the dye interface in their multi-cell alveolar model. Their model was one of expanding and contracting during one cycle. The exact origins of this finger-like structure in the tracer advection were not discussed. Also, it was reported that the formation of this structure in the duct was associated with the presence (or absence) of recirculation. On the contrary, our analysis and results clearly indicate that the presence of recirculation inside the cavity have no bearing on the observed drift in the dye. Instead, the observed drift in tracer transport is of hydrodynamic origin and can be directly correlated to steady

streaming. Such low-Re hydrodynamic streaming-induced phenomenon has been recorded earlier in different environments. For example, Flekkoy et al. (1996) observed similar 'pinch' dispersion of tracer in a Hele-Shaw cell in the presence of an obstacle. More recently, Larrieu et al. (2009) observed Lagrangian drift for oscillatory flow over a wavy wall due to streaming. Wang and Ottino (2009) observed that increasing K_C increases disorder in tracer motion in a lid-driven cavity flow. The present finding is unique to low-Re open cavity flows directly applicable to dispersion in acinar airways with a large displacement parameter, K_C.

We have also supplemented our mixing study with stretching analysis. Haber et al. (2000) investigated flow inside a hemispherical cavity. In their study of mixing, stretching was computed using $(\underline{D}:\underline{D})^{1/2}$ where the velocity gradient tensor $\underline{D}$ was calculated through advection of an array of particles, although they did not arrive at a parametrical mixing estimate. The stretch rate map for Case I agree qualitatively with those of Haber et al. (2000) showing higher stretch rate near the proximal wall.

The conclusions presented thus far have important physiological implications with respect to the fate of inhaled pharmaceutical and pollutant particle clouds in the acinus. In the adult human lung, less than ~13% of alveoli originate from bronchioles in the first three acinar generations, while almost ~87% originate from alveolar ducts and sacs[8]. Under normal breathing conditions, Re is typically 0.6-1.0, for the first few acinar generations. Hence, when one neglects gravitational and diffusional mechanisms, advective mixing of an inhaled bolus could originate in respiratory bronchioles (and more significantly for Re>1) and may extend up to the beginning of alveolar ducts. In the later generations (when Re≤0.52), the flow induced dispersion and the resulting convective

mixing inside the cavity are negligible. But, the unique combination of low-Re, high-K_C oscillatory shear flow in the presence of an expansion (in the form of alveolar cavity) causes non-negligible dispersion in the alveolar duct. The low-Re flow in distal generations could still achieve effective mixing through other mechanisms like parent-daughter branching, hysteresis in wall motion and ductal-alveolar flow phase lag (Haber et al., 2000) and is a topic of future work. The extrapolation of the mixing measures and correlations to the entire acinar region of the lung should be done with caution and the predictions may not completely hold true in the lung in-vivo.

Table 5.1 Mesh sensitivity test for Eulerian mean velocity

Mesh Case	**Coarse Mesh**	**Fine Mesh**	**Very Fine Mesh**
Number of elements	11000	25200	85500
Element size near the corner (Δ/L)	0.01566	0.0087	0.004475
Maximum (axial) $\boldsymbol{u}_E$ magnitude × 1000	1.367	1.377	1.38

Table 5.2 Lagrangian streaming, Eulerian mean and Stokes drift velocities for points 1, 2, 3, 4 and 5 inside the cavity marked in Figure 5.4(a).

Point	**Lagrangian streaming** (u_L, v_L)	**Eulerian mean** (u_E, v_E)	**Stokes drift** (u_S, v_S)
1	3.943E-005, -5.693E-005	-4.681E-006, 5.807E-006	4.412E-005, -6.215E-005
2	1.478E-004, -3.257E-004	-1.244E-006, 1.751E-006	1.491E-004, -3.266E-004
3	3.931E-007, 1.919E-006	-1.022E-006, 1.455E-006	1.286E-006, 9.840E-007
4	-1.507E-003, 6.737E-004	-7.970E-007, 1.131E-006	-1.507E-003, 6.726E-004
5	-2.253E-006, 5.470E-006	-1.295E-007, 2.309E-009	-2.121E-006, 5.467E-006

Table 5.3 Lagrangian streaming, Eulerian mean and Stokes drift velocities for points 1, 2, 3, 4 and 5 in the outer channel marked in Figure 5.7(b)

Point	**Lagrangian streaming** (u_L, v_L)	**Eulerian mean** (u_E, v_E)	**Stokes drift** (u_S, v_S)
1	3.585E-004, -1.073E-003	-7.160E-004, 1.061E-003	1.074E-003, -2.141E-003
2	-8.467E-005, 1.749E-003	-6.889E-004, 1.047E-003	6.027E-004, 6.955E-004
3	4.805E-006, 2.671E-006	-5.547E-004, 9.521E-004	5.566E-004, -9.621E-004
4	6.922E-004, -1.315E-003	-3.810E-004, 7.502E-004	1.076E-003, -2.076E-003
5	-6.687E-005, 2.689E-003	-3.529E-004, 7.097E-004	2.869E-004, 1.972E-003

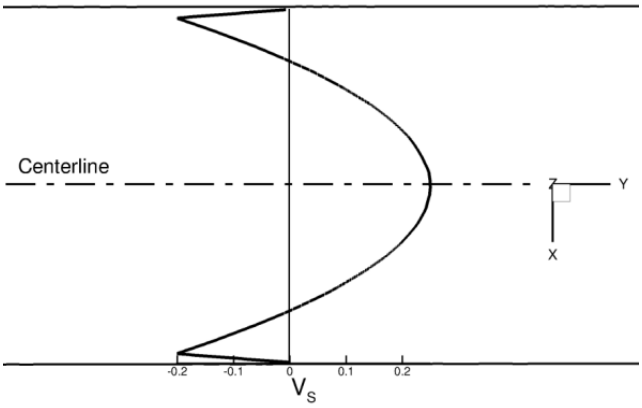

(a) Axial streaming velocity

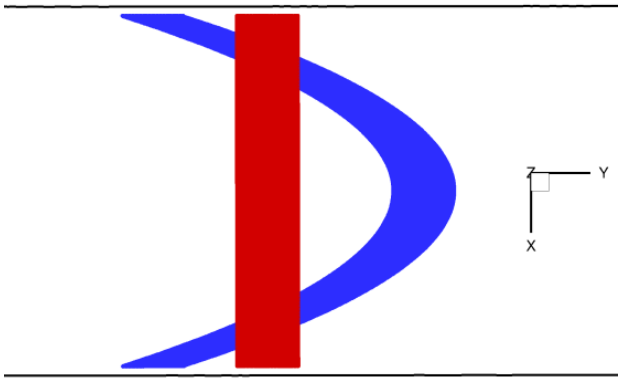

(b) Transport Profile

Figure 5.1 Illustration of steady streaming and the resulting transport of particles in a pipe flow. (a) Axial component of the streaming velocity. (b) Transport profile of a flux of particles. Red region is the initial flux at t/T=0. Blue region is the final transport profile at t/T=1.

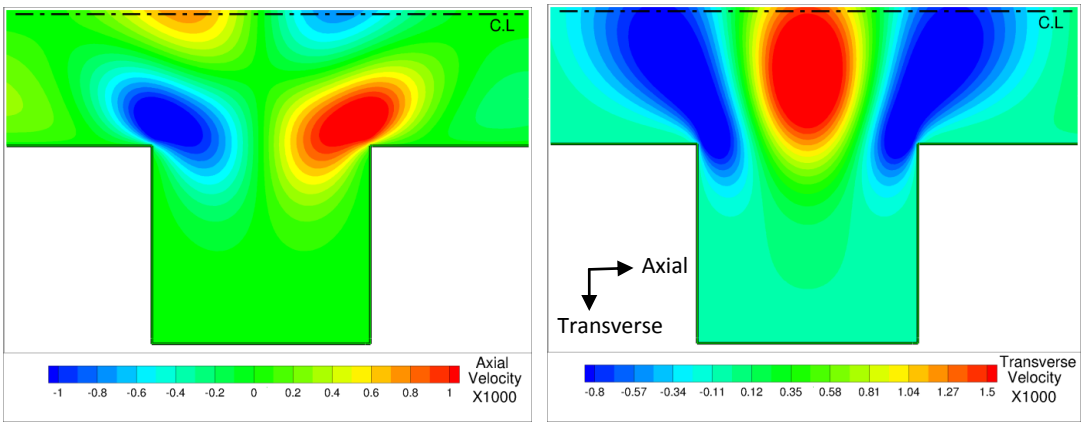

(a) (b)

Figure 5.2 Contours of Eulerian mean velocities computed using Eq. (5.1) in deep cavity flow for Re=1: (a) Axial velocity (y-component) and (b) transverse velocity (x-component).

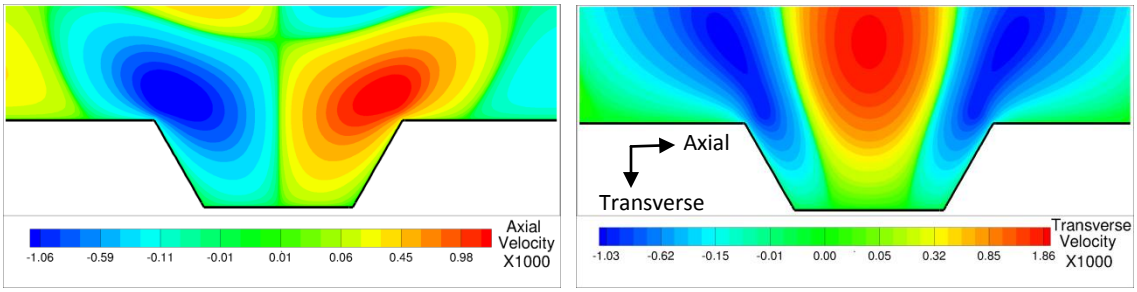

(a) (b)

Figure 5.3 Contours of Eulerian mean velocities computed using Eq. (5.1) in shallow cavity flow for Re=1: (a) Axial velocity (y-component) and (b) transverse velocity (x-component).

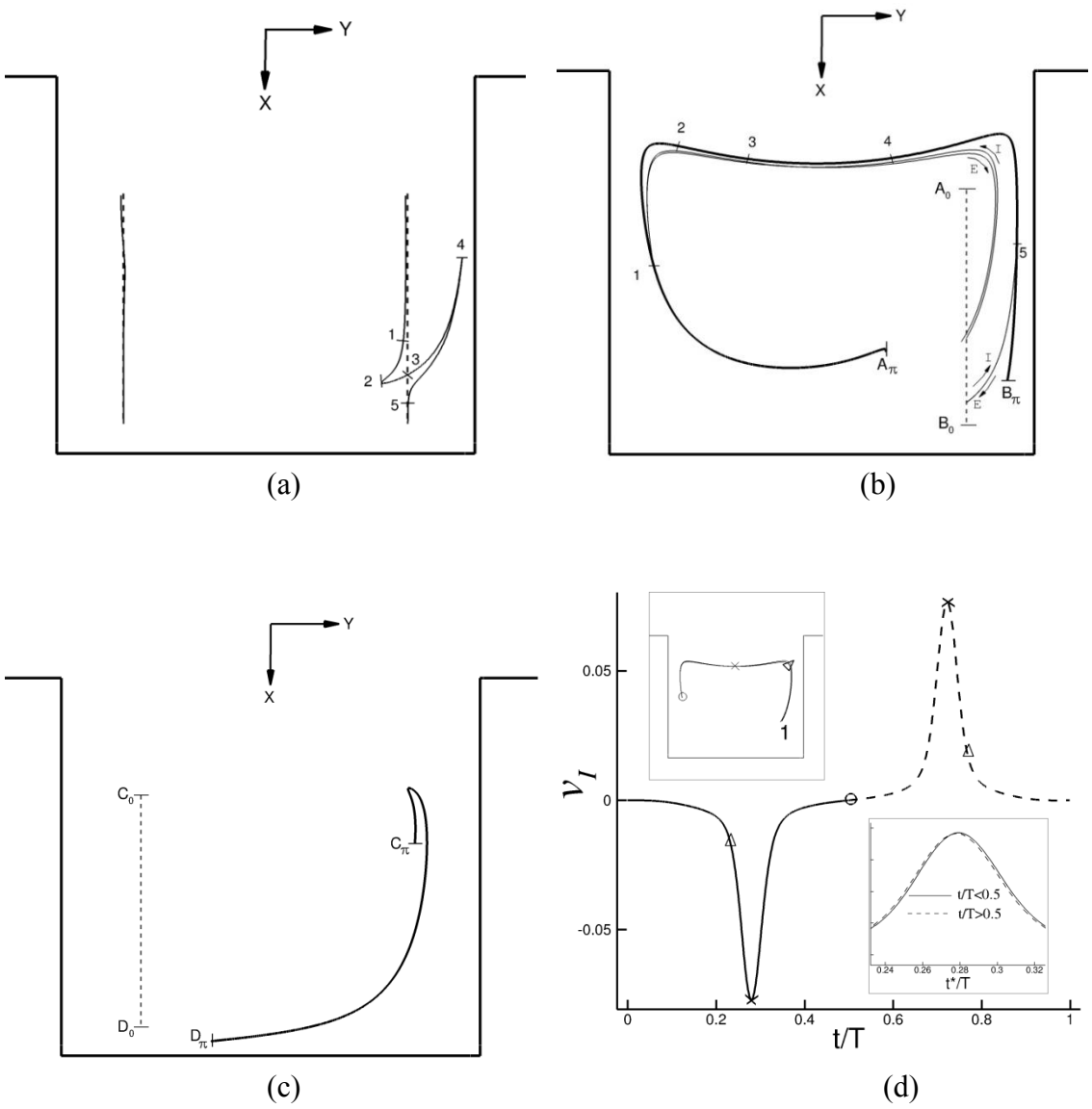

Figure 5.4 (a) Drifts (solid line) of two initially vertical line dyes (dotted line) at end cycle t/T=1. (b) Location of line dye A_o-B_o at end inspiration t/T=0.5, A_π-1-2-3-4-5-B_π. Points 1-2-3-4-5 correspond to those in (a). The pathlines for points 1 and 5 on inspiration and expiration (marked by I and E, respectively) are also plotted. (c) Location of line dye C_o-D_o at end inspiration t/T=0.5, C_π-D_π. (d) The distribution of y-component instantaneous Stokes drift velocity v_I for point 1 over one period. The instants at the three locations along the pathlines in the upper left insert are marked by the same symbols in the main plot. In the lower right insert, the inspiratory curve with an inverted sign (solid line) and the expiratory curve with the reversed time t*/T=1-t/T (dashed line) are overlapped to compare their magnitudes.

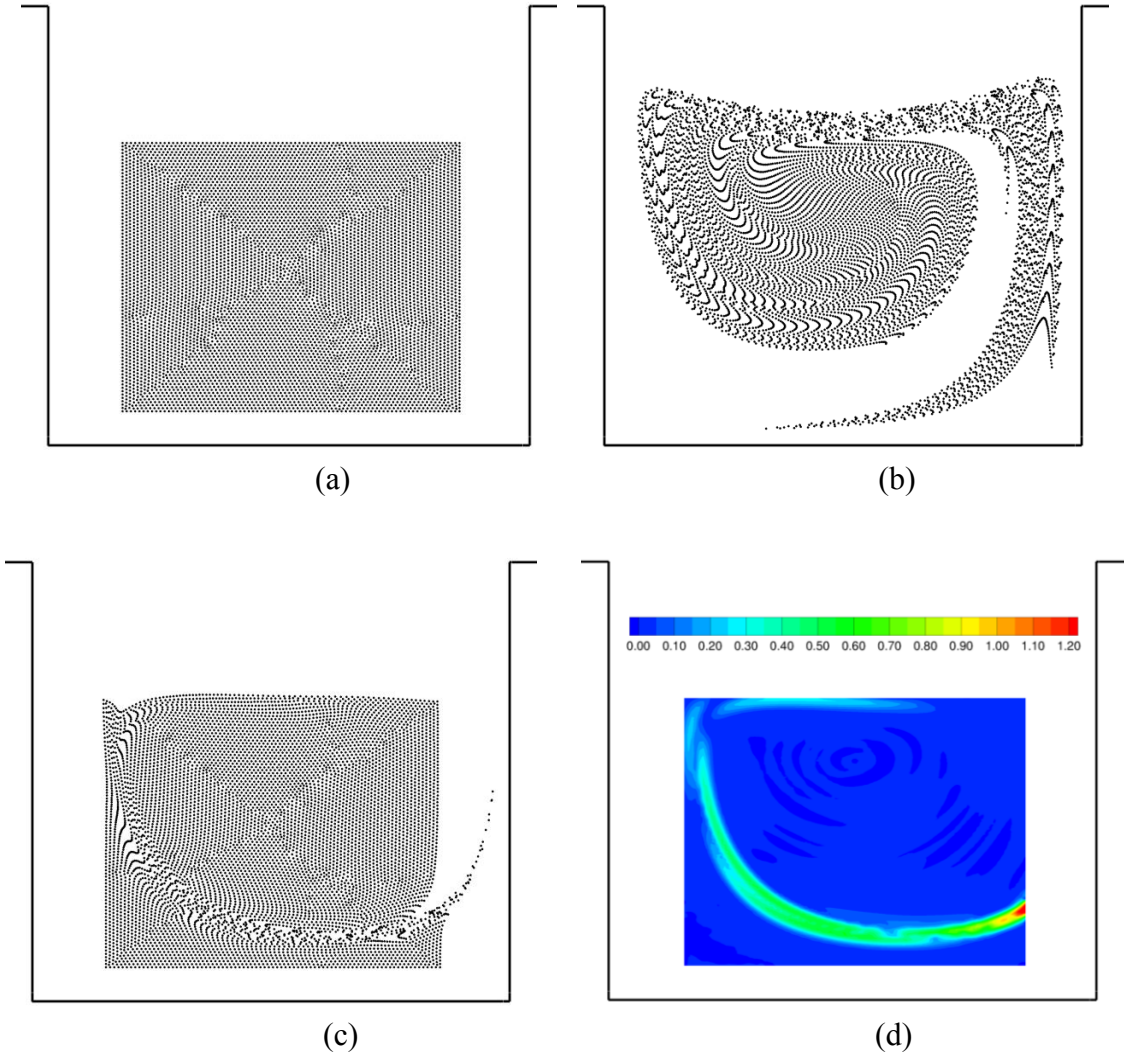

Figure 5.5 Tracer advection in the cavity of a 2D channel flow with Re=1. Distributions of tracer particles at t/T=: (a) 0, (b) 0.5, and (c) 1. (d) Stretch rate map calculated in the same region as (a) within the cavity.

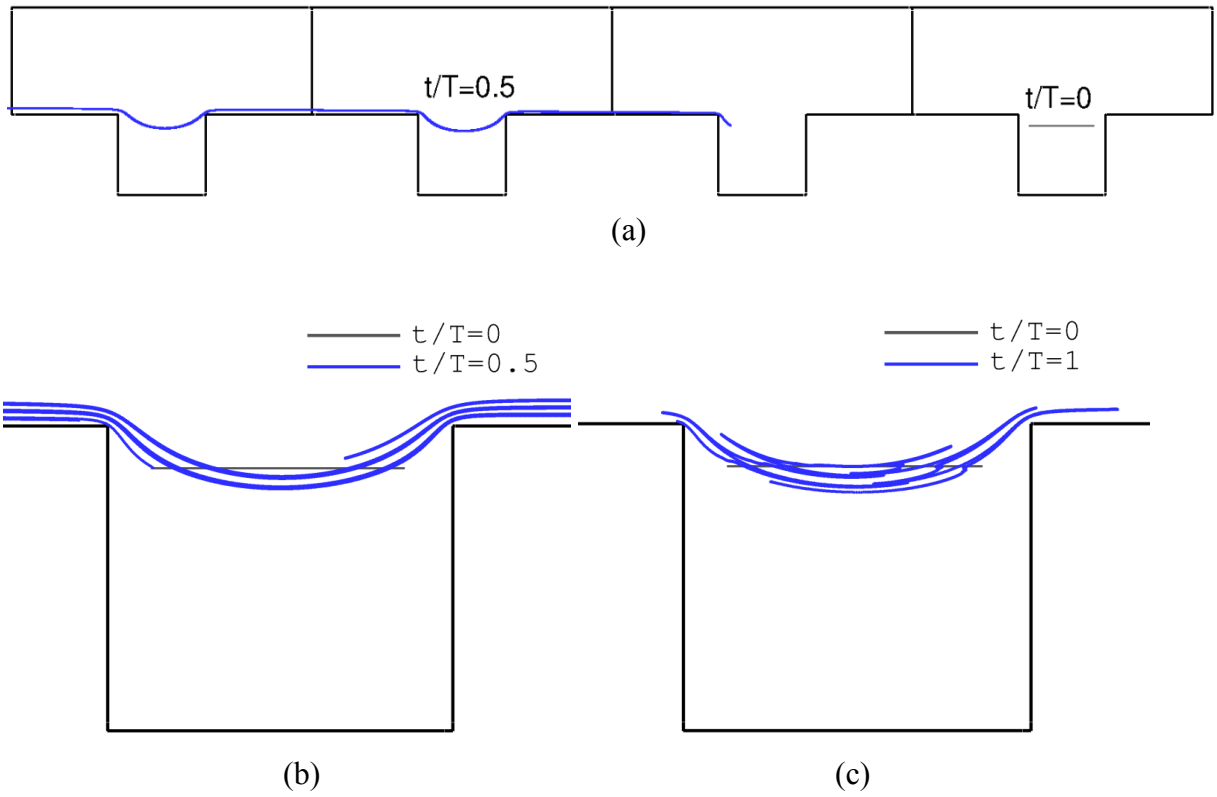

Figure 5.6 Tracer advection in a 2D channel with d_E=1.2. (a) Advection of an initial line dye (gray) into multiple cavities downstream is shown in blue. (b) Appearance of layer structure at end inspiration t/T=0.5. The dye in multiple cavities shown in (a) is overlaid on to a single cavity due to periodicity. (c) Fold structure is formed after one cycle at t/T=1 and covers the cavity-channel mouth region.

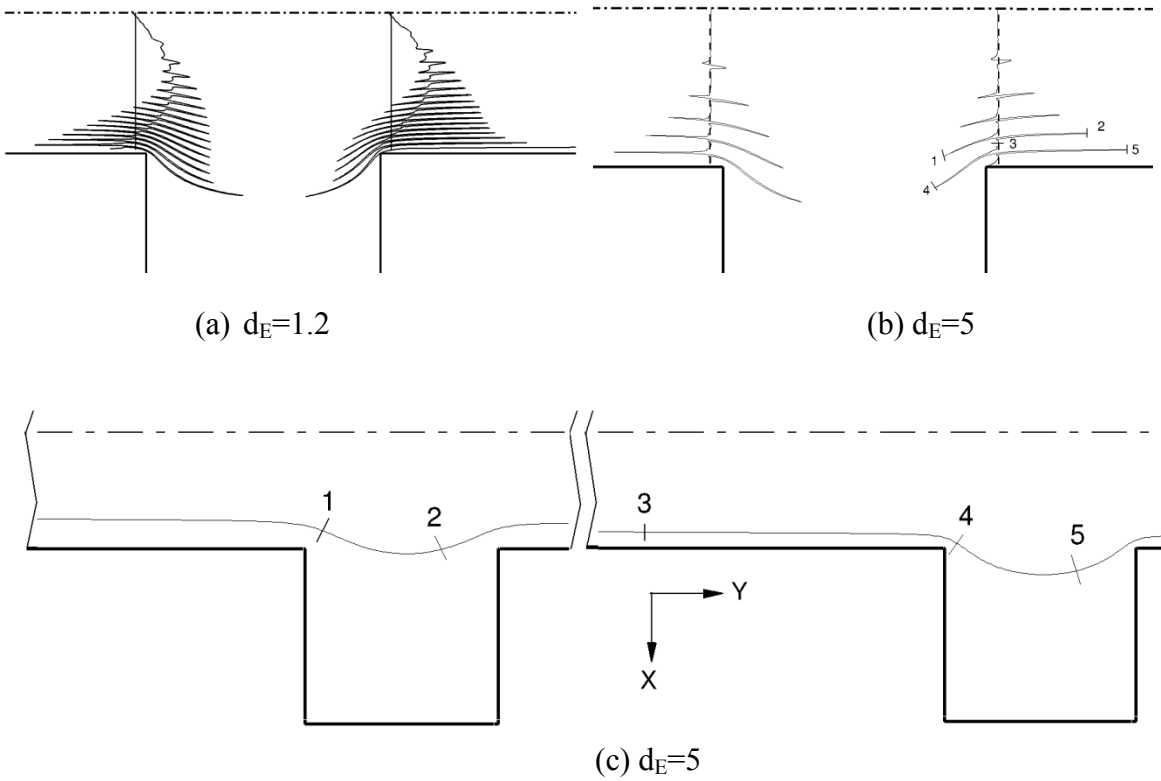

(a) d_E=1.2 (b) d_E=5

(c) d_E=5

Figure 5.7 Drifts of two line dyes in the channel near the two cavity corners for d_E=: (a) 1.2, (b) 5. (c) Locations of points 1-2-3-4-5 at end inspiration t/T=0.5. Their locations at end expiration t/T=1 are marked in (b).

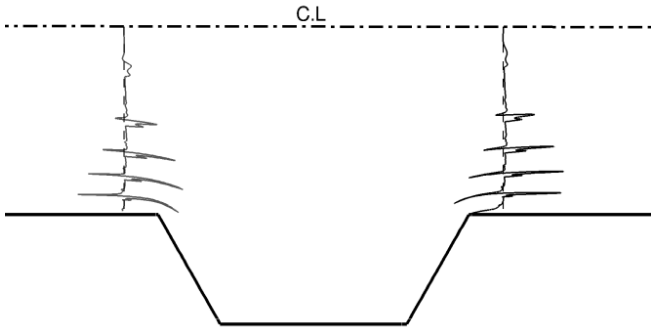

Figure 5.8 Shallow cavity case for d_E =5, Re=1: drifts of two line dyes in the channel.

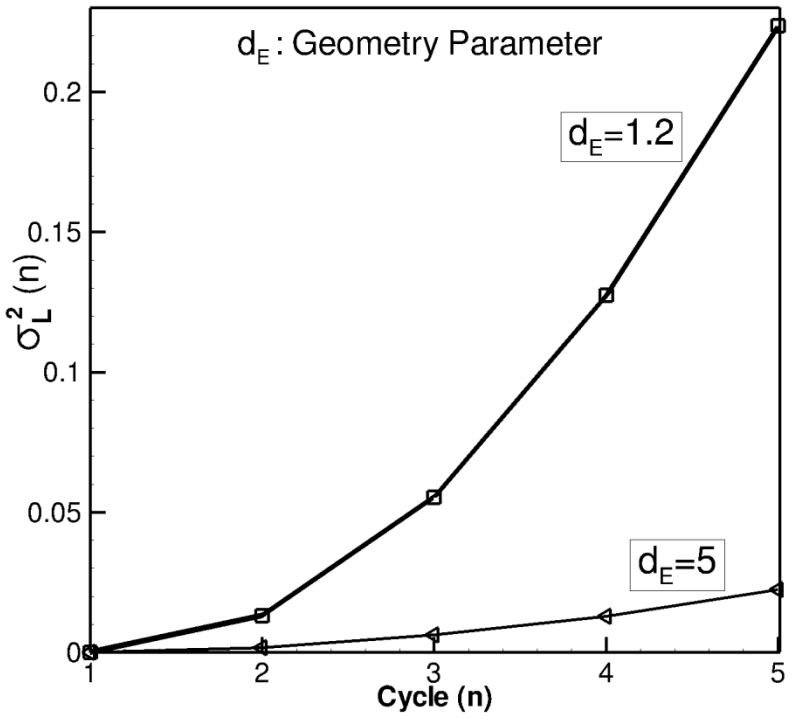

Figure 5.9 Axial dispersion quantified by axial variance as a function of number of cycle. Subscript 'L' is used for variance to indicate that the computation is carried out on the right vertical line of tracer shown in Figures 5.7(a) and 5.7(b).

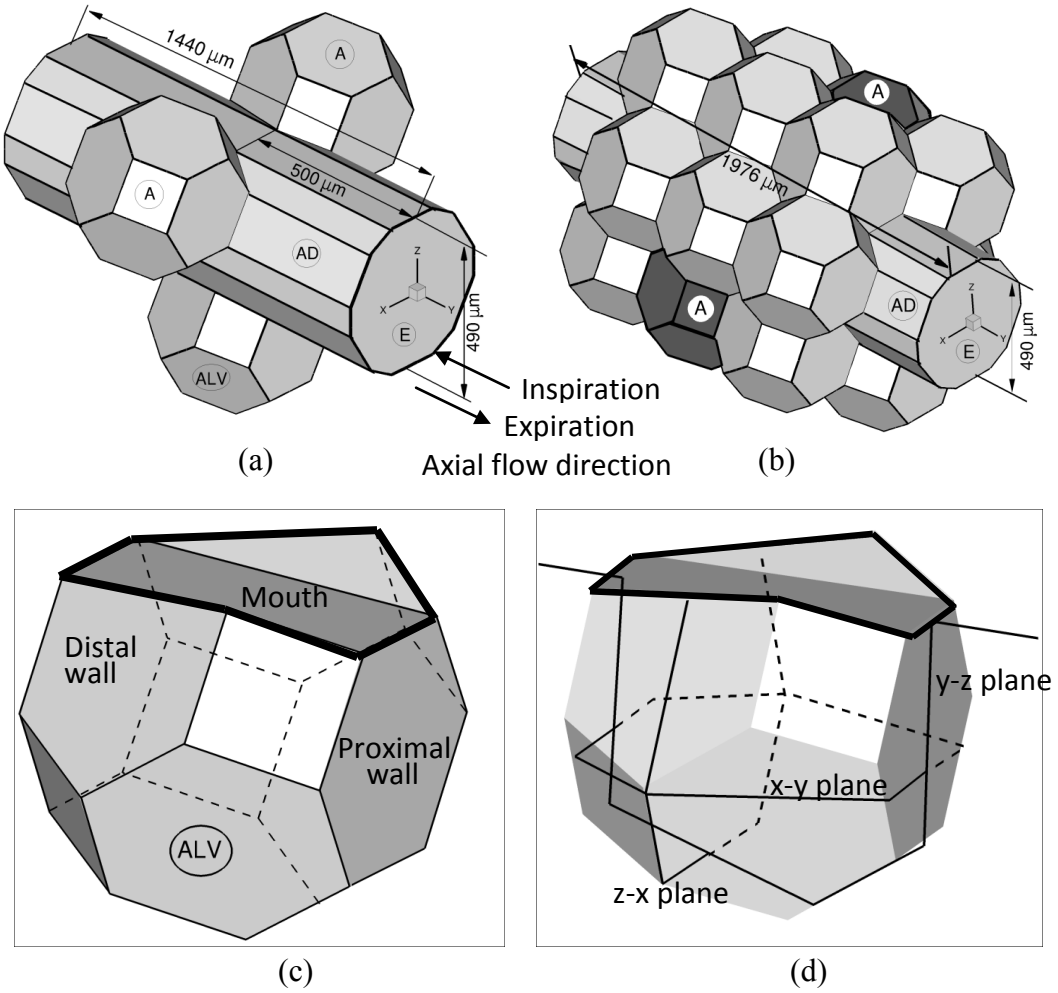

Figure 5.10 Representative geometrical models for regions of the acinus. (a) "Case I" model for respiratory bronchiole, (b) "Case II" model for alveolar duct, where (A, AD, E) denote (alveoli, alveolar duct, ductal entrance), (c) and (d) shows two presentations of an alveolar sac, denoted by ALV in (a) to be analyzed in Section 5.4. (c) ALV with solid and dashed edges for front and rear faces, respectively. (d) ALV with three planes to show the orientation of the unit. The y-direction is the axial direction. Some results are displayed in the y-z plane for clarity.

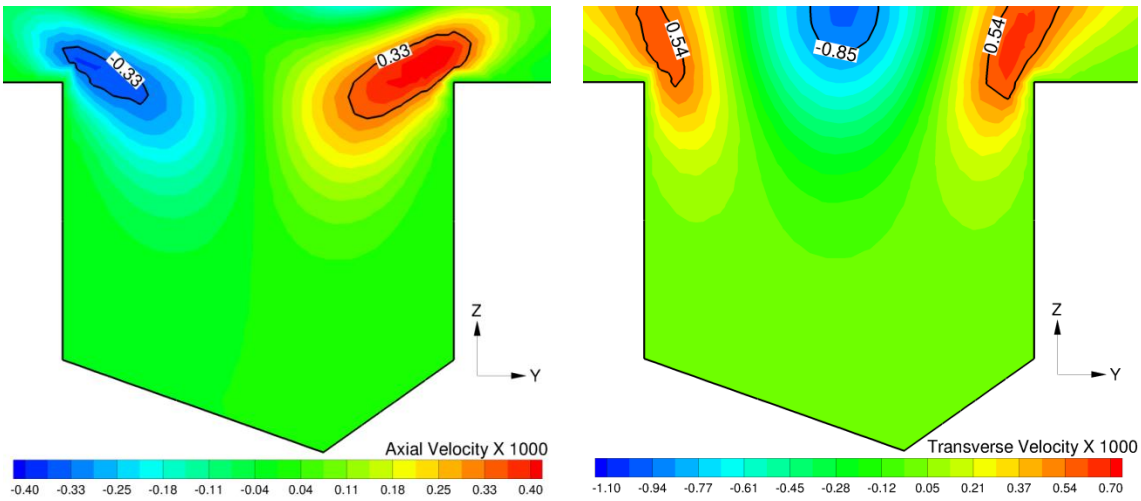

Figure 5.11 Contours of steady streaming-Eulerian mean (a) axial (y-component) velocity (b) Transverse (z-component) in the y-z plane of the cavity "ALV" for Case I with Re=1.

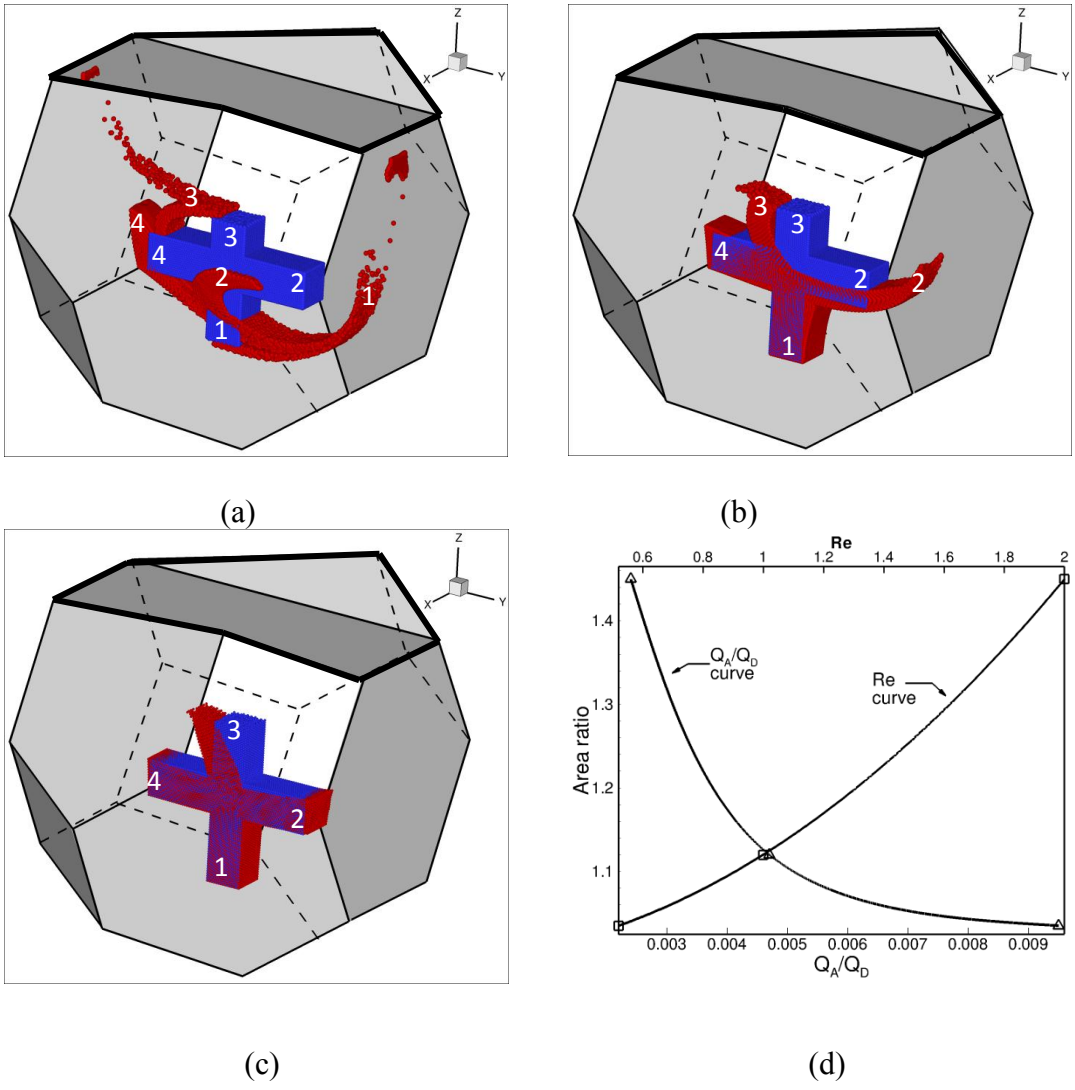

Figure 5.12 Advection patterns for an initial cross-shaped dye within the cavity "ALV" of Case I for (a) Re=2; Q_A/Q_D=0.0024, (b) Re=1; Q_A/Q_D=0.0047, and (c) Re=0.52; Q_A/Q_D=0.0095 after ten periods of breathing. The blue dye is the initial shape of the dye and the red dye is the deformed shape after advection. (d) Correlation of red-blue interface area ratio with Q_A/Q_D and Re.

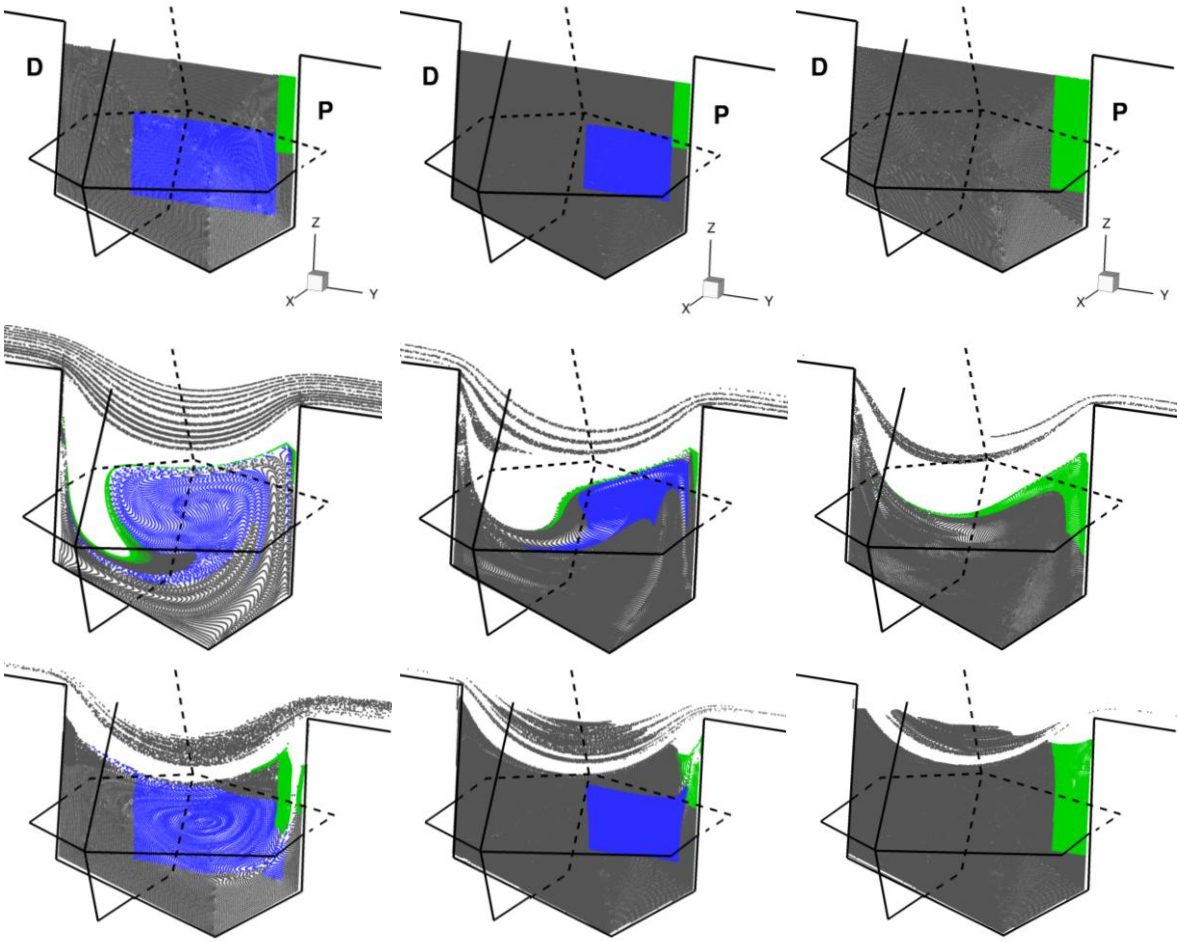

(a) (b) (c)

Figure 5.13 Material advection in the y-z plane of the cavity "ALV" of Case I (see Fig. 10(d)) with (a) Re=2; Q_A/Q_D=0.0024 (b) Re=1; Q_A/Q_D=0.0047 (c) Re=0.52; Q_A/Q_D=0.0095 at t/T=0 (top panel), 0.5 (middle panel), and 1.0 (bottom panel). P, proximal wall; D, distal wall. The blue (green) dye in (a) and (b) covers a center-like spiral point (a stagnation saddle point). There is no critical point in (c) due to very low Re.

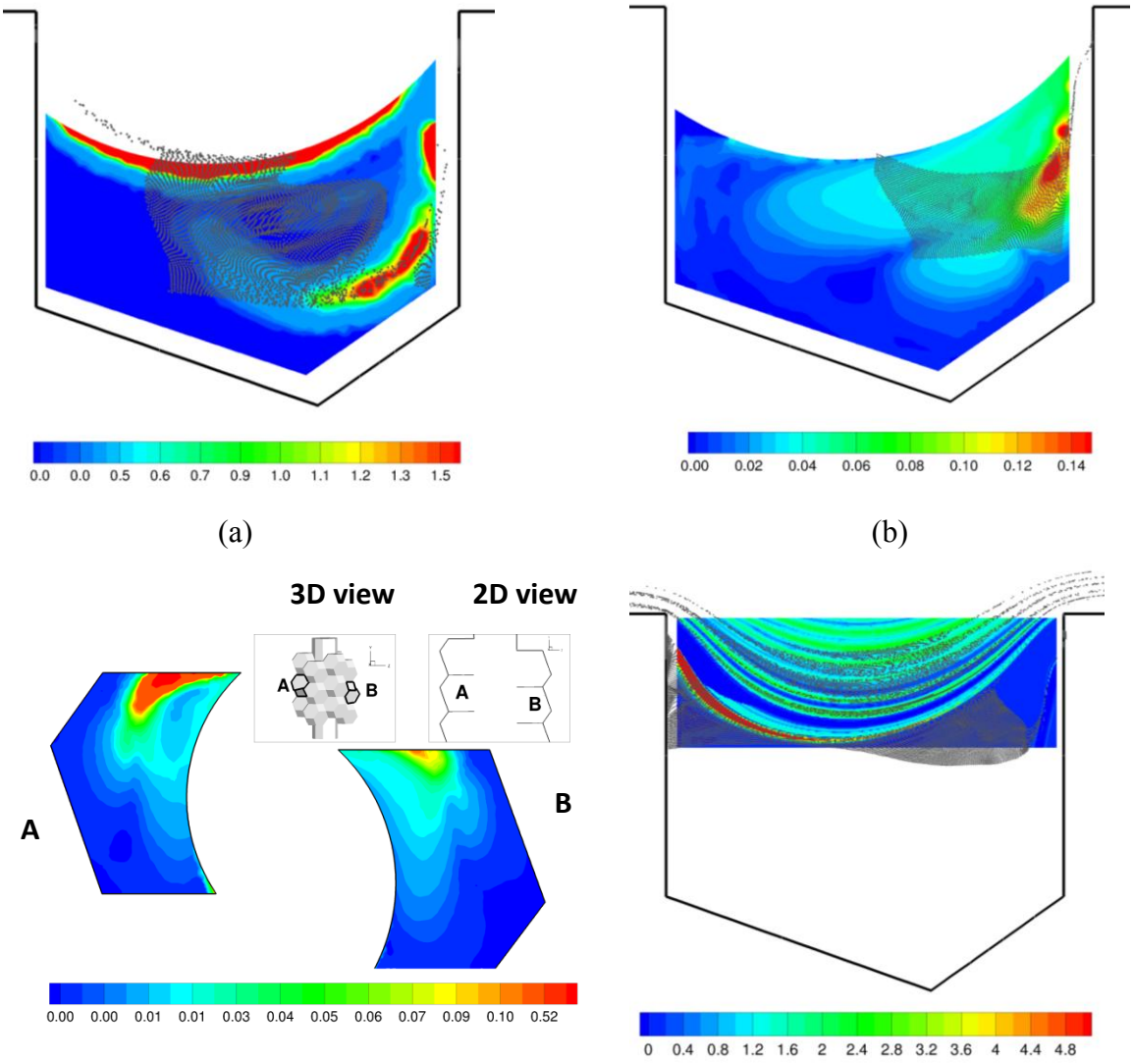

Figure 5.14 Maps of stretch rate (s_l) after five cycles in the y-z plane of the alveolar cavity for: (a) Case I, Re=2.0, Q_A/Q_D=0.0024, (b) Case I, Re=1, Q_A/Q_D=0.0047, (c) Case II, Re=1; Q_A/Q_D=0.0047, (d) in the mouth region of Case I, Re=1. For Case I the alveolus "ALV" in Figure 10(a) is examined. For Case II two alveoli marked by "A" and "B" in the two inserts of (c) are examined with the left one "A" closer to the ductal entrance "E". The distributions of particles covering the recirculation region of Case I (the blue dyes in Figures 5.13(a) & 5.13(b)) after five cycles are overlaid with stretch rate maps in (a) and (b), and the distribution of particles in the mouth region is overlaid in (d).

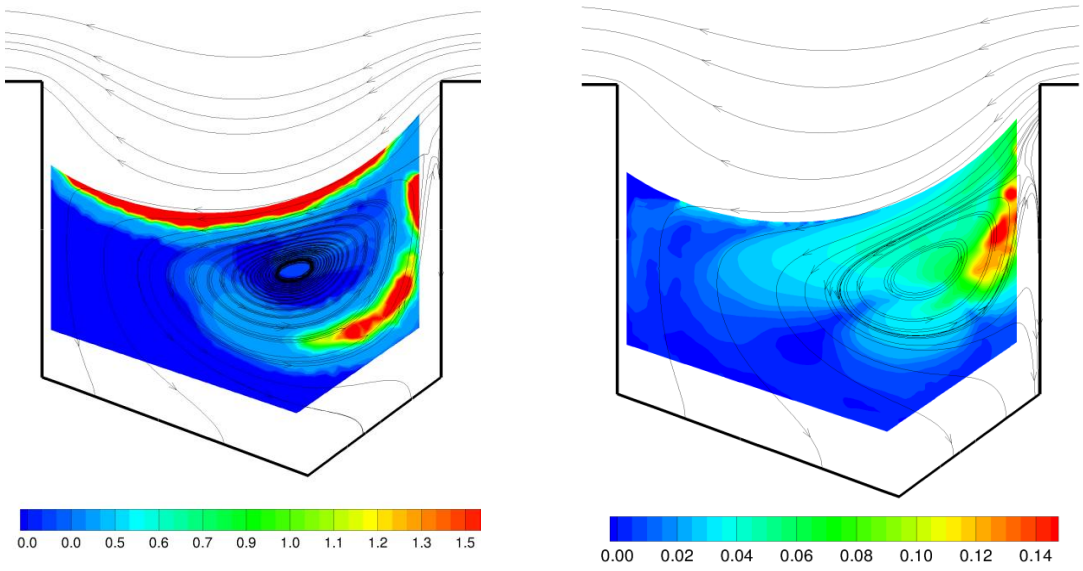

(a) (b)

Figure 5.15 Stream-traces near peak inspiration at t/T=0.24 overlaid with stretch rate map for Case I with Re=: (a) 2, (b) 1.

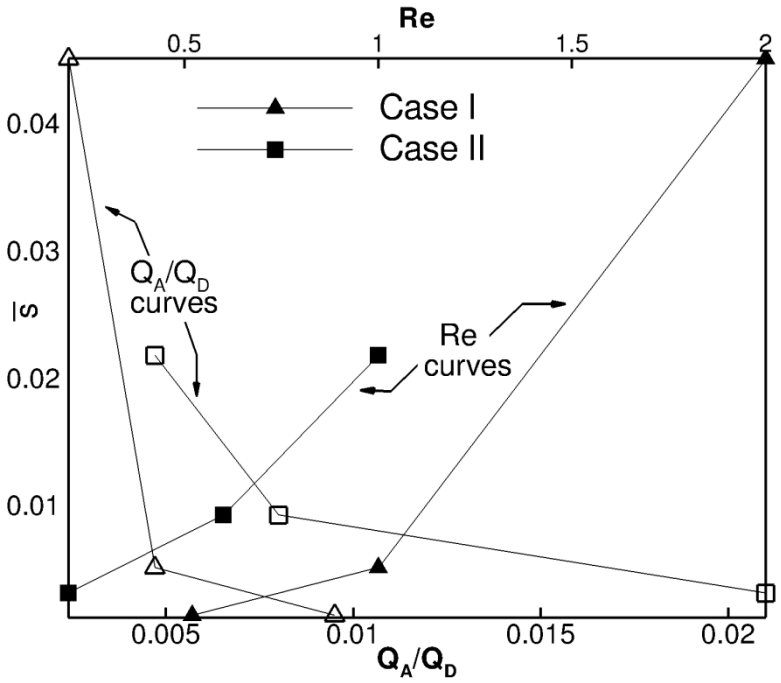

Figure 5.16 Effects of Q_A/Q_D and Re on kinematic mixing rate.

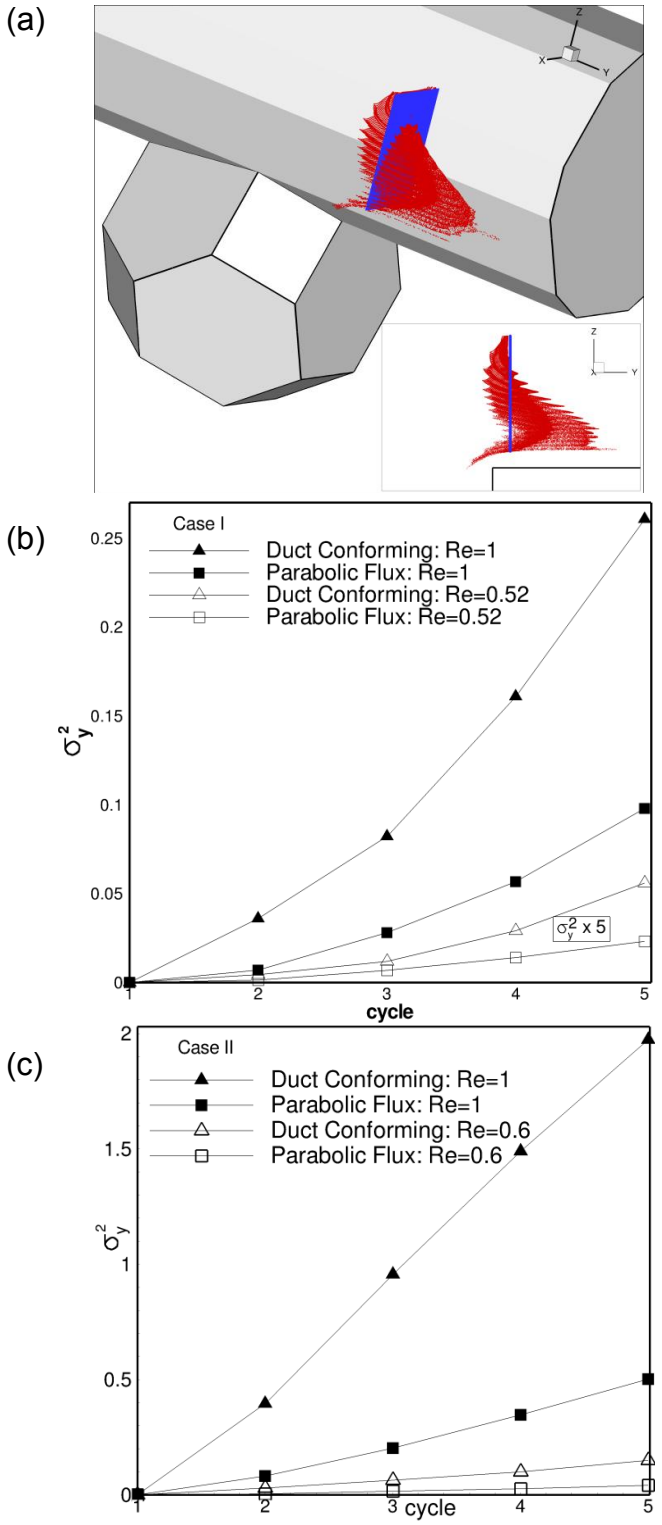

Figure 5.17 (a) Drift of an initial rectangular-plane dye (blue) in the duct for Case I, Re=1. The final shape of the dye after one cycle is in red. The insert shows the same when looking into the *x*-plane. (b) & (c) Axial variance vs. cycle number in Case I and Case II, respectively. The variances for Re=0.52 have been amplified by 5 times.

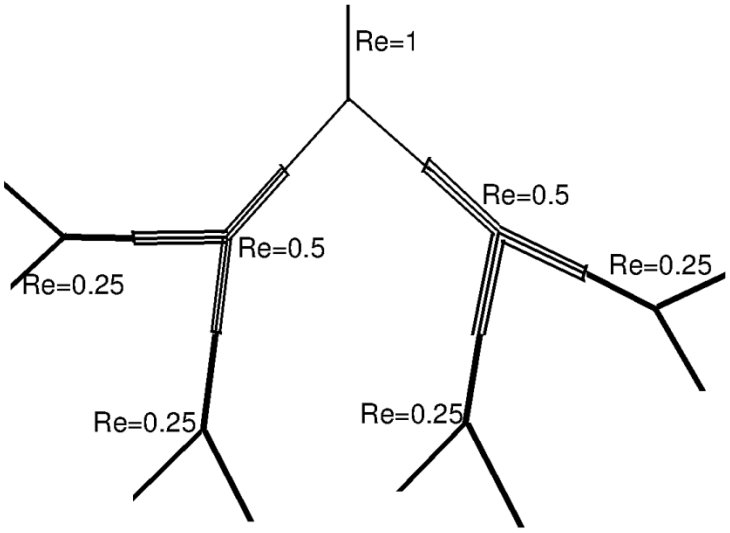

(a)

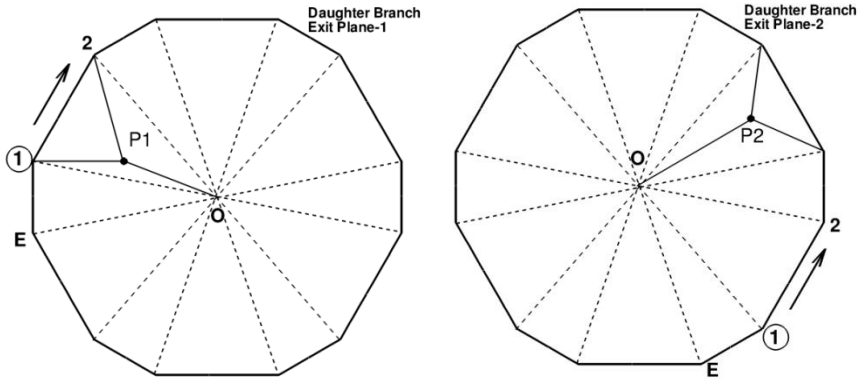

(b)

Figure 5.18 (a) Schematic of the tree structure used for advective mixing analysis. (b) Two exit planes in daughter branches of a given generation.

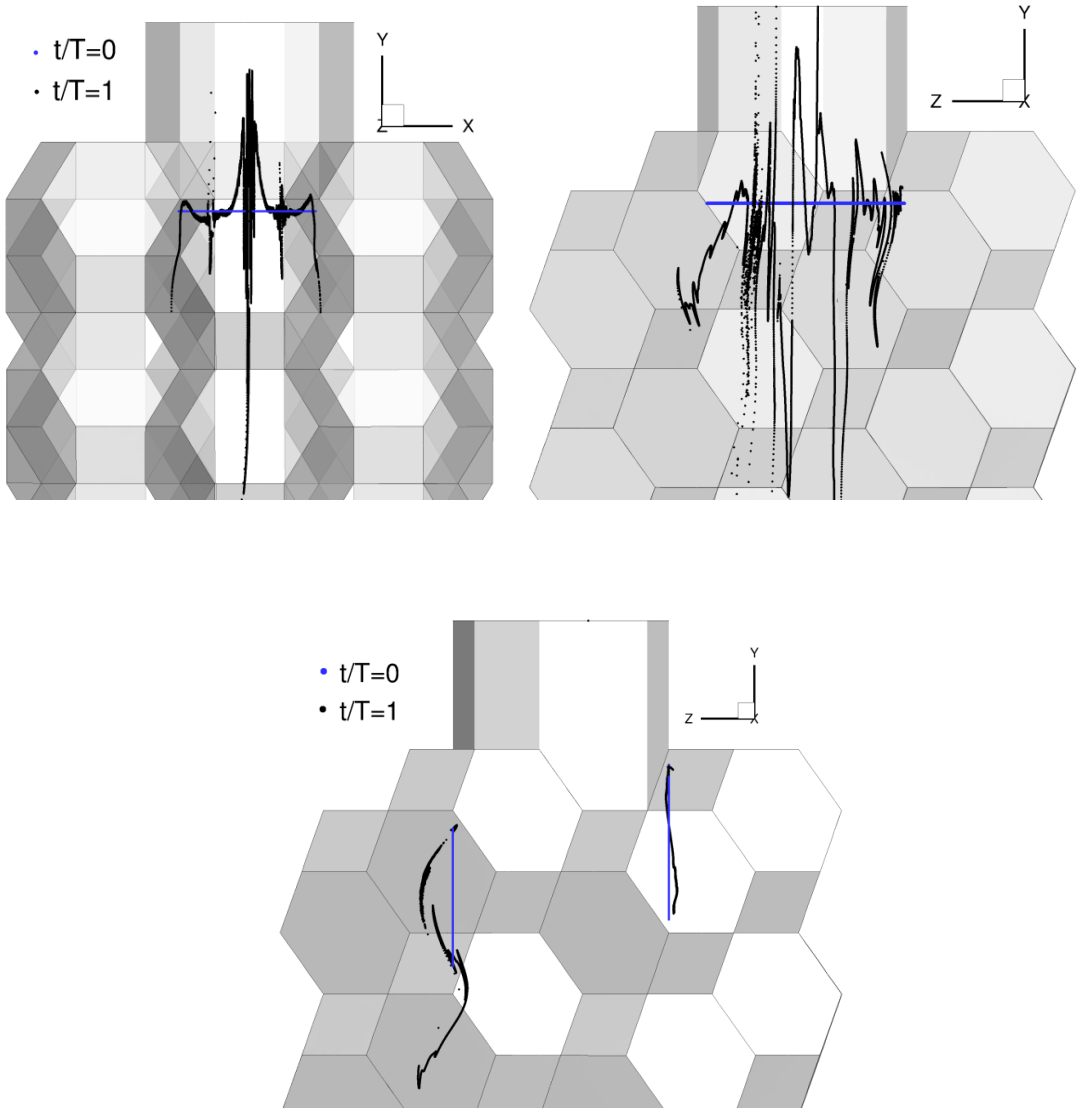

Figure 5.19 Advection of line dyes in the single bifurcation alveolar model.

CHAPTER 6

AEROSOL PARTICLE DEPOSITION

The main objective of this chapter is to compute particle deposition in idealized models of pulmonary acinus. Results of deposition efficiency for different regions of the acinus are presented. As before, geometries of Case I, Case II and Case III serve as models for respiratory bronchioles, alveolar ducts and alveolar sacs, respectively.

6.1 Introduction

A comprehensive knowledge of particle deposition mechanisms and estimates in acinar airways are essential. Particles in the range of 0.1-5 μm play an important role in various processes and are a part various occupational and environmental exposure (Tsuda et al., 1994). Also, understanding transport mechanisms of particles in this range may be useful as they serve as a diagnostic tool to estimate effective airway diameter (Tsuda et al., 1994). Timsina et al. (1994) estimated that only 10% of an inhaled drug delivered via a dry powder inhaler (DPI) reaches the alveoli. Newman et al. (1981) estimated that pressurized aerosols deliver only 8.8% of the dose to the lung, of which ~3% is deposited in the alveoli. Estimates of alveolar deposition based on ICRP (International Commission for Radiological Protection) formulae for CSP (Cigarette Smoke Particulate) typically of size 0.1-1 μm, significantly under-predict the alveolar deposition fraction (Gower and Hammond, 2007). Accurate estimation of particle deposition would help in improving drug delivery strategies for pharmaceutical aerosols.

Unlike mixing studies, the deposition of particles in the acinus has been computed using a plethora of models. The deposition estimates have been accompanied by one-dimensional, two-dimensional (Darquenne and Paiva, 1996; Darquenne and Prisk, 2003) and 3D (Harrington et al., 2006) models. Both moving wall and rigid wall models have been utilized (Haber et al., 2003; Sznitman et al. 2009; Darquenne et al. 2009; Chhabra and Prasad, 2010). There have also been some multi-generational deposition models which use either a simple geometry without bifurcation or a larger branching network to compute deposition efficiencies and determine hotspots of deposition (Darquenne, 2001, Darquenne, 2002; Darquenne and Prisk, 2003; Darquenne et al., 2009; Ma and Darquenne, 2011). Some of the experimental estimates of deposition include those of Darquenne and Prisk (2003). It is not possible to summarize all the works in the last two decades that has all contributed to improve our understanding of transport and deposition in the acinus. Here we describe conclusions of some studies relevant to our discussion that will highlight the current state of the art. Previous works have consistently made the following observations regarding deposition in the acinus.

Haber et al. (2003) identified that models of acinar flow that could be used to predict transport characteristics fall under two categories: *1*) the acinar ductal flow model that considers an alveolated duct and multiple alveoli surrounding the duct, and *2*) the single-alveolus model. The former model is suitable to study the duct-cavity interaction. The latter model is useful in studying the effect of the time-dependent flow field inside alveoli on the fate of aerosol particles within the alveoli. They considered approach '2' described above for their calculation by studying deposition inside a hemispherical

alveolus. The details of the flow structure inside the alveolus decide the residence time and ultimately, the deposition of particles.

One of the earliest studies of deposition in acinar models are those of Tsuda et al. (1994) who considered a 3D-axisymmetric acinar structure with rigid walls using only steady flow fields. The interaction between gravity and inertia were studied for larger sized particles. Deposition under varying flow rates and Stokes number were studied. Later analysis of flow and particle deposition using oscillatory flow fields in acinar models became commonplace. Kojic and Tsuda (2004) presented a very simple but elegant analytical treatment of flow and particle deposition in a long straight pipe. It was shown that the assumption of steady flow conditions to predict particle transport could significantly under-estimate local deposition density than computing deposition percentages from a more realistic oscillatory flow condition (such as tidal breathing condition). The significance of using a moving wall model over a fixed wall model has also been demonstrated in literature. For example, Haber et al. (2003) using a hemispherical alveolus model showed that the deposition could increase by as much as 100% for 0.5 μm particles in the presence of wall motion. More recently, Darquenne et al. (2009) also showed that the presence of wall motion significantly enhances deposition by using relative estimates with a stationary-wall model. Transport was computed using flow conditions that correspond to 18^{th} and 23^{rd} generation of the acinar tree. The geometry consists of annular rings around a duct with spatially periodic walls in the azimuthal direction defining each alveolus.

Deposition of micron sized particles predominantly depends on the parameters – gravity and flow structure. The flow Reynolds number in the acinus is of order unity or

less. The flow structures within a single alveolus across different generations of the acinar tree have been well understood (Tsuda et al., 1995; Haber et al., 2000; Henry et al., 2002; Kumar et al., 2009). As mentioned earlier, the two models that are appropriate to compute particle deposition are the isolated alveolus model (as in Haber et al., 2003) or the alveolar duct model that considers both the alveolar duct space and the surrounding alveoli.

Inspite of the advances in understanding alveolar transport, it has been recognized that the improved representation of acinus are important for better estimation of accurate estimates of deposition. Hence we utilize the accurate representation of honey-comb like representation of different regions of the acinus, introduced in Chapter 2 to predict particle deposition. The objectives of the work presented in this chapter are as follows.

a) First, we utilize the geometry of Case I to study the effect of time-dependent flow structure within the alveoli on deposition. To meet this objective, an initial particle flux is released at the entrance of an isolated alveolus. Its transport and the deposition percentages at the end of one complete cycle are computed.

b) Second, we utilize the Case I, Case II and Case III introduced in Chapter 2 to compute depositional efficiencies. To meet this objective, an initial bolus of particles is released in the entrance of the alveolar duct and its transport is computed for one complete cycle. Particles exiting the duct which may be available for distal acinar generations are not considered in the simulation. It may be recollected that Case I represents respiratory bronchioles which have occasional alveolar units. The model for Case II is an alveolar duct lined

completely with alveoli asymmetrically and represents the lung units in generation 18-22. Case III represent closed-end alveolar sacs. The current treatment uses a cluster of truncated octahedron to obtain a nearly space filling polyhedral.

6.2 Methodology

The particle tracking algorithm is a post-processing step which uses the 3D velocity fields generated using the techniques described in Chapter 2. The details of the flow structure in the alveolar cavity and alveolar duct were described in Chapter 4. Each particle's motion is individually computed. Brownian motion of the particles is not considered in this study. The equation of motion for spherical particles (Nowak et al., 2003; Maxey and Riley, 1983) reduces to

$$\frac{d\mathbf{u}_P}{dt} = F_D(\mathbf{u} - \mathbf{u}_p) + \mathbf{g} \tag{6.1}$$

where $\boldsymbol{u}_P$ is the particle velocity, $\boldsymbol{u}$ is the fluid velocity computed at the particle location, $\boldsymbol{g}$ is the gravitational acceleration. ρ_p is the particle density equal to 1000 kg/m^3 and is based on Finlay (2001) who asserts that for dry powder inhalers, particle density is typically ~ 1,000 kg/m^3 or greater. In addition, ρ is the fluid air density, which is equal to 1.2 kg/m^3. The above equation is reduced based on the assumption that the ratio of particle density to fluid density, $\rho_p/\rho >> 1$. The term $F_D(\boldsymbol{u}-\boldsymbol{u}_P)$ is the drag force per unit mass on the particle, where F_D is computed as

$$F_D = \frac{18\mu}{\rho_p d_p^2} \tag{6.2}$$

d_p is the particle diameter. F_D may be realized as the inverse of momentum relaxation time (Kojic and Tsuda, 2004). It has been shown that for smaller particles, the momentum relaxation time is much shorter than the characteristic timescale of the problem. In case of oscillatory flows, the time period is usually taken as the characteristic time scale. Hence, based on this assumption, the particle inertia term on the left hand side of equation (6.1) may be neglected (Kojic and Tsuda, 2004) and the equation of motion becomes

$$\frac{d\mathbf{x}_p}{dt} = \mathbf{u}_P = \mathbf{u} + \mathbf{g}/F_D = \mathbf{u}(\mathbf{x}_p) + \mathbf{g}/F_D \tag{6.3}$$

Henceforth, we use Eq. (6.3) in all our simulations. Here $\boldsymbol{x}_P$ is the location of particle. When gravity term is removed from the above equation, the equation of massless particles is retrieved. The term, $g/F_D=\rho_P g d_P^2/(18\mu)$ appearing on the right hand side of Eq. (6.3) is called the sedimentation velocity. The relative magnitudes of the velocity, $\mathbf{u}(\mathbf{x}_P)$ and sedimentation velocity, $\mathbf{U}_S$, determine the net transport of particles. Table 6.1 compares the magnitudes of sedimentation velocity and the maximum fluid velocity for various Reynolds numbers considered in this study. Table 6.1 also compares the sedimentation velocity with maximum flow speed observed in the alveolar cavity mouth. The values at the lowest Reynolds case considered are highlighted in this table. Both these velocities are computed at peak inspiration of the breathing cycle for Cases I, II and III described earlier. It is known that velocity in the alveolus is roughly an order of

magnitude smaller than those in the duct. The gravitational sedimentational velocity roughly increases as squared of particle diameter.

In all simulations, unless specified, the initial bolus consists of a disc of aerosol particles that conforms to the shape of the alveolar duct. Two types of concentration profiles have been used, namely, a uniform and a parabolic concentration. The concentration is modeled by assigning a concentration value to each particle in the inlet bolus. If a particle with concentration 'c' gets deposited on the wall, then 'c' particles are assumed to be deposited. For parabolic concentration, the distance from the center of the duct is used as a scaling factor. The concentration of a particle at the center of the duct is assumed to be 100 while the particles at the rim of the initial disk of bolus are assigned a concentration of unity.

Particle velocity was initialized to be equal to fluid velocity. The total simulation time of 2.5 s corresponds to a complete cycle. A total of 50 fluid volume data sets are used through one cycle. At each time step increment, the fluid velocity and the fluid mesh are interpolated between two of the fluid data sets, whose time window contains the current time, in order to obtain an instantaneous flow field for the particle transport. The interpolation method used a second-order approach that utilizes fluid velocity at each of the four node points of the tetrahedral element containing the particle. Deposition criteria for a particle are as described below. If the shortest distance from the center of mass of the particle to the airway wall is less than the particle radius, it is considered deposited. At the end of the expiratory phase, the coordinates of all the particles are stored for inspection.

The alveolar ducts and alveoli in different regions of the acinar tree may be treated as a collection of randomly oriented tubes. Under this assumption, an average estimate of deposition fraction could be obtained, once the deposition efficiency is estimated (as described above) at the end of one complete cycle. For a particle of given diameter d_P, let $DE(\theta)$ represent the deposition fraction corresponding to a gravity orientation θ. The angle theta defines the angle between the axis of the duct (which is the y-axis in our geometrical model) and gravity vector. With this notation, $\theta=0$ represents the case when the y-axis is normal to gravity vector. In the same way, $\theta=-90^o$ represent the cases where the gravity vector coincides with inspiratory flow direction in the duct. The fraction of aerosol depositing in an ensemble of randomly oriented non-alveolated ducts (Finlay, 2001 and Harrington et al, 2006) is given by

$$DE_R = \frac{1}{2}\int_{-90\deg}^{90\deg} DE(\theta)Cos(\theta)d\theta \tag{6.4}$$

Here DE_R is the deposition fraction for randomly chosen angle of gravity.

6.3 Validation

Before considering the results of alveolar deposition, the methodology and computational procedure is validated by computing particle transport in an oscillatory flow through a long straight pipe. The effect of gravitational deposition on the axial transport is considered. The simplicity of this problem also helps us understand the effect of sedimentation velocity and flow Reynolds number on the resulting deposition characteristics. An elaborate analytical treatment of this problem was carried out by Kojic and Tsuda (2004). To compare our results, a non-dimensional deposition parameter, P_d is

used. P_d is defined (as in Kojic and Tsuda, 2004) as ratio of characteristic sedimentation time and oscillatory flow period. The ratio of duct diameter and sedimentation velocity (D/U_S) is taken as the characteristic sedimentation time.

In the following validation cases, gravity vector is assumed to act normal to the axis of the pipe. The y-axis is taken as the main direction of oscillatory flow in the pipe. First we simulated oscillatory flow through a straight pipe for two Reynolds numbers, Re_D=0.9 and 0.45 defined using peak velocities of 2.66 cm/s and 1.33 cm/s respectively. The pipe diameter (D=2R) is taken as 540 μm. The data corresponding to generation 17 (Table 1 in Kojic and Tsuda, 2004) is considered for validation. Sedimentation time is computed for particle size d_p=1 and 2.5 μm. Other key parameter is the sedimentation velocity taken as U_s=0.0214 cm/s (for d_p=2.5 μm) and U_s=0.0034 cm/s (for d_p=1 μm). The computed particle trajectory and deposition parameter is shown in Figure 6.1. The initial location of the particle in both cases is at *x/R*=1.0, y=0 and z=0 where R is the radius of the pipe. In Figures 6.1 and 6.2, the axial location of the particle has been normalized with V_T/D^3, the ratio of stroke volume (V_T) to characteristic ductal volume (D^3). Here, a value of V_T/D^3 = 30.85 has been used. We direct the reader to Kojic and Tsuda (2004) for further details on this non-dimensional parameter. In Figures 6.1 and 6.2, the particle trajectory for Re=0.9 and Re=0.45 are plotted. The deposition parameter predicted from our simulation agrees well with the analytical value within an estimated error of ~0.2% for d_P=2.5 μm and ~0.4% for d_P=1 μm. As can be observed from Figures 6.1 and 6.2, the deposition time is roughly half the time-period for 2.5 μm particle. There is a significant increase in the sedimentation time observed for particle size of 1 μm. It takes more than 3 complete cycles for the particle to travel one full pipe diameter before

it gets deposited on the bottom wall. In both these cases, we chose the initial particle location to be located at x/R=1 because this corresponds to the maximum deposition time. All other particles initially located at any x/R<1 will have lesser sedimentation time. The predicted deposition parameter is independent of the Reynolds number. But the deposition location along the length of the tube is observed to be a function of the peak flow velocity.

6.4 Acinar Deposition Results

The rest of this chapter presents results of deposition for Cases I, II and III. Varying particle sizes and different orientations of gravity are considered. The following results correspond to the Case I (with Re= 1 and 0.52), Case II (with Re= 1 and 0.6 and 0.2) and Case III described earlier in Chapter 2. Particles sizes 0.5, 1, 2, 3 and 5 μm are simulated. The reader is referred to Chapter 2 and 4 for details of geometry and flow structure.

6.4.1 Deposition in an Isolated Alveolus

First, we utilize the geometry of Case I to study the effect of time-dependent flow structure within the alveoli on deposition. To meet this objective, an initial particle flux is released at the entrance of an isolated alveolus. Figure 6.3 shows an illustration of the initial particle release location at the beginning of inspiration. During the process of aerosol particle transport, some particles may be advected out of the domain. These advected particles are not considered any further in the simulation. At the end of one complete cycle, deposition percentages are computed and reported.

Figure 6.4 shows the final distribution of 1 μm and 3 μm particles. The particles advected out of the domain are denoted as 'A'. The particles that remain suspended at the end of expiration are denoted as 'S'. The deposited particles have been indicated as 'D'. The advected particles may be available for further penetration into distal alveoli and distal alveolar generations. During inspiration, the inspiratory flow is along negative y-axis. In the 1 μm particle case, roughly 80% of the total released particles advected out of the domain. Importantly, ~6% of particles remained suspended within the alveolus for further transport. The distal corner of the alveolar cavity is observed as a hotspot of deposition. Interestingly, almost all of 3 μm particles are deposited. The deposition location is split between the alveolar duct and within the alveolus. Roughly 60% of particles deposited in the alveolar duct and ~40% of particles deep within the alveolus.

Figure 6.5 shows the depositional efficiency for the various particle sizes considered in this study. The solid line corresponds to Re=1 case while the dashed line corresponds to Re=0.52 case. For both Reynolds numbers considered, all 3 μm and 5 μm particles are deposited. For the smaller sized particles (2 μm or less), the depositional efficiency is higher for Re=0.52 than Re=1 case. This can be expected as at lower flow speeds, the residence time of particles are increased. This can also be understood from Table 6.1 presented earlier. The last column of Table 6.1 reports the ratio of sedimentational velocity to alveolar flow speed. For example, in case of 0.5 μm particles, the ratio U_S/U_A at Re=0.5 is 0.005 and 0.0025 for Re=1.

6.4.2 Deposition in an Alveolar Duct Model

In this section, we present deposition estimates for the alveolar duct model for Case I, Case II and Case III. The alveolar duct model consists of alveolated duct and multiple alveoli surrounding the central lumen. In these simulations, an initial bolus of particles is released in the entrance of the alveolar duct and its transport is computed for one complete cycle. During the process of aerosol transport, some particles may be advected out of the domain through the two exits of the alveolar duct. These advected particles are not considered any further in the simulation.

For Case I, total of 31000 particles are initially released. It is ensured that any further increase in this number changes the computed depositional efficiency by less than 0.1 % and hence the result can be assumed as independent of the initial number of particles considered. Figure 6.6 shows the depositional efficiency for the various particle sizes considered in this study for Case I model. It may be recollected that Case I represents the geometry of respiratory bronchioles with isolated alveoli attached to a central duct. Here, the gravity vector is oriented along negative z-axis. This causes a preferential deposition onto the alveolus marked 'ALV' of Figure 6.6 for larger sized particles. The solid line corresponds to the Re=1 case while the dashed line corresponds to Re=0.52 case. Figure 6.6(a) shows the deposition for a uniform concentration of particles while Figure 6.6(b) shows the deposition characteristics for a parabolic concentration of particles. The definitions of these concentrations were described earlier in Section 6.2. It can be observed that parabolic concentration produced deposition efficiency which were systematically much lower than uniform concentration for particles of diameters less or equal to 2 μm. Again, as before, the Re=0.52 predicts higher

deposition than the Re=1 case for reasons described earlier in Section 6.3. The depositional efficiencies for 5 μm particles are roughly 60% for Re=1 and roughly 75% for Re=0.52 case. It is also observed that the depositional efficiency of 0.5 and 1 μm particles are very low indicating weak sedimentational deposition characteristics. Figure 6.7 presents results of deposition percentage for various gravity orientations. The angle 'θ' defines the angle between the axis of the duct (which is y-axis in our geometrical model) and gravity vector. For ease of representation, the complementary angle 'ϕ' is shown in the insert of Figure 6.7. For example, $\phi=180^{o}$ or $\theta=-90^{o}$ represent the cases when the gravity vector is opposite to inspiratory flow direction (marked as 'I' in Figure 6.7) in the duct. The variation of depositional efficiency follows a similar trend with the orientation 'θ' for all particle sizes. The curves in Figure 6.7 were computed only for particle sizes 2, 3 and 5 μm. The smaller size particles showed a weak variation with change in gravity orientation. The behavior of particles when $\theta=-90^{o}$ needs a special mention. When $\theta=-90^{o}$, the gravity vector acts opposite to the inspiratory flow direction in the duct: $\mathbf{g}=(0,1,0)$. During inspiratory phase, the ductal flow velocity increases. Due to expansion of the alveoli and duct, a fraction of the particles enter the alveoli. In the reverse expiration phase, the flow in the duct changes in direction. But these particles that have entered the alveoli are unable to exit the alveoli due to the predominant effect of the gravity acting to pull these particles toward the proximal wall where they are ultimately deposited. Figure 6.8 shows the final distribution of advected (marked as 'A') and deposited (marked as 'D') particles. Note the higher deposition region found within the alveoli on the proximal alveolar wall. With increasing particle size, the deposition occurs only on this proximal wall as in Figure 6.8(d) for the 5 μm particles.

Next, deposition in Case II geometry is considered. Unlike Case I, the two exits of the alveolar duct are not the same as the planes within which the particle computations are carried out. Figure 6.9 shows two planes 'I' and 'E' used in particle transport computation. It may be recollected that Case II geometry represents an alveolar duct model representing generations 19-22 of the acinar airways. In a real lung, roughly 25 % of the volume is occupied by alveolar lumen space while alveoli comprise roughly 75 % by volume (Haefeli-Bleuer and Weibel, 1988). Since the number of lung units increase exponentially down the acinar tree, a drastic reduction in the non-alveolated part of the ductal volume could be expected. Hence the particles that cross planes 'I' and 'E' are considered to have advected out of the domain and are available for penetration to distal acinar generation. If instead of exits 'I' and 'E', the entire length of the duct in Case II geometry in included in the particle transport simulation, roughly 5-10% higher deposition was predicted, particularly when the gravity vector acted perpendicular to the flow in the duct. In the following cases, a total of 49700 particles are considered. It is ensured that any further increase in this number changes the computed depositional efficiency by less than 0.1 % and hence the result can be assumed as independent of the initial number of particles considered. Figure 6.10 shows the depositional efficiency for the various particle sizes considered in this study. The gravity vector is oriented along negative z-axis. As before, the deposition characteristics for a uniform concentration and a parabolic concentration of particles are compared. For 2, 3 and 5 μm particles, deposition increases by roughly the same percentage with successive reduction in Reynolds number. For example, in case of a uniform concentration of 3 μm particles,

roughly 38% of particles are deposited in Re=1 case, ~48 % are deposited when Re=0.6 while ~60% of particles are deposited in case of Re=0.2.

Next, the deposition estimates for the alveolar duct model for Case III are presented in Figure 6.11. The deposition model and the initial release location of particles are also shown in Figure 6.11. The variation of deposition efficiency with particle size is shown for one particular gravity orientation. Case III corresponds to our alveolar sac model. In this case, the velocities existing are very small. The ratios of flow speed to sedimentational speed for Re=0.03 highlighted in Table 6.1. As can be noted from this table, for 2 μm or larger particles, this ratio is of the order of 1 or higher. Hence, gravitational sedimentation is the dominant mode of deposition.

6.4.3 Deposition for Randomized Gravity Orientation

The deposition efficiency computed for Cases I and II are used to arrive at an average estimate of deposition fraction using Eq. (6.4). The alveolar ducts and alveoli in different regions of the acinar tree are treated as a collection of randomly oriented tubes. The deposition efficiency computed using Eq. (6.4) is plotted as a function of a non-dimensional time computed as follows. The time a particle takes to travel one unit length divided by the time the fluid takes to settle one tube diameter is defined (Finlay, 2001) as

$$t' = \frac{2U_S}{U}\frac{L}{D} = \frac{\rho_P g d_P^2}{9\mu U}\frac{L}{D} \tag{6.5}$$

Here U_S is the particle sedimentational speed and U is the maximum flow speed for each of the cases depending on the Reynolds number as listed in Table 6.1. The total

model length, L for Cases I and II is obtained from Figure 2.2 in Chapter 2. D is the diameter of the alveolar duct. Most pharmaceutical aerosols are poly-disperse (Finlay, 2001) with a wide range of t' and hence the results of deposition percentage are expressed as a function of this non-dimensional time.

Table 6.1 Comparison of sedimentational speed with maximum flow speed for various particle diameters.

Particle Diameter (μm)	**Sedimentational velocity, U_S (cm/s)**		**Maximum Ductal Speed, U(cm/s)**	**Ratio, U_S/U**	**Maximum Alveolar Speed, U_A(cm/s)**	**Ratio, U_S/U_A**
0.5	0.000856	Re=1	3.2	0.00027	0.32	0.0027
		Re=0.5	1.6	0.0005	0.16	0.005
		Re=0.2	0.8	0.001	0.08	0.01
		Re=0.03	0.18	0.005	0.018	0.05
2.0	0.0137	Re=1	3.2	0.0043	0.32	0.043
		Re=0.5	1.6	0.0086	0.16	0.086
		Re=0.2	0.8	0.017	0.08	0.17
		Re=0.03	0.18	0.08	0.018	0.8
5.0	0.0856	Re=1	3.2	0.027	0.32	0.27
		Re=0.5	1.6	0.0535	0.16	0.5
		Re=0.2	0.8	0.11	0.08	1.1
		Re=0.03	0.18	0.5	0.018	5.0

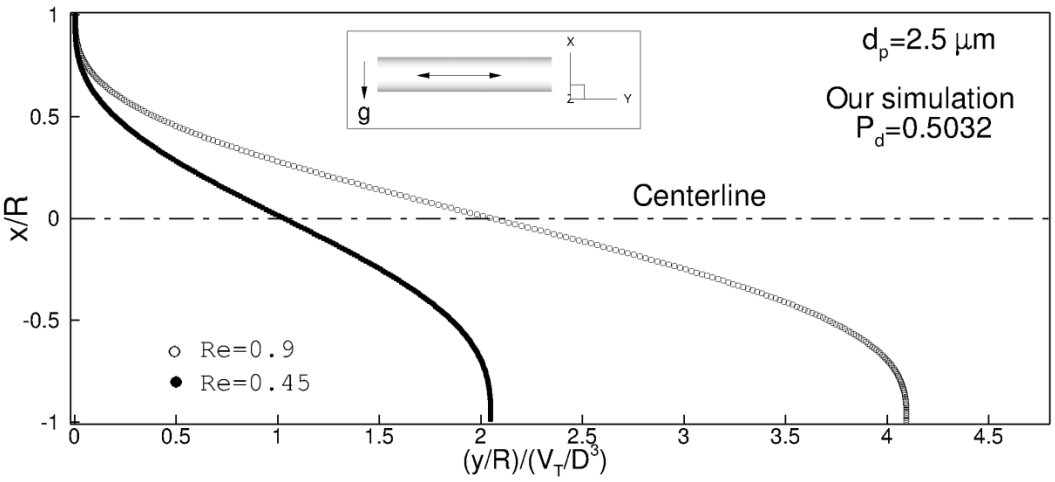

Figure 6.1 2.5 μm particle trajectory for oscillatory flow in a straight pipe. Gravity is perpendicular to flow direction.

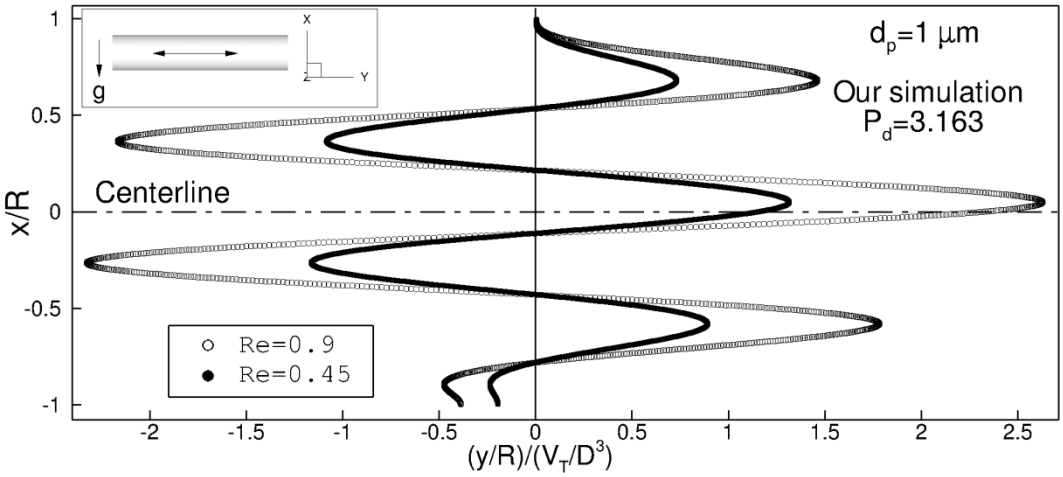

Figure 6.2 Validation: 1 μm particle trajectory for oscillatory flow in a straight pipe. Gravity is perpendicular to flow direction.

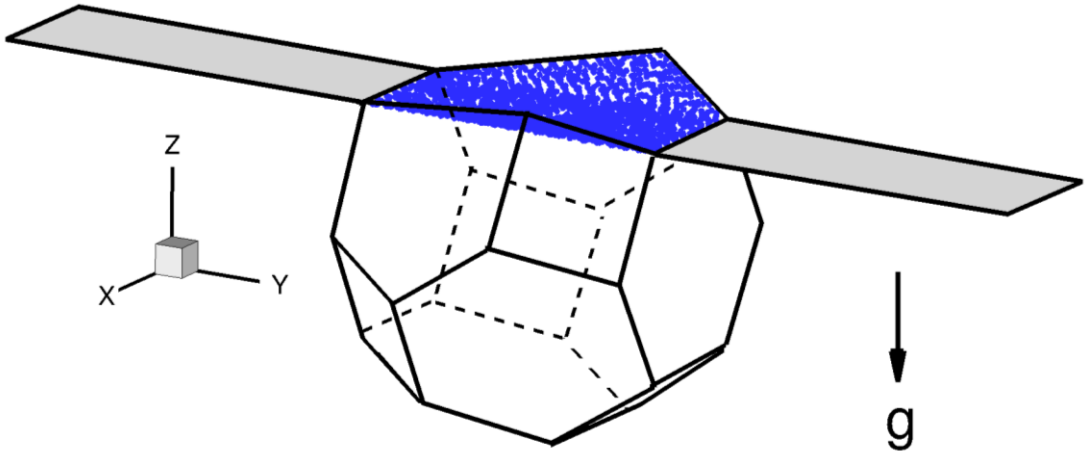

Initial release location of particles

Figure 6.3 Case I, Re=1, Moving wall case. Total of 11500 uniformly distributed particles were initially released as shown in blue.

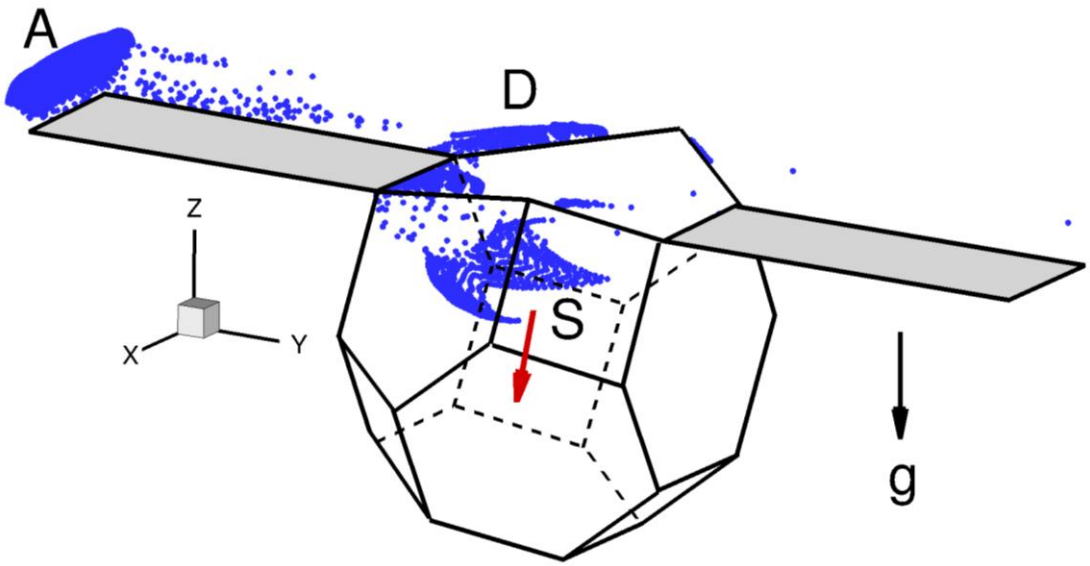

(a) 1μm particles

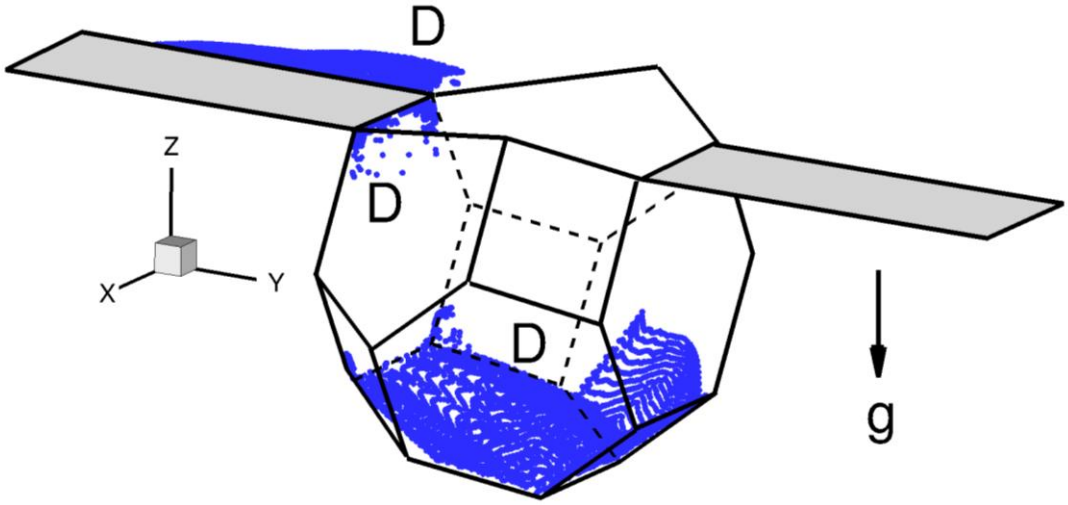

(b) 3μm particles

Figure 6.4 Case I, Re=1, Moving wall (a) Final distribution of 1μm particles after t/T=1 (b) Final distribution of 3 μm particles after t/T=1. The following notation has been used: D→Deposited particles; S→Suspended particles; A→Advected particles. The direction of gravity is also indicated. Almost all 3 μm particles are deposited within one cycle.

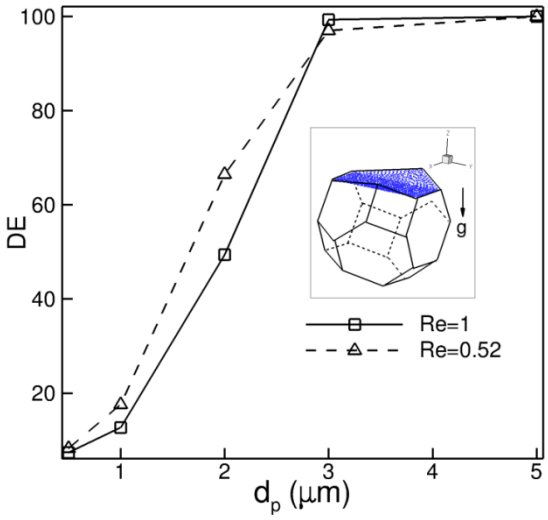

Figure 6.5 Deposition efficiency (DE%) for varying particles sizes. The initial release location at the entrance of the alveolus is shown in insert. The gravity is oriented perpendicular to the mean flow direction in the duct.

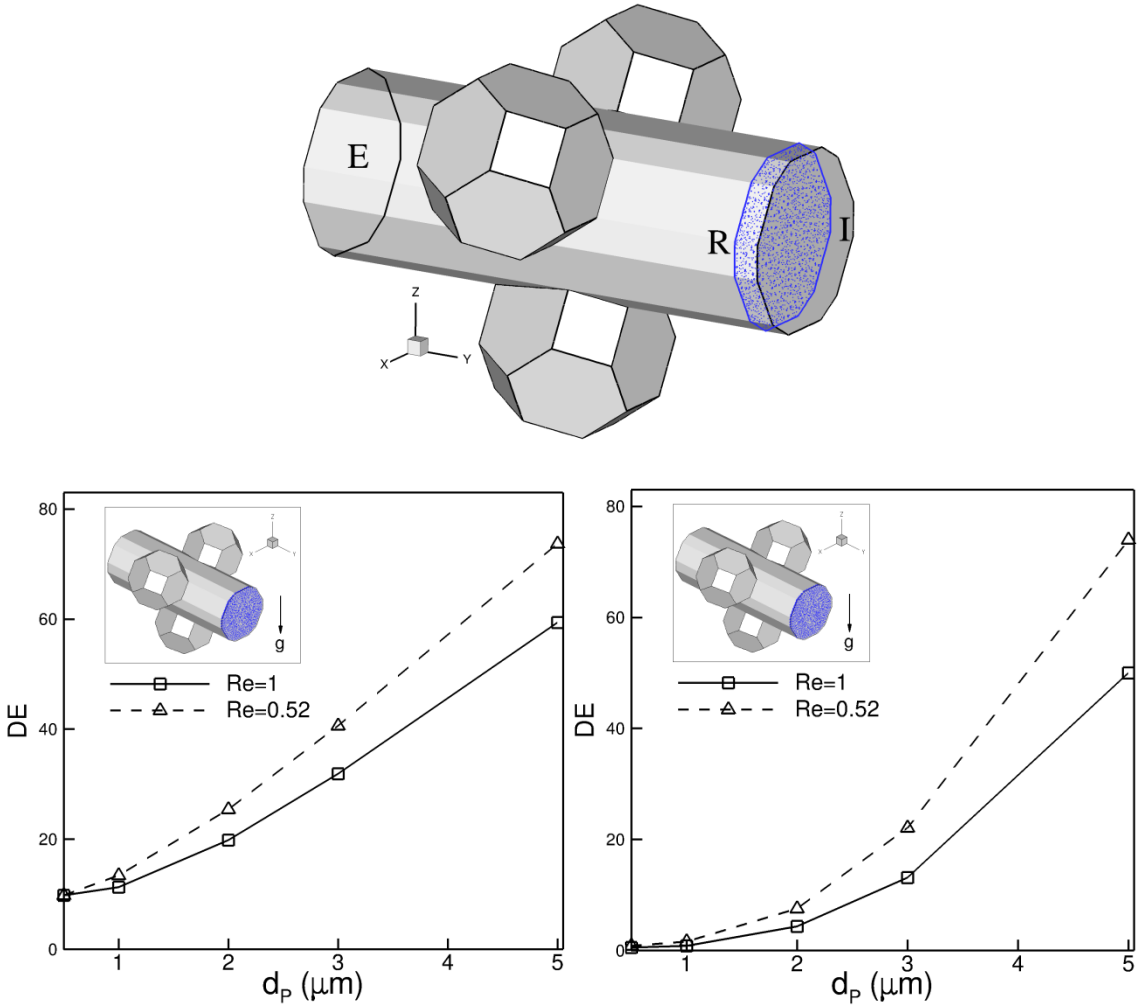

(b) Uniform concentration (c) Parabolic concentration

Figure 6.6 Deposition efficiency (%) for varying particles sizes for Case I. (a) The initial release location at the entrance of the duct is shown in insert in blue. The gravity is oriented perpendicular to the mean flow direction in the duct. (b) Uniform distribution of particles. (c) Parabolic distribution of particles.

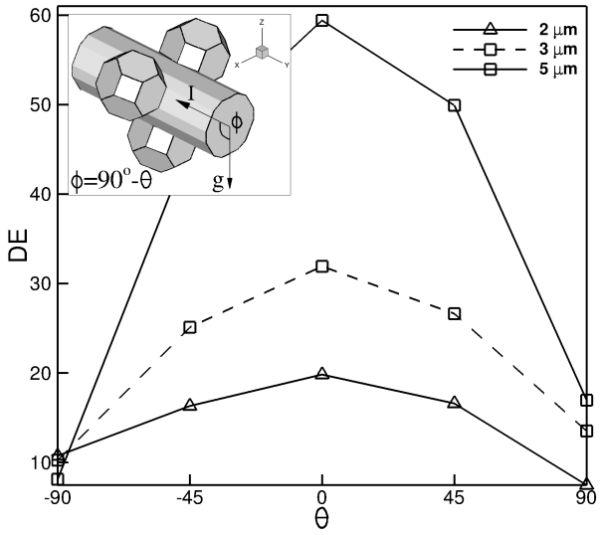

Figure 6.7 Case I: Deposition efficiency as a function of gravity for 3 particle sizes (a) Re=1, moving wall case with oscillatory flow in duct. The orientation 'θ' is defined with respect to inspiratory flow direction marked as 'I' in the insert.

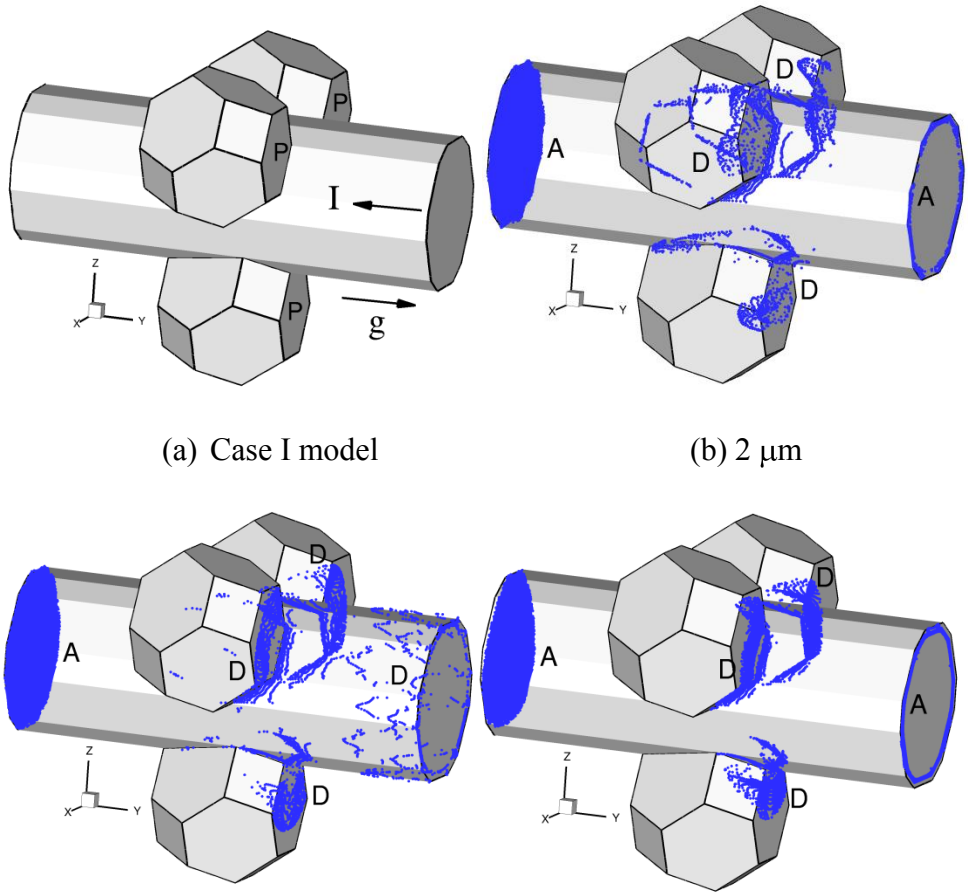

(a) Case I model (b) 2 μm

(c) 3 μm (d) 5 μm

Figure 6.8 Case I, Re=1, Moving wall for θ=90^o (a) Case I model showing gravity vector and inspiratory flow direction 'I'. The proximal is indicated as 'P'. (b) Final distribution of 2μm particles after t/T=1 (c) Final distribution of 3 μm particles after t/T=1. (d) Final distribution of 5 μm particles after t/T=1.The following notation has been used: D→Deposited particles; A→Advected particles. Gravity vector, **g**=(0,1,0) points along positive y-axis.

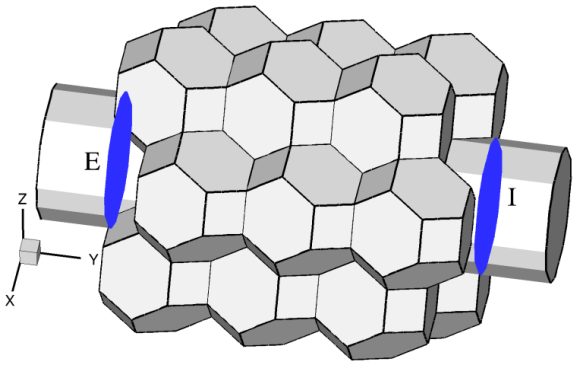

Figure 6.9 Depositional model for Case II geometry. Particles are considered as advected out when they cross exit planes marked ‘E’ and ‘I’. Particles advected out are not considered further in the simulation. The initial release plane for particles is just inside of plane marked ‘I’.

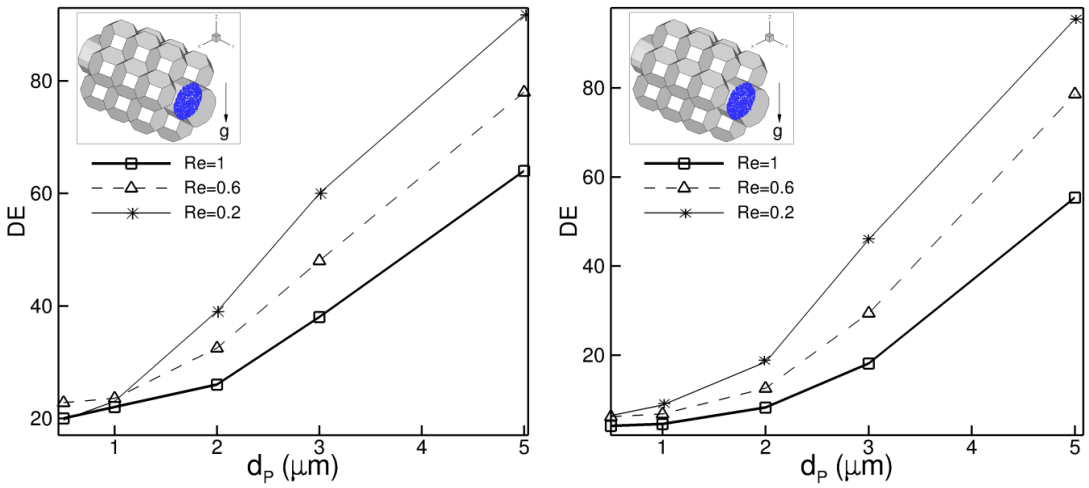

(a) Uniform concentration (b) Parabolic concentration

Figure 6.10 Deposition efficiency (%) for varying particles sizes in Case II. The initial release location plane of all particles near the entrance of the duct is shown in the insert in blue. Gravity is oriented perpendicular to the mean flow direction in the duct. Results for (a) uniform distribution of particles and (b) parabolic distribution of particles.

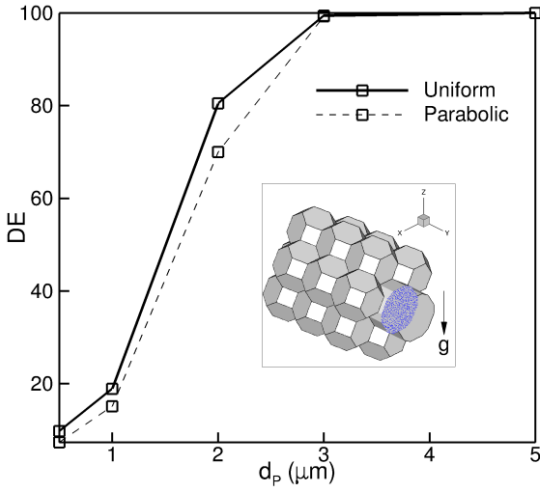

Figure 6.11 Deposition efficiency (%) for varying particles sizes in Case III. Gravity is oriented perpendicular to the mean flow direction in the duct. Results for (a) uniform distribution of particles and (b) parabolic distribution of particles.

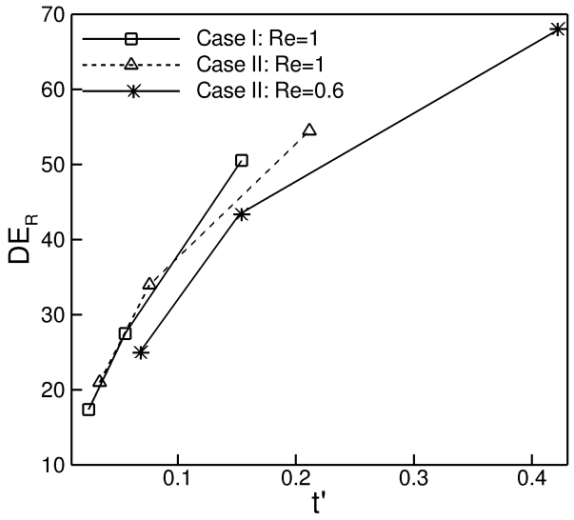

Figure 6.12 Average deposition computed using Eq. (6.4) with randomized gravity for Cases I and II.

CHAPTER 7

AIR FLOW AND TRANSPORT USING IMAGE-BASED MODELS

7.1 Introduction

Three-dimensional characterization of alveolar spaces and acinus in the mammalian lung are important for various purposes. The applications areas are numerous including accurate morphometry, better understanding of gas exchange and progression of diseases like emphysema, understanding alveolar mechanics and also providing a realistic representation for airflow and transport simulations. Since the acinus is a complicated 3D structure, 2D approaches have many limitations when it comes to understanding the true 3D geometry of the acinus and its tissue structure. In understanding alveolar mechanics, measurements from histology are limited in its ability to measure alveolar dimension and volume changes in the same lung tissue.

Efforts at 3D visualization and characterization of acinar spaces are limited and more recent (Watz et al., 2005; Litzlbauer et al., 2006; Tsuda et al., 2008; Parameshwaran et al., 2009) in literature. Apart from the problems associated with accessibility during imaging, the thin soft-tissue-like characteristics of the alveolar structure presents contrast issues during imaging and segmentation. A good review of the various imaging modalities and the usefulness of virtual bronchoscopy of various regions of the bronchial tree were presented by Mclennan et al. (2007). They also presented an image of digital micro-optical aided 3D virtual bronchoscopy of alveoli in human lung.

When analyzing transport of gases and particles in acinus, two important modeling aspects closely associated with the problem definition are the choice of

geometric representation of acinus and the alveolar wall motion. Conventional geometric representations of acini (alveolated ducts and alveolus) presented in literature and commonly used in CFD calculations are torus (Henry et al., 2002), spherical cavity (Sznitman et al., 2009), azimuthally divided cylinder (Harrington et al., 2006) or honeycomb like structure (Kumar et al., 2009). More complex representations have also considered (Sznitman et al., 2009) recently. The accuracy in estimating alveolar deposition has direct correlation with geometry.

Recently, micro-Computed Tomography (μCT) has been increasingly used to perform 3D imaging on mammalian lung acinus. Most of the efforts in literature have used fixation based on vascular perfusion or instillation before imaging the 3D structure of the acinus using tomography. In this work, air flow and particle transport analysis is carried out in a realistic model of a mammalian lung acinus. First, a 3D representation of the acinus is first obtained in a murine lung fixed using vascular perfusion at an inflation pressure of 20cmH_2O. Segmentation and isolation of a single (entire) acinus that branches out of a terminal bronchiole is carried out. The expansion of the acinus is prescribed and the air flow solution is computed. The main objective of this effort is to demonstrate the capability of utilizing high-fidelity image-based 3D models of acinus for transport calculations and hence motivate future works to consider realistic representations of acinus while studying alveolar mechanics and acinar flow.

7.2 Methodology

A C57Bl/6 mouse was chosen for this study that was part of a series of mice used in a larger study in our laboratories. Mouse handling, imaging and fixation protocol were

approved by the animal care facilities of the University of Iowa. The lungs were fixed in-situ by means of vascular perfusion at an inflation pressure of 20cmH_2O. Adjacently the lungs were extracted en bloc with the heart and dried while holding the same tracheal constant pressure. The lungs remained preserved and no significant shrinkage was determined. This fixation method preserves the lung tissue in the most natural state, where blood vessel and capillaries remain open. To image the alveolar structures of an acinus, very high resolutions are required. A multi resolution scanner that uses optical magnification (MicroXCT 400, XRadia, Concorde, CA) was used for imaging the fixed lung non-destructively in two steps. An initial whole lung scan was performed which was used to determine the coordinates of an acinus inside the apical lobe. The scanner uses different objective lenses to enable magnifications of 0.5, 2, 10 and 20x allowing zooming inside an object. The lowest magnification was used for the whole lung scan with a resolution of 12-28μm/voxel. At this resolution it is possible to see terminal bronchioles of the mouse lung and therefore have the ability to determine precise locations of individual acini. The 10x magnification provided both the necessary field of view (FOV) of 2×2×2mm as well as the required resolution of 2μm/voxel to allow visualization of the septal walls. A novel framework of multi-scale topo-morphologic opening approach allowed us to segment the acinus in high resolution images. Some initial manual seeding allowed the algorithm to decide which air spaces needed to be separated from each other (Saha et al., 2010). Once the acinus segmentation is obtained, it is converted into surface mesh with a Marching Cubes algorithm (Cline, 1987) and further smoothing the mesh using a without-shrinkage smoothing technique (Taubin, 1995).

7.3 Geometry and Problem Set-up for CFD

The acinus obtained from the methodology mentioned above is a complex geometrical structure. It has about 80 branch points. Figure 7.1 shows three views of this dense structure of alveoli. Figure 7.2 shows sections of the acinus. The region of the acinus above the shown plane has been blanked to aid in visualization. The entrance duct is not a part of the actual geometry and has been manually added to provide a boundary condition for the air flow simulation. The blue line indicates the boundary which was extrapolated to create the entrance duct. Some of the arrows are embedded in the figure to indicate the possible airflow direction. The red boundary shown in Figure 7.2(a) is the region of carina between two branches as also shown in Figure 7.2(b). It may be speculated that this is hot spot of particle deposition.

The acinus obtained from the high field of view scan has a surface area 6.9 mm^2 and occupying volume of 0.145 mm^3 giving a Surface area-to-Volume (S/V) of 47.5 mm^{-1}. It has a single entrance for air flow into the entire volume. The entrance to acinus in the mouse lung is about 160 μm. For our CFD analysis, the mouse acinus model has been scaled to human acinus dimensions. This has been scaled to obtain an entrance diameter (hydraulic diameter based on surface area) to acinus of about 500 μm giving S/V of 15 mm^{-1}. This value is close to the ratio by Woods et al. (2006) who observed a S/V of 20 mm^{-1} for human lung acinus. The surface mesh obtained from the surface smoothing step is exported in STL format. Volume mesh is created in GAMBIT©. The volume mesh has about 13.5 million tetrahedral elements and about 2.59 million nodes.

The acinus geometry provides a single entrance through which air ventilates the entire volume of acinus. Hence the observed flow rate at the entrance is the result of volumetric expansion of the acinus. The boundary conditions imposed for the CFD model are shown in Figure 7.3(a). A uniform sinusoidal expansion of the wall motion is prescribed in all three directions. The mouth of the acinus is assumed to expand only radially and does not move in the z-direction. All other surfaces of the acinus have non-zero boundary velocity. This prescribed wall motion results in a volume expansion (difference in volume of acinus between end of inspiration and beginning of inspiration normalized by the volume at beginning of inspiration) of 29.5%. The resulting Reynolds number based on the peak velocity computed at peak inspiration of t/T=0.25 and the hydraulic diameter of the attached duct (measured also at peak inspiration) is 0.5. The flow rate from such a volume expansion results in a flow Reynolds number (based on velocity at peak inspiration of t/T=0.25) of 0.54.

7.4 Results

7.4.1 Air Flow

Figure 7.3(b) shows a snapshot of the streamlines in the flow at t/T=0.25. The complicated structure of the acinus makes plotting and interpretations of the flow pattern difficult. In Figure 7.3(b), care was taken to plot the streamlines in most of the alveoli. After very careful and thorough consideration, it was concluded that none of the alveoli contains a recirculatory flow and the resulting flow pattern is similar to the streamline pattern that was observed in Figure 4.5 of Case III. Note that the geometry being studied is a very large acinar structure and hence it is easier to introduce higher Reynolds number

flow (unlike Case III) and hence look for the presence of recirculatory flow and also study the low-Reynolds number inertial effects of the flow. It is already established from the mathematical models in Chapter 4 that at low-Re (for Q_A/Q_D not too small), the flow within the alveolus does not separate. Currently, it is not possible to compute the Q_A/Q_D ratio of any chosen alveolus due to the complexity of the acinar geometry.

7.4.2 Mixing

Once the flow is computed, advection of massless particles and the resulting Lagrangian drift is computed. A line tracer is advected for one full cycle. The dye is released far away from the entrance of the alveolar mouth as shown in Figure 7.4. Figure 7.4 shows the advection of two line dyes. The two line dyes are released in yz-plane and xz-plane respectively. The resulting shape of the dye due to advection at t/T=0, 0.5 and 1.0 are plotted. Note that the dye forms like folding structures similar to those observed for Case I and Case II when the dye was released in the duct. This observation supports and in-line with the observations made in Chapter 5. To recall, streaming was identified as a key mechanism of dispersion and mixing in low-Re oscillatory flows. It was also demonstrated in that chapter that this streaming is a result of non-zero inertial and geometrical effects and explains transport of massless particles in low-Re high-K_C acinar flows. It was also demonstrated that the presence of recirculation (for both rigid-wall, moving wall cases and also for deep and shallow cavity) does not have any direct influence on the observed drift of the dye. The observations from Figure 7.4 are in agreement with the above discussion again confirming the fact that streaming resulting from interaction of non-zero inertial flow with acinar geometry results in folded

advection pattern. Here advection has been demonstrated for one complete breathing cycle. It may be noted from Figure 7.4 that some particles have exited the domain on the reverse flow (expiration phase). Currently, these particles have been considered lost in the results of Figure 7.4. In future, improvements on the model could be made to remove this limiting situation thus enabling analysis for multiple breathing periods.

7.4.3 Aerosol Deposition

As before, transport and deposition analysis is carried out. Aerosol particles are released at the entrance of the duct as shown in Figure 7.5. Different particle sizes and gravity orientations have been considered. Particles (aerosols) are transported into the acinus and get deposited. On the return phase during expiration, some particles may advect out of the domain and are assumed lost from the simulation. The transport calculation is carried out for one complete breathing cycle. The deposition percentage and the spatial distribution of aerosol particles at the end of one full cycle are reported in Figure 7.5 and Figure 7.6. The spatial distribution of particles seems to be dependent on the gravity orientation although for all gravity directions, the deposition percentage increases with particle diameter. As before, both parabolic and uniform particle distributions are considered. The reader is referred to Section 6.2 for details. 2 μm particle seems to be most affected (and hence most sensitive to) by changes in gravity orientation. Parabolic and uniform distributions give almost similar depositional characteristics. The deposition behavior seems to be largely dominated by sedimentation as can be observed from the fact the larger diameter particles (3 and 5 μm) show very high depositional rates immaterial of the gravity orientation. Similarly, the small particles

(0.5 and 1 μm) seem to be least affected by gravity direction and show almost same deposition percentages. Previously in Section 6.4, it was observed that when the gravity vector acts opposite to the inspiratory flow direction in the duct, significant deposition was observed near the proximal wall. During inspiratory phase as the ductal flow velocity increases, the expansion of the alveoli and duct causes a fraction of the particles to enter the alveoli. In the expiration phase, the flow direction reverses. But these particles that have entered the alveoli are unable to exit the alveoli due to the predominant effect of the gravity. Similar effect can be observed in Figure 7.5(c) and (d) as the most of the particle deposition is near the proximal regions and top walls of the alveoli.

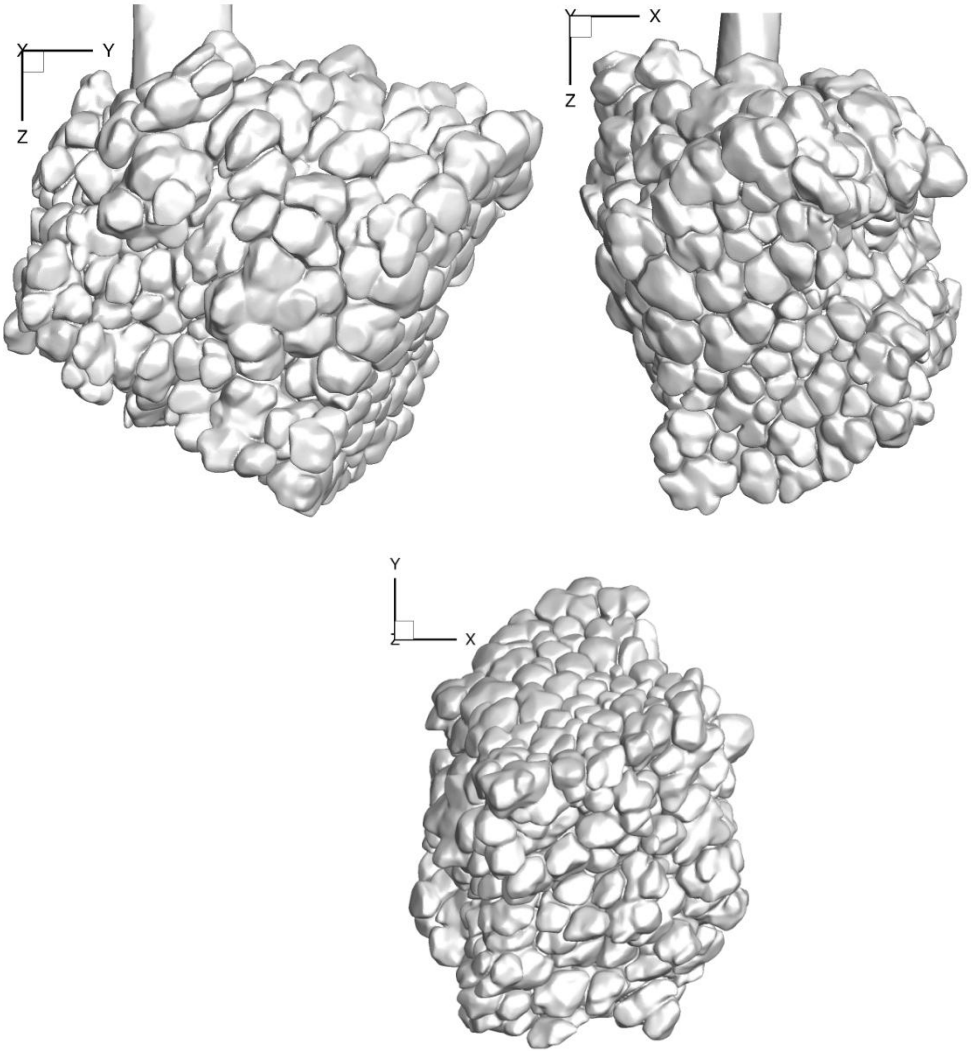

Figure 7.1 Three views of the reconstructed acinus from μCT high-resolution scans.

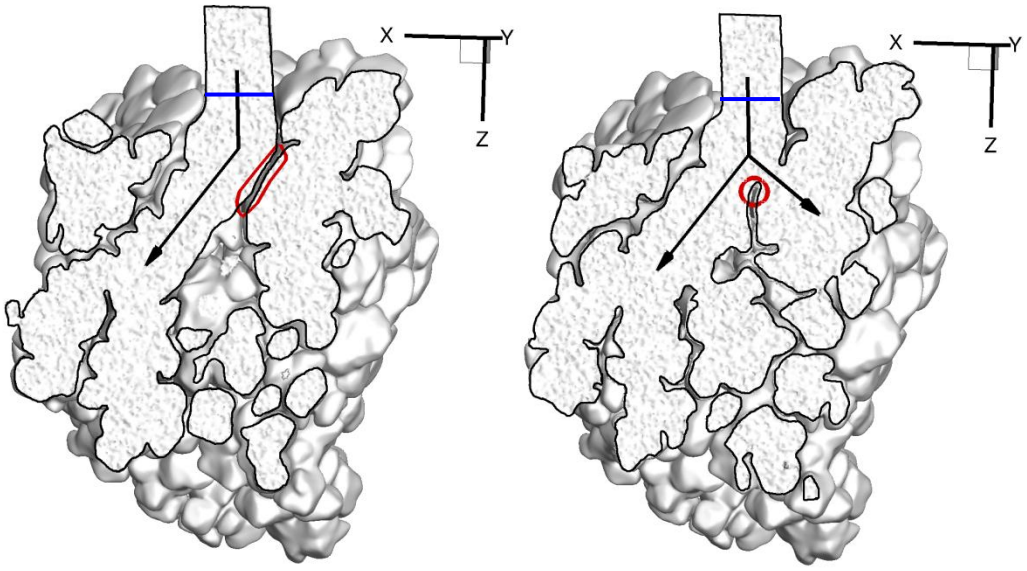

Figure 7.2 A section of the acinar model sliced at two locations. The portion of the acinus upto this slice location is blanked to aid in visualization.

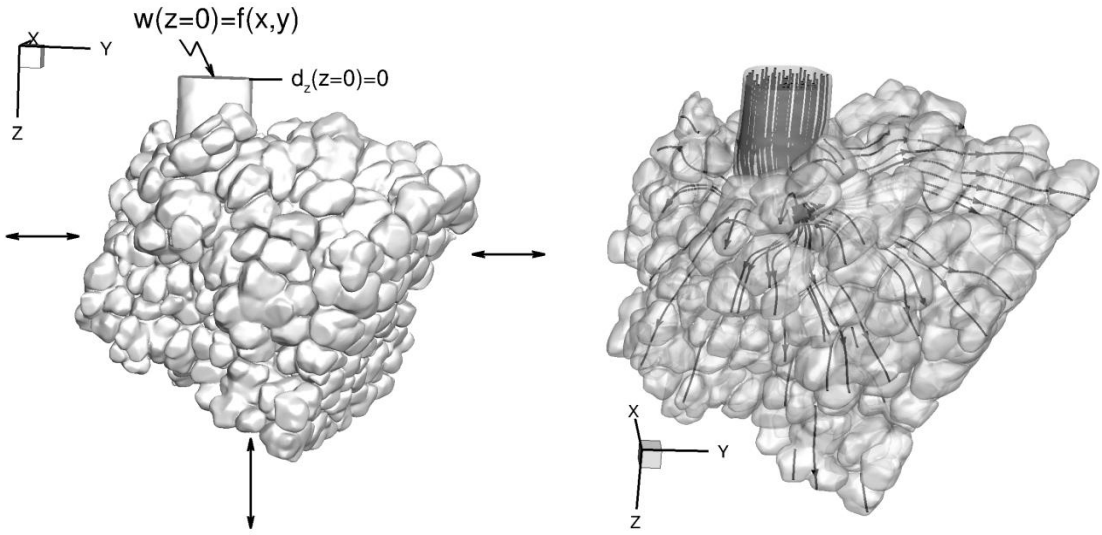

(a) (b)

Figure 7.3 (a) CFD model of acinus. Arrows indicate direction of expansion. The boundary condition at entrance is also shown. (b) Snapshot of instantaneous streamlines at t/T=0.25.

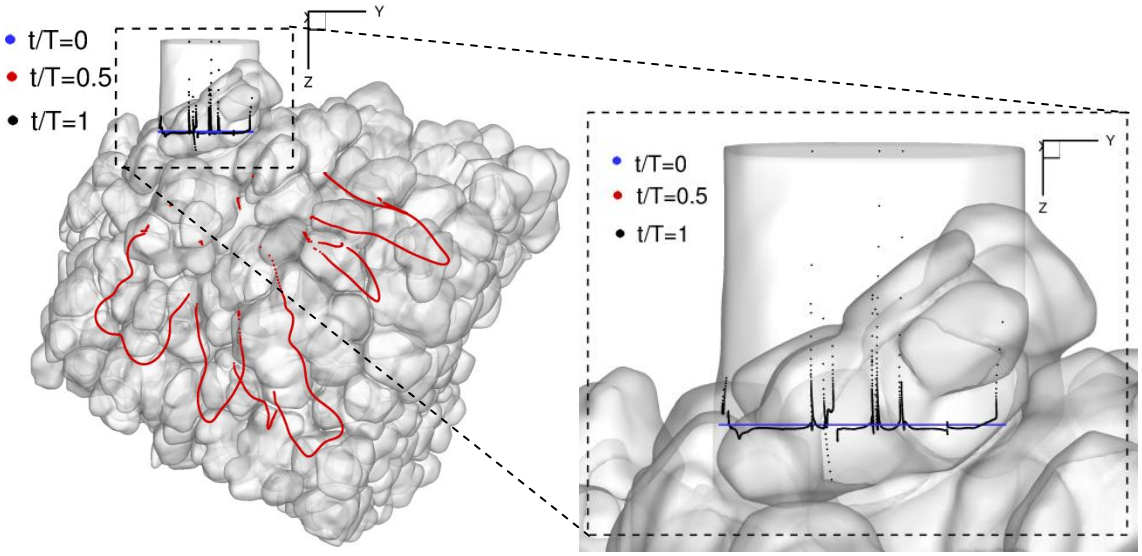

(a)

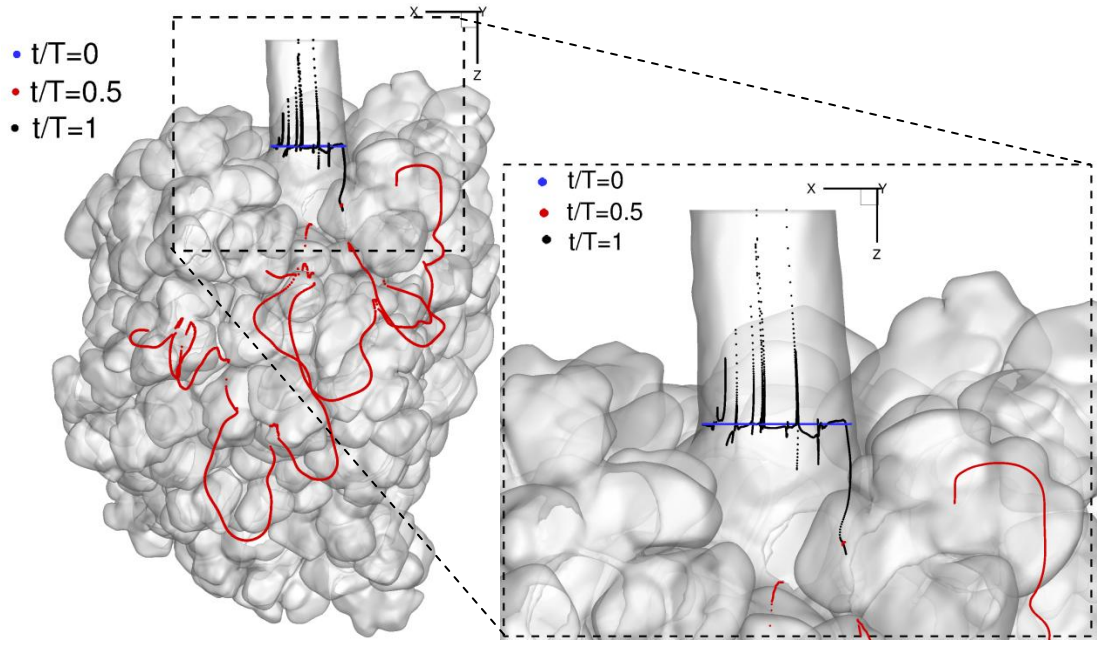

(b)

Figure 7.4 Results of advection of a line dye for one cycle. (a) Results of advection of a line dye released in yz-plane. Zoomed-in view is shown on right. (b) Results of advection of a line dye released in xz-plane. Zoomed-in view is shown on right.

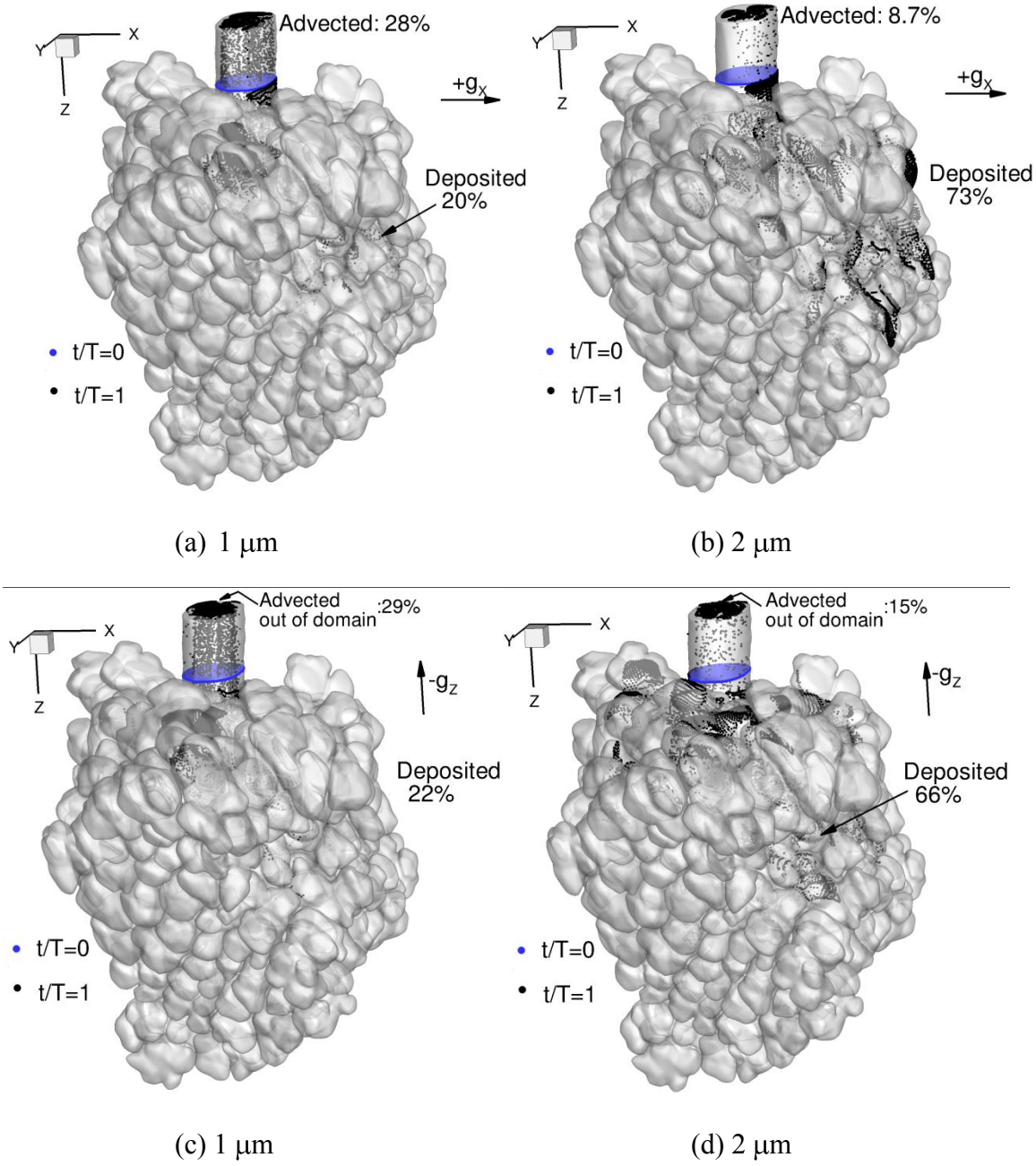

(a) 1 μm (b) 2 μm

(c) 1 μm (d) 2 μm

Figure 7.5 Aerosol deposition results (a), (c) The final particle distribution after one complete cycle for 1 μm particle. (b), (d) The final particle distribution after one complete cycle for 2 μm particle.

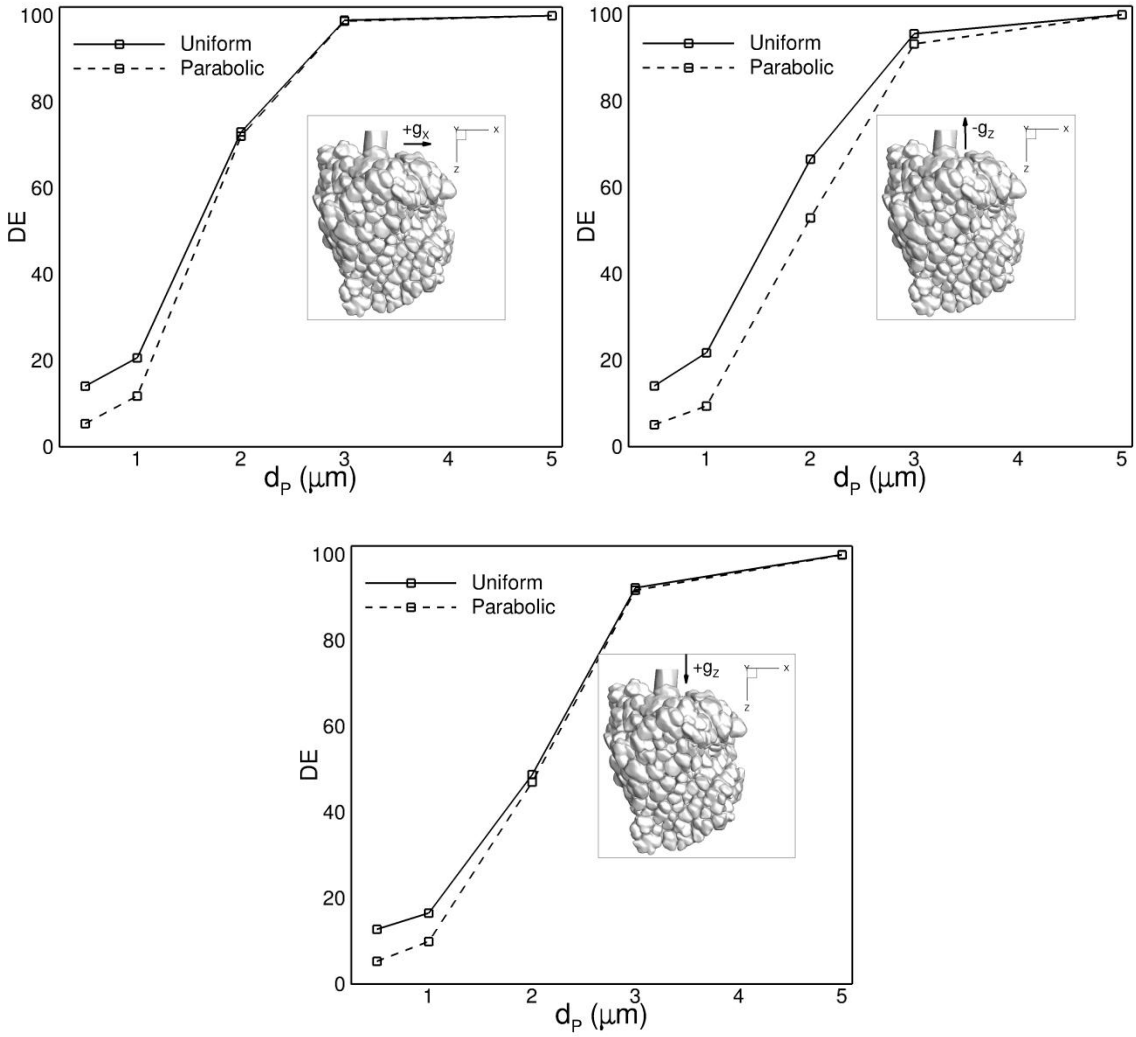

Figure 7.6 Aerosol deposition results (a-c) Deposition efficiency (DE in %) for three gravity orientations.

CHAPTER 8

SUMMARY AND RECOMMENDATIONS FOR FUTURE WORK

8.1 Summary

Understanding flow and transport phenomena in the pulmonary acinus are important for predicting particle deposition and hence, in designing effective drug delivery strategies for the lung.

In the first part of this study, two-dimensional open cavity geometry and three-dimensional honeycomb-like model involving a central airspace and surrounding alveoli are used as models to study alveolar flow. In the 2D case, the wall is assumed rigid and the flow structure consists of a dominant recirculation. In the 3D case, numerical results predict that flow in the presence of wall motion is characterized by the presence of a developing recirculation region within the cavity and by flow entrainment region indicative of the weak nature of interaction between duct and cavity. Under normal breathing condition (2.5 seconds) and volumetric expansion (~25%) considered here, recirculation is observed to disappear for $Re<0.6$. Alveolar flow in higher generations (at lower Reynolds number) results from significantly higher entrainment of the ductal flow and does not exhibit any dominant recirculation within the cavity. In an asymmetric arrangement of the alveolar cluster, topological differences in cavity result in significant differences in the size of recirculation and the size of entrainment region within the same acinar generation, indicative of a non-uniform alveolar ventilation. The flow in the terminal alveolar sac is non-recirculating and not affected by geometrical asymmetries.

In the second part of this study, the flow field is utilized to study advective mixing in low-Reynolds number acinar flows. Acinar flows belong to a unique category of low-Re high-K_C oscillatory flows. Study of mixing is important in understanding transport of sub-micron sized particles in the acinar region of the lung. The objective of the study is to observe and possibly explain the mechanism of dispersion and mixing of small aerosol-like particles in the acinus. Mixing is studied by tracking diffusion-less massless particles in an unsteady flow. In simple terms, we seek to explain and estimate the extent of deviation of a particle location at the end of a breathing cycle, from its initial location at the beginning of the breathing cycle. This deviation is termed as Lagrangian drift. The origin of Lagrangian drift can be explained by the steady-streaming phenomenon, a terminology commonly known in the fluid dynamic community. This non-zero Lagrangian drift in the acinus results from interaction of the oscillatory ductal flow with alveolated geometry. The phenomenon of steady streaming is found to hold the key to the origin of kinematic mixing in the alveolus, the alveolar mouth and the alveolated duct. This mechanism provides the route to explain folding of material lines and surfaces in any region of the acinar flow, and has no bearing on whether the geometry is expanding and contracting or if flow separates within the cavity. In other words, the presence of volumetric expansion of the alveolus is not the determinant of observed advection pattern. Similarly, the presence of recirculatory flow pattern within the alveolus is not the determinant of the observed advection pattern. Based on flow conditions and resultant convective mixing measures, we conclude that significant convective mixing in the duct and within an alveolus could originate only in the first few generations of the acinar tree as a result of non-zero inertia, flow asymmetry and large K_C number.

In the third part of the study, aerosol deposition analysis is performed. Particles are released in various regions of the flow and advected for one complete breathing cycle. Five different diameters of particles, 0.5 μm, 1 μm, 2 μm, 3 μm and 5 μm are considered. Different gravity orientations with respect to the inspiration flow direction are also considered.

In the fourth part of this study, the envelope of flow and transport studies in acinus is expanded by utilizing image-based models of acinus. Consistent with observations from idealized (2D and 3D) models, kinematic mixing studies indicated a fold-like advection pattern of line dyes, non-zero Lagrangian drift and hence established the existence of non-negligible dispersion deep in the lung acinus. Unlike the idealized models, visualization of the flow, mixing and deposition becomes a very big challenge due to the complexity of the acinar geometry. Nonetheless, the results in Chapter 7 are expected to motivate future work in utilizing more realistic representations of acinus.

8.2 Specific Contributions of This Work

Some of the highlights of this work are as follows. Early acinar flow and transport studies utilized simple 2D or 3D toroidal or spherical open cavity models of pulmonary acinus. More recently, Sznitman et al., 2009 used a complex multi-generational model of acinus using honeycomb-like model of acinus and estimated particle deposition. The present study utilized a wide range of model representations of acinus with complexities ranging from simple 2D open cavity to complicated asymmetrical honeycomb-like structure (with and without branching) and further expanded the envelope of these studies by using an image-based acinar model.

Mixing is a commonly studied topic in idealized acinar models (See chapter 5 and thereon). In these experiments, advection of massless particles is assumed to model the transport of small particles across the inhaled air-residual air interface in the lung. Many studies looked for mechanisms of irreversible transfer of particles across this interface. Significant contributions from Tsuda et al. (1995), Henry et al. (2002) and others revealed important dispersive behavior in the acinus. The dye was shown to experience very large folded pattern after one or multiple cycles resulting in dispersion that increased more than linearly with number of breathing cycles. It was shown that the presence of alveolar wall motion and saddle points associated with the recirculatory flow in an alveolus played significant contributions. In this work, elaborate mixing analysis was carried out in a wide range of acinar models. The concepts of streaming, drawn from fluid-dynamics are used to explain observed large drift of the dye during advection. The observed dispersion of dye is shown to arise due to interaction of oscillatory flow in an alveolated geometry at non-zero Reynolds numbers. Interestingly, it was also observed that the presence of such advective mixing behavior exists immaterial of whether the alveoli expand or not. Also, it was observed that the presence or absence of recirculatory flow inside the alveoli does not solely determine the presence of observed Lagrangian drift of the dye.

8.3 Recommendations for Future Work

Although the present work revealed important and fundamental mechanisms towards better understanding of acinar transport, various modeling assumptions were used. These assumptions become a limitation and are worth mentioning here. The

assumption on alveolar wall motion is one of the main limiting assumptions in this study. The specific details on volumetric expansion of alveolar duct and alveoli in response to lung volume change during breathing remains largely unknown. Several modes of expansion like recruitment, balloon-like isotropic expansion and paper-bag like crumbling have been proposed. Different theories also exist on whether alveoli actually expand or much of the volume change is due to expansion of alveolar duct region. It is not within the scope of this work to answer such questions. It is hoped that the discussion of these limitations will motivate future work in removing these assumptions.

Various physiologically-relevant and non-physiological future studies could follow from the results presented in this thesis. The current work could be expanded in the following directions.

- The present work utilized a symmetric wall motion where the wall motion in the inspiration and expiration follows identical paths. This assumption could be relieved and a slight asynchrony could be introduced between the alveolar and ductal flows.
- The present work assumes equal time intervals of inspiration and expiration (i.e) inspiration time interval is exactly equal to expiration time interval. In tidal breathing, the expiration time interval is slightly longer (Finlay, 2001) than the inspiration time. Understanding the effect of such a change on mixing and deposition characteristics may have important implications for drug delivery.
- Streaming is a fundamentally a fluid dynamic phenomenon and was identified as a key mechanism to explain observed mixing and dispersion in acinar flows. In particular, the observed mixing is due to the presence of high K_C number which

results in the observed transport characteristics. Although not directly related to acinar mixing, it will be useful to understand effect of the following parameters on mixing: the ratio of depth of cavity versus depth (or diameter) of duct and the aspect ratio of cavity.

- Another important aspect of importance is the effect of breathing frequency. Only one breathing period has been considered in this study. It would be very valuable to consider a wide range of breathing periods and hence varying Keulegan-Carpenter number.

BIBLIOGRAPHY

Allievi, A., and Bermejo, R. 1997. "A Generalized Particle Search-Locate Algorithm for Arbitrary Grids." *Journal of Computational Physics* 132:157-166.

Anderson, P.D., Galaktionov, O.S., Peters, G.W.M., Van De Vosse, F.N., and Meijer, H.E.H. 1999. "Analysis of mixing in three-dimensional time-periodic cavity flows." *Journal of Fluid Mechanics* 386, 149-166.

Aref, H. 1984 "Stirring by chaotic advection", *Journal of Fluid Mechanics* 143:1-21.

Burrowes, K.S. 2005. "An anatomically-based mathematical model of the human pulmonary circulation." PhD. Thesis, The University of Auckland.

Butler, J.P., and Tsuda, A. 1997. "Effect of convective stretching and folding on aerosol mixing deep in the lung, assessed by approximate entropy." *Journal of Applied Physiology* 83:800–809.

Carney, D., DiRocco, J., and Nieman, G. 2005. "Dynamic alveolar mechanics and ventilator-induced lung injury." *Critical Care Medicine* 33:122-128.

Chhabra, S., and Prasad, A. K. 2010. "Flow and particle dispersion in a pulmonary alveolus-part 2: effect of gravity on particle transport." *Journal of Biomechanical Engineering* 132:051010.

Chien, W.L., Rising. H and Ottino, J.M. 1986. "Laminar mixing and chaotic mixing in several cavity flows." *Journal of Fluid Mechanics* 170:355-377.

Choi, H.G., Choi, H., and Yoo, J.Y. 1997. "A fractional four-step finite element formulation of the unsteady incompressible Navier-Stokes equations using SUPG and linear equal-order element methods." *Computer Methods in Applied Mechanics and Engineering* 143:333-348.

Choi, J., Tawhai, M.H., Hoffman, E.A., and Lin, C.L. 2009. "On intra- and inter-subject variabilities of airflow in the human lungs." *Physics of Fluids* 21:101901-17.

Cline, H.E. 1987. "Marching cubes: a high resolution 3D surface construction algorithm." *Computer Graphics* 21: 163-169, 1987.

Dailey, H. L., and Ghadiali, S. N. 2007. "Fluid-structure analysis of microparticle transport in deformable pulmonary alveoli." *Journal of Aerosol Science* 38:269-288.

Darquenne, C. 2001. "A realistic two-dimensional model of aerosol transport and deposition in the alveolar zone of the human lung." *Journal of Aerosol Science* 32:1161-1174.

Darquenne, C. 2002. "Heterogeneity of aerosol deposition in a two-dimensional model of human alveolated ducts." *Journal of Aerosol Science* 33:1261-1278.

Darquenne, C., and Kim Prisk, G. 2003. "Effect of gravitational sedimentation on simulated aerosol dispersion in the human acinus." *Journal of Aerosol Science* 34:405-18.

Darquenne, C., and Kim Prisk, G. 2004 "Effect of small flow reversals on aerosol mixing in the alveolar region of the human lung." *Journal of Applied Physiology* 97:2083-2089.

Darquenne, C., and Kim Prisk, G. 2005. "Aerosols in the study of convective acinar mixing." *Respiratory Physiology and Neurobiology* 148:207-216.

Darquenne, C., and Paiva, M. 1996. "Two- and three-dimensional simulations of aerosol transport and deposition in alveolar zone of the human lung." *Journal of Applied Physiology* 80:1401-1414.

Darquenne, C., Harrington, L., and Prisk, G. K. 2009. "Alveolar duct expansion greatly enhances aerosol deposition: a three-dimensional computational fluid dynamics study." *Philosophical Transactions of The Royal Society A* 367:2333-2346.

Davidson, M.R., and Fitz-Gerald, J.M. 1972. „Flow patterns in models of small airway units of the lung." *Journal of Fluid mechanics* 52:161-177.

Duck, P.W., and Bodonyi, R.J. 1988 "Oscillatory flow over a semi-infinite flat plate at low Reynolds numbers." *Computers and Fluids* 16:311-326.

Federspiel, W.J., and Fredberg, J.J. 1988. "Axial dispersion in respiratory bronchioles and alveolar ducts." *Journal of Applied Physiology* 64:2614-21.

Finlay, W.H. 2001. *The mechanics of inhaled pharmaceutical aerosols. An introduction.* London:Academic Press.

Flekkoy, E. G., Rage, T., Oxaal, U., and Feder, J. 1996. "Hydrodynamic Irreversibility in Creeping Flow." *Physical Review Letters* 77:4170-4173.

Fresconi, F.E., and Prasad, A.K. 2007. "Secondary velocity fields in the conducting airways of the human lung." *Journal of Biomechanical Engineering* 129:722-32.

Fung, Y.C. 1988. "A model of the lung structure and its validation." *Journal of Applied Physiology* 64:2132-41.

Gatto, L. A., Fluck, R. R., and Nieman, G. F. 2004. "Alveolar mechanics in the acutely injured lung: Role of alveolar instability in the pathogenesis of ventilator-induced lung injury." *Respiratory Care* 49:1044-1055.

Gefen, A., Elad, D., and Shiner, R. J. 1999. "Analysis of stress distribution in the alveolar septa of normal and simulated emphysematic lungs." *Journal of Biomechanics* 32:891-7.

Gower, S., and Hammond, D. 2007. "CSP deposition to the alveolar region of the lung: Implications of cigarette design." *Risk Analysis* 27:1519-1533.

Haber, S., Butler, J.P., Brenner, H., Emanuel, I., and Tsuda, A. 2000. "Shear flow over a self-similarexpanding pulmonary alveolus during rhythmical breathing." *Journal of Fluid Mechanics* 405:243-268.

Haber, S., Yitzhak, D., and Tsuda, A. 2003. "Gravitational deposition in a rhythmically expanding and contracting alveolus." *Journal of Applied Physiology* 95:657-671.

Haber, S., Butler, J.P., Brenner, H., Emanuel, I., and Tsuda, A. 2000. "Shear flow over a self-similar expanding pulmonary alveolus during rhythmical breathing." *Journal of Fluid Mechanics* 405:243-268.

Haefeli-Bleuer, B., and Weibel, E.R. 1988. "Morphometry of the human pulmonary acinus." *The Anatomical Record* 220:401-414.

Harrington, L., Prisk, G. K., and Darquenne, C. 2006. "Importance of the bifurcation zone and branch orientation in simulated aerosol deposition in the alveolar zone of the human lung." *Journal of Aerosol Science* 37:37-62.

Harrington, L., Prisk, G.K., and Darquenne, C. 2006 "Importance of the bifurcation zone and branch orientation in simulated aerosol deposition in the alveolar zone of the human lung." *Aerosol Science* 37:37-.

Haselton, F. R., and Scherer, P. W. 1982. "Flow visualization of steady streaming in oscillatory flow through a bifurcating tube." *Journal of Fluid Mechanics* 123:315-333.

Helman, J. L., and Hesselink, L., 1991. "Visualizing Vector Field Topology in Fluid Flows." *IEEE Computer Graphics and Applications* 11:36-46.

Henry, F.S., Butler, J.P., and Tsuda, A. 2002. "Kinematically irreversible acinar flow: a departure from classical dispersive aerosol transport theories." *Journal of Applied Physiology* 92:835-.45

Henry, F.S., Laine-Pearson, F.E., and Tsuda, A. 2009. "Hamiltonian chaos in a model alveolus." *Journal of Biomechanical Engineering* 131:0110061-7.

Heyder, J., Blanchard, J.D., Feldman, H.A., and Brain, J.D. 1988. "Convective mixing in human respiratory tract: estimates with aerosol boli." *Journal of Applied Physiology* 64:1273-1278.

Hofmann, W., and Koblinger, L. 1990. "Monte Carlo modeling of aerosol deposition in human lungs. Part II: Deposition fractions and their sensitivity to parameter variations." *Journal of Aerosol Science* 21:675-688.

Hofmann, W., Pawlak,E., and Sturm, R. 2008. "Semi-empirical stochastic model of aerosol bolus dispersion in the human lung." *Inhalation Toxicology* 20:1059-1073.

Horner, M., Metcalfe, G., Wiggins, S., and Ottino, J.M. 2002. "Transport enhancement mechanism in open cavities." *Journal of Fluid Mechanics* 452:199-229.

Jana, S.C., and Ottino, J.M. 1992. "Chaos-enhanced transport in cellular flows." *Philosophical Transactions of Royal Society of London A* 338:519-532

Jana, S.C., Metcalfe, G., and Ottino, J.M. 1994 "Experimental and computational studies of mixing in complex Stokes flows: the vortex mixing flow and multicellular cavity flows." *Journal of Fluid Mechanics* 269:199-246.

Jana, S. C., and Ottino, J. M. 1992. "Chaos-enhanced transport in cellular flows." *Philosophical Transactions of Royal Society of London A* 338:519-532.

Kojic, M., and Tsuda, A. 2004. "A simple model for gravitational deposition of non-diffusing particles in oscillatory laminar pipe flow and its application to small airways." *Journal of Aerosol Science* 35:245-261.

Kumar, H., Lin, C.L., Tawhai, M.H., and Hoffman, E.A. 2009. "The effects of geometry on airflow in the acinar region of the human lung." *Journal of Biomechanics* 42:1635-42.

Larrieu, E., Hinch, E. J., and Charru, F. 2009. "Lagrangian drift near a wavy boundary in a viscous oscillating flow." *Journal of Fluid Mechanics* 630:391-411.

Lee, D.Y., and Lee, J.W. 2003. "Characteristics of particle transport in an expanding or contracting alveolated tube." *Aerosol Science* 34:1193-1215.

Levitzky, M. G. 2007. *Pulmonary Physiology*. Crawfordsville:McGraw-Hill.

Lin, C.L., Lee, H., Lee, T., and Weber, L.J. 2005. "A level set characteristic Galerkin finite element method for free surface flows." *International Journal of Numerical Methods in Fluids* 49:521–547.

Lin, C.-L., Tawhai, M. H., McLennan, G., and Hoffman, E.A. 2007. "Characteristics of the turbulent laryngeal jet and its effect on airflow in the human intra-thoracic airways." *Respiratory Physiology and Neurobiology* 157:295-309.

Lin, C.L., Tawhai, M. H., McLennan, G., and Hoffman, E.A. 2009. "Multiscale Simulation of Gas Flow in Subject-Specific Models of the Human Lung." *IEEE Eng. in Medicine and Biology* 28:25-33.

Litzlbauer, E.J.R., Neuhaeuser C., Moell A., Greschus S., Breithecker A., Franke FE., Kummer W., and Rau WS. 2006. "Three-dimensional imaging and morphometric analysis of alveolar tissue from microfocal X-ray-computed tomography." *American Journal of Physiology Lung Cellular Molecular Physiology* 291: 535-545.

Lyne, W. H. 1971. "Unsteady viscous flow over a wavy wall." *Journal of Fluid Mechanics* 50:33-48.

Ma, B., and Darquenne, C. 2011. "Aerosol deposition characteristics in distal acinar airways under cyclic breathing conditions." *Journal of Applied Physiology* 110: 1271-1282.

Marzo, A., Luo, X. Y., and Bertram, C. D. 2005. "Three-dimensional collapse and steady flow in thick-walled flexible tubes". *Journal of Fluids and Structures* 20:817-835.

McLennan, G., Namati, E., Ganatra, J., Suter, M., O'Brien, E.E., Lecamwasam, K., Van Beek, and Hoffman EA. "Virtual Bronchoscopy" *Imaging Decisions MRI* 11: 10-20, 2007.

Namati, E., Thiesse, J., De Ryk, J., and McLennan, G. 2007. "Dynamic in vivo alveolar morphology using a novel laser scanning confocal microscope" *9th Biennial Conference of the Australian Pattern Recognition Society*, DICTA 99-105.

Newman, S. P., Pavia, D., Moren, F., Sheahan, N. F., Clarke, and S. W. 1981. "Deposition of pressurized aerosols in the human respiratory tract." *Thorax* 36:52-55.

Nithiarasu, P. 2006. "A Matrix Free Fractional Step Method for Static and Dynamic Incompressible Solid Mechanics." *International Journal for Computational Methods in Engineering Science and Mechanics* 7:369-380.

Ottino, J.M. 1989. "The kinematics of mixing: stretching, chaos and transport." *Cambridge texts in applied mathematics*, Cambridge University Press

Parameswaran, H., Bartolak-Suki, E., Hamakawa, H., Majumdar, A., Allen, PG., and Suki, B. 2009. "Three-dimensional measurement of alveolar airspace volumes in normal and emphysematous lungs using micro-CT." *Journal of Applied Physiology* 107:583-592.

Pedrizzetti,G. 1996. "Unsteady tube flow over an expansion." *Journal of Fluid Mechanics* 310:89-111.

Popp, A., Wendel, M., Knels, L., Koch, T., and Koch, E. 2006. "Imaging of the three-dimensional alveolar structure and the alveolar mechanics of a ventilated and perfused isolated rabbit lung with Fourier domain optical coherence tomography." *Journal of Biomedical Optics* 11:14015-9.

Pozrikidis, C. 1994. "Shear flow over a plane wall with an axisymmetric cavity or a circular orifice of finite thickness." *Physics of Fluids* 6:68-79.

Quarteroni, M., Tuveri, M. and Venexiani, A. 2000. "Computational vascular fluid dynamics: problems, models and methods." *Computing and Visualization in Science* 2:163-197.

Riley, N. 2001. "Steady streaming." *Annual Review of Fluid Mechanics* 33, 43-65.

Roberts, E. P. L., and Mackley, M. R. 1995. "The simulation of stretch rates for the quantitative prediction and mapping of mixing within a channel flow." *Chemical Engineering Science* 50:3727-3746.

Robertsand, E.P.L., and Mackley, M.R. 1995. "The simulation of stretch rates for the quantitative prediction and mapping of mixing within a channel flow." *Chemical Engineering Science* 50:3727-3746.

Saha, P.K, Gao, Z., Alford, S.K., Sonka, M., and Hoffman, E.A. 2010. "Topomorphologic separation of fused iso-intensity objects via multiscale opening: separating arteries and veins in 3-D pulmonary CT." *IEEE Transactions Medical Imaging* 29: 840-851.

Sarangapani, R., and Wexler, A. S. 1999. "Modeling aerosol bolus dispersion in human airways." *Journal of Aerosol Science* 30:1345-1362.

Sarangapani, R., and Wexler, A.S. 2000. "The role of dispersion in particle deposition in human airways." *Toxicological Sciences* 54:229–236.

Shen, C., and Floryan, J.M. 1985. "Low Reynolds flow over cavities." *Physics of Fluids* 28:3191-3202.

Sobey, I.J. 1985. "Dispersion caused by separation during oscillatory flow through a furrowed channel." *Chemical Engineering Science* 40,:2129-2134.

Suh, Y.K., and Kang, S. 2008. "Acoustic Streaming." *Encyclopedia of Microfluidics and Nanofluidics*, 1:25-33.

Sung, J., Choi, H.G., and Yoo, J.Y. 2000. "Time-accurate computation of unsteady free surface flows using an ALE-segregated equal-order FEM." *Computer Methods in Applied Mechanics and Engineering* 190:1425-40.

Swanson, P.D., and Ottino, J.M. 1990 "A comparative and experimental study of chaotic mixing of viscous fluids." *Journal of Fluid Mechanics* 213:227-249.

Sznitman J., Heimsch, T., Wildhaber, J. H., Tsuda, A. and Rosgen T. 2009. "Respiratory Flow Phenomena and gravitational deposition in a three-dimensional space-filling model of the pulmonary acinar tree." *Journal of Biomechanical Engineering* 131:031010-16.

Sznitman J., Schmuki S., Sutter R., Tsuda A. and Rösgen T. 2007. "CFD investigation of respiratory flows in a space-filling pulmonary acinus model, Brebbia C.A. ed., Modelling in Medicine and Biology VII." *WIT Transactions on Biomedicine and Health* 12:147-156.

Sznitman, J**.,** Heimsch, F**.,** Heimsch, T**.,** Rusch, D**.,** and Rösgen, T**.** 2007. "Three-Dimensional Convective Alveolar Flow Induced by Rhythmic Breathing Motion of the Pulmonary Acinus**."** *Journal of Biomechanical Engineering* 129:658-665**.**

Taubin, G. 1995. "Marching cubes: a high resolution 3D surface construction algorithm." *Proceedings of the Fifth International Conference on Computer Vision* 852-857.

Tawhai, M. H., Nash, M. P., Lin, C.L., and Hoffman, E. A. 2009. "The influence of supine and prone posture on regional lung density & pleural pressure gradients in the human lung." *Journal of Applied Physiology* 107:912-920.

Tawhai, M.H., and Burrowes, K.S. 2003. "Developing integrative computational models of pulmonary structure." *The Anatomical Record - Part B* 275B:207-18.

Tawhai, M.H., and Lin, C.L. 2010 "Image-based modeling of lung structure and function." *Journal of Magnetic Resonance Imaging* 32:1421-1431.

Timsina, M. P., Martin, G. P., Marriott, C., Granderton, D., and Yianneskis, M. 1994. "Drug delivery to the respiratory tract using dry powder inhalers." *International Journal of Pharmaceutics* 101:1-13.

Tippe, A., and Tsuda, A. 2000. "Recirculating flow in an expanding alveolar model: experimental evidence of flow-induced mixing of aerosols in the pulmonary acinus." *Journal of Aerosol Science* 31:979-986.

Tsuda, A., Butler, J. P., and Fredberg, J. J. 1994. "Effects of alveolated duct structure on aerosol kinetics. II. Gravitational sedimentation and inertial impaction." *Journal of Applied Physiology* 76:2510-2516.

Tsuda, A., Filipovic, N., Haberthur, D., Dickie, R., Matsui, Y., Stampanoni, M., and Schittny, JC. 2008. "Finite element 3D reconstruction of the pulmonary acinus imaged by synchrotron X-ray tomography." *Journal of Applied Physiology* 105:964-976.

Tsuda, A., Henry, F.S., and Butler, J.P. 2008 "Gas and aerosol mixing in the acinus." *Respiratory Physiology and Neurobiology* 163:139-149.

Tsuda, A., Henry, F.S., Butler, J.P. 1995. "Chaotic mixing of alveolated duct flow in rhythmically expanding pulmonary acinus." *Journal of Applied Physiology* 79:1055-1063.

Tsuda, A., Rogers, R.A., Hydon, P.E., and Butler, J.P. 2002. "Chaotic mixing deep in the lung." *Proceedings of National Academy of Science"* 9910173-178.

Wang and Ottino, 2009. "Inertial effects on chaotic advection and mixing in a 2D cavity flow." *Industrial and Engineering Chemistry Research* 48:2436-2442.

Wang, H., Iovenitti, P., Harvey, E., and Masood, S. 2003. "Numerical investigation of mixing in microchannels with patterned grooves." *Journal of Micromechanics and Microengineering* 13:801-808.

Wang, J., and Ottino, J. M. 2009. "Inertial effects on chaotic advection and mixing in a 2D cavity flow." *Industrial and Engineering Chemistry Research* 48:2436-2442.

Watz, H., Breithecker, A., Rau, WS., and Kriete, A. 2005. "Micro-CT of the human lung: imaging of alveoli and virtual endoscopy of an alveolar duct in a normal lung and in a lung with centrilobular emphysema-initial observations." *Radiology* 236:1053-1058.

Weibel, E.R., Sapoval, B., and Filoche, M. 2004. "Design of peripheral airways for efficient gas exchange." *Respiratory Physiology and Neurobiology* 148:3-21.

Woods, J.C., Choong, C.K., Yablonskiy, D.A., Bentley, J., Wong, J., Pierce, J.A., Cooper, J.D., Macklem, P.T., Conradi, M.S., and Hogg, J.C. 2006. "Hyperpolarized 3He diffusion MRI and histology in pulmonary emphysema." *Magnetic Resonance Medicine* 56:1293-1300.

Xia, G., and Lin, C.L. 2008. "An unstructured finite volume approach for structural dynamics in response to fluid motions." *Computers and Structures* 86:684-701.

Xia, G., Tawhai, M.H., Hoffman, E.A., and Lin, C.L. 2010. "Airway Wall Stiffness and Peak Wall Shear Stress: A Fluid-Structure Interaction Study in Rigid and Compliant Airways." *Annals of Biomedical Engineering* 38:1836-1853.

Yin, Y., Choi, J., Hoffman, E.A., Tawhai, M.H., and Lin, C.L. 2010. "Simulation of pulmonary air flow with a subject-specific boundary condition." *Journal of Biomechanics* 43:2159-63

Yin, Y., Hoffman, E. A., and Lin, C.L. 2009a. "Mass preserving non-rigid registration of CT lung images using cubic B-spline." *Medical Physics* 36:4213-4222.

Yin, Y., Hoffman, E. A., and Lin, C.L. 2009b. "Local tissue-weight-based nonrigid registration of lung images with application to regional ventilation." *SPIE Medical Imaging* 7262, 72620C.

Yue, W., Lin, C-L., and Patel, V.C. 2003. "Numerical simulation of unsteady multidimensional free surface motions by level set method." *International Journal for Numerical Methods in Fluids* 42:853-884.